

EXPLORING THE POTENTIAL OF LOW-COST PEROVSKITE CELLS AND
IMPROVED MODULE RELIABILITY TO REDUCE LEVELIZED COST OF
ELECTRICITY

A Dissertation

Submitted to the Faculty

of

Purdue University

by

Reza Asadpour

In Partial Fulfillment of the

Requirements for the Degree

of

Doctor of Philosophy

December 2020

Purdue University

West Lafayette, Indiana

THE PURDUE UNIVERSITY GRADUATE SCHOOL
STATEMENT OF DISSERTATION APPROVAL

Dr. Muhammad A. Alam, Chair

School of Electrical and Computer Engineering

Dr. Mark Lundstrom

School of Electrical and Computer Engineering

Dr. Peter Bermel

School of Electrical and Computer Engineering

Dr. Peide Ye

School of Electrical and Computer Engineering

Approved by:

Dr. Dimitrios Peroulis

Head of the school of Electrical and Computer Engineering

To my family who always supported me

ACKNOWLEDGMENTS

I would like to express my sincere appreciation to Professor Muhammad A. Alam for his support and patience as a teacher, mentor, and advisor. I have learned many academic and life lessons from him through my years as a PhD student in his group. With his help I re-learned the semiconductor physics and modeling.

I like to acknowledge my committee members Prof. Mark Lundstrom, Prof. Peide Ye, and specially Prof. Peter Bermel for their support and collaboration.

I would like to say special thanks to Dr. Aditya Mohite, Dr. Wanyi Nie for years of collaborations, sharing the experimental results with us, and fruitful discussions that we had. Also I would like to thank Dr. Steve Johnston and Dr. Dana Sulas for their help and collaboration.

I also want to say a huge thank you to my past and present group members and colleagues. We shared a lot of good memories and laughs together.

To my past lab mates from Alam's group: Xin Jin, Woojin Ahn, Piyush Dak, Aida Ebrahimi, Xingshu Sun, Chunsheng Jiang, Hai Jiang, SangHoon Shin, Mohammad Ryyan Khan, Raghu V. K. Chavali, Nicolo Zagni, Ratul Baruah, Md Abdul Wahab, Sambit Palit, and Ankit Jain for their helpful thoughts and supports whenever I asked them a question.

To my current lab mates from Alam's group: Tahir Patel, Yen-Pu Chen, Bikram Mahajan, Marco Fratus, Ajanta Saha, and Levi Davies. The arguments and collaborations we had are going to be a reminder of our friendship. I also want to thank my dear friends including Mohammadhasan Sasar, Dr. Amir Rashidinejad, Dr. Nastaran Karimi, Dr. Zamzam Golmohammadi, Mehdi Jokar, Dr. Mohsen Minaei, Dr. Evan Wilson for their care and encouragements.

I would like to thank Vicki Johnson, Christine M. Ramsey, Matt Golden, and Elisheba Vanwinkle for their help in scheduling meetings, reserving rooms, and administrative assistance.

And last but not least, I would like to express my deepest gratitude towards my family specially my parents: Aliasghar Asadpoor and Touba Haghshenas Lari who always helped me through every chapter of my life. My PhD journey would have not been possible without their sacrifice and unconditional love.

TABLE OF CONTENTS

	Page
LIST OF TABLES	x
LIST OF FIGURES	xi
ABSTRACT	xx
1 INTRODUCTION	1
1.1 A Brief History of Solar Energy	2
1.2 Techniques of LCOE Reduction Discussed in This Thesis	5
1.2.1 Decreasing the Cost by using Thin-Film Solar Cell Technology	5
1.2.2 Increasing the Energy Output by Using Silicon-Perovskite Tandem Solar Cells	6
1.2.3 Increasing the Lifetime/Reliability of Perovskite Solar Cells	6
1.2.4 Degradation Modes and Potential Increase of c-Si Projected Lifetime	7
1.3 Conclusions	9
2 BULK PEROVSKITE SOLAR CELL	11
2.1 Introduction	11
2.2 Hot-casting Method Improves Efficiency by Increasing Grain Size	13
2.3 Simulation Framework	18
2.3.1 Optical Modeling	18
2.3.2 Self-consistent transport simulation	18
2.3.3 Importance of grain sizes for electronic transport of electrons and holes	19
2.4 Summary and Conclusion	23
3 BIFACIAL PEROVSKITE-HIT TANDEM STRUCTURE TO PRODUCE HIGHLY EFFICIENT SOLAR CELL	24
3.1 Background and Motivation	24

	Page	
3.2	Simulation Framework	27
3.3	Traditional Tandem Configuration	35
3.4	Bifacial Tandem Configuration	38
3.5	Summary and Conclusion	40
4	2D PEROVSKITE SOLAR CELLS- A WAY TO IMPROVE THE RELIABILITY	42
4.1	background	44
4.2	Experimental Results	47
4.2.1	Thickness Dependence of the Performance	47
4.2.2	Light Intensity Dependence	51
4.2.3	Temperature Dependence	54
4.3	Simulation Results	56
4.4	Conclusions	60
5	RELIABILITY OF C-SI SOLAR MODULES	62
5.1	Theory and Modeling Framework	63
5.2	Simulation Framework	64
5.3	Effect of Finger Corrosion and Solder Bond Failure	67
5.3.1	Metal Finger Thinning	69
5.3.2	Metal Delamination (Glass Frit Corrosion under Dark)	72
5.3.3	Solder Bond Failure	73
5.4	Cell vs. Module I-V Characteristics	75
5.5	Discussion	78
5.5.1	Reverse Bias Characteristics	81
5.5.2	Irradiance Dependent Efficiency	81
5.5.3	Optical Measurement to Distinguish between Yellowing and Delamination-induced Loss in Photo-current	82
5.5.4	Combination of Degradation Mechanisms	83
5.6	Summary and Conclusion	84

	Page
6 DLIT IDENTIFIES SOLDER BOND FAILURE AS THE ROOT CAUSE OF THE SERIES RESISTANCE INCREASE	85
6.1 Introduction	85
6.2 Theory and Simulation: Current Redistribution in Modules with Broken solder bonds	89
6.3 Theory and Simulation: Hot Spot Formation around Broken solder bonds	91
6.4 Experimental Validation	96
6.5 Summary and Conclusions	99
7 A PHYSICS-BASED AND PROBABILISTIC MODEL THAT PREDICTS THE SOLDER BOND FAILURE IN C-SI SOLAR PANELS	103
7.1 Introduction	104
7.2 Theory and Simulation Framework	106
7.2.1 An Overview of the Theoretical Framework	106
7.2.2 Step 1: Module Temperature Fluctuation Determines the Accumulated Stress on the Solder Bonds	107
7.2.3 Step 2: Accumulated Damage and Broken Solder Bonds	108
7.2.4 Step 3: Broken Solder Bonds and Increasing Series Resistance	110
7.3 Statistical Distribution of Solder Bond Failure at Module Level	113
7.3.1 A Markov Chain Model for Solder Bond Failure	113
7.3.2 Results and Discussion	115
7.4 Conclusion and Summary	116
8 CONCLUSIONS	118
8.1 Summary of Chapter 2: A 3D high-efficiency Perovskite Technology	118
8.2 Summary of Chapter 3: Efficiency Enhancement by Tandem Solar Cells	119
8.3 Summary of Chapter 4: Reliability of Perovskite Solar Cells	120
8.4 Summary of Chapter 5: Reliability of c-Si Solar Cells	122
8.5 Summary of Chapter 6: Electrical Signature of Solder Bond Failure	124
8.6 Summary of Chapter 7: A Physics-based Model of Solder Bond Failure	124
8.7 Future Work: Physics-based Reliability Modeling	126

	Page
8.7.1 Forward Modeling: Location-specific Predictive Reliability Model of a Solar Cell	126
8.7.2 Inverse Modeling: Reading the "Heartbeat" of a Solar Farm	126
REFERENCES	130
A IMPORTANCE OF THICKNESS VARIATION FOR INDIVIDUAL CELLS	153
B ENERGY BAND DIAGRAM OF INDIVIDUAL SUB-CELLS OF PEROVSKITE- HIT TANDEM STRUCTURE	155
VITA	157

LIST OF TABLES

Table	Page
2.1 Equations for carrier transport	19
2.2 The simulation parameters used in numerical simulation of Perovskite cell	20
3.1 Equations for carrier transport	30
3.2 The simulation parameters used in numerical simulation of HIT cell [77]	31
3.3 The simulation parameters used in numerical simulation of perovskite cell .	35
5.1 Baseline Simulation Parameters for Cells in Griddler	68
6.1 Baseline Simulation Parameters for Cells in Griddler	93
6.2 Baseline Simulation Parameters for the Cell simulated in HSPICE	94
7.1 Baseline Simulation Parameters for Cells in Griddler	111
7.2 Number of Broken Bonds vs. Change in Series Resistance Lookup Table	113

LIST OF FIGURES

Figure	Page
1.1 Global primary energy consumption, measured in terawatt-hours (TWh) per year. Here 'other renewables' are renewable technologies not including solar, wind, hydro-power and traditional bio-fuels. [1]	1
1.2 Selected renewable energy generation technologies are cost-competitive with conventional generation technologies under certain circumstances. [2]	2
1.3 LCOE improvement of HIT cells if the structure is conventional, bifacial, bifacial tandem, or when sun tracking is utilized.	4
1.4 LCOE as a function of the lifetime of the solar panel at Kansas City, MO.	5
1.5 Tests help forward modeling framework that predicts lifetime/performance and by using field data framework can help calibrating test conditions. . .	7
2.1 Progress of perovskite solar cells compared to other thin-film technologies	12
2.2 Processing scheme for perovskite thin-film using hot casting methods and observations for large-area mm-scale crystal grain formation for perovskite ($PbCH_3NH_3I_{3-x}Cl_x$) based thin-film. (a) Hot-casting scheme for large-area crystal growth. Optical micrographs illustrating grain formation as a function of substrate temperature with the casting solution maintained at ($70^\circ C$) and (b) Large area grain formation using casting solvents with high boiling points. (c) Compares the grain size as a function of processing temperature obtained for the hot-casting and the conventional post-annealing methods for the substrate processing temperature.	14
2.3 Solar cell device architecture and performance (a) Planar device configuration used for this study and (b) J-V curves obtained under AM 1.5 illumination and (c) overall PCE (left) and J_{SC} (right) as a function of crystalline grain size. Grey box represents the range of PCE obtained using the conventional post-annealing process. (d) Average J-V characteristics resulted by sweeping the voltage from forward to reverse and reverse to forward bias demonstrates the absence of hysteresis. These were curves were obtained by averaging 15 sweeps in each direction. (e) J-V curves at different voltage scan-rates in voltage delay time (ms) or Volts/sec again demonstrate negligible hysteresis. (f) Describes the variation in the PCE for 50 measured devices.	16

Figure	Page
2.4 Solar cell parameters measured under AM 1.5 illumination. (a) Open circuit voltage (V_{OC}) and (b) FF extracted from J-V curve under AM 1.5 illumination at 100 mW/cm^2 solar simulator for planar perovskite solar cell as a function of grain size.	17
2.5 Carrier densities and recombination profiles within small and large grain solar cells: (a) Carrier densities inside the cell at the open circuit condition for small grain cells processed at 120°C (solid lines) and large grain cells processed at up to 180°C (dashed lines), respectively. The inset magnifies the carrier concentrations at the PCBM-Perovskite interface. (b) Corresponding normalized cumulative recombination rates inside the cell for small grain cells (solid line) and large grain cells (dashed line), at the open circuit condition.	21
2.6 Self-consistent device simulation attributes the process-dependent PCE gain to the improved mobility of films with larger grains. (a) The simulated J-V characteristics for large- and small-grain devices reproduce the salient features of the corresponding experimental data. (b) Typical energy band diagram at short circuit (SC) indicates the importance of a semi-intrinsic (reduced self-doping) fully depleted absorber in directing the charge carriers to their respective contacts; otherwise, the charge carrier would be lost to recombination in the field-free regions. (c) With all other parameters characterized and/or obtained from the literature, the PCE values appear to be correlated to the bulk mobility of the absorber (labels correspond to the average grain size). (d) Experimental data for V_{OC} as a function of illumination light intensity for a large-grain device (180°C) and a small-grain device (100°C) along with the linear fit (red line).	22
3.1 (a) A solar panel generally utilizes the direct illumination of sunlight. A fraction of the light can also be scattered from the ground onto the back of the panel. (b) Traditional tandem structure, and (c) a bifacial tandem structure.	27
3.2 Absorption spectrum of optimum-thickness classical tandem solar cell. . .	28
3.3 Absorption spectrum of top incident light for bifacial tandem solar cell. .	29
3.4 Absorption spectrum of bottom incident light (Albedo reflection) for bifacial tandem solar cell.	30

Figure	Page	
3.5	Absorbed sunlight (in terms of corresponding current density J_{abs}) is shown for perovskite (green) and HIT (red) subcells as a function of L_{PVK} (perovskite layer thickness). The short circuit current of the series tandem will be limited to $\min(J_{abs}^{Si}, J_{abs}^{PVK})$ as shown by the dashed black lines. We set $L_c Si = 200\mu m$	36
3.6	$J - V$ characteristics of (a) individual HIT and perovskite cells (b) HIT (red) and perovskite (green) sub-cell $J - V$ characteristics are shown along with the tandem cell (black dashed line). Inset table shows sub-cells contribution to the efficiency	38
3.7	Spatial photo-generation profile in the convention and bifacial tandem cell. The primary sunlight is from the left	39
3.8	(a) The J_{SC} of the sub-cells and bifacial tandem as function of albedo R_A . (b) Output η_T^* (normalized to 1-sun) of the perovskite and HIT sub-cells (green and red areas) are shown. The bifacial tandem (black dashed line) outperforms the bifacial HIT cell (blue solid line) for $R_A < 40\%$. Common backgrounds such as grass, white concrete, and snow have R_A of approximately 30%, 60%, and 90%, respectively [98].	41
4.1	(a) Experimental (red line) and simulated (black dashed line) current-density-voltage (J-V) curves under an AM.1.5G solar simulator for planar devices using 2D $(BA)_2(MA)_3Pb_4I_{13}$ perovskites as the absorbing layer at optimized thickness (230 nm). The inset shows the device architecture. Al, aluminum; PCBM, [6,6]-phenyl-C61-butyric acid methyl ester; PEDOT:PSS, poly(3,4-ethylenedioxythiophene) polystyrene sulfonate; FTO, fluorine-doped tin oxide. (b), External Quantum Efficiency (EQE; red circles and line) and integrated short circuit current density (J_{SC} ; blue dashed line) as a function of wavelength.	43
4.2	(a) The crystal structure of the Ruddlesden-Popper $(BA)_2(MA)_2Pb_3I_{10}$ and $(BA)_2(MA)_3Pb_4I_{13}$ layered perovskites, depicted as n polyhedral blocks, where n refers to the number of layers; the BA spacer layers are depicted as space-fill models to illustrate the termination of the perovskite layers. (b), Schematic representation of the (101) orientation, along with the (111) and (202) planes of a 2D perovskite crystal	44

Figure	Page	
4.3	Photovoltaics with various absorber thickness evaluated by J–V characteristics. (a) Molecular structure of $BA_2MA_3Pb_4I_{13}(Pb_4)$ and (b) planar solar cell device structure used in this study. (c) J–V curve under AM 1.5G solar-simulated light with 1-Sun equivalent power and (d) EQE spectrum collected under short-circuit condition with monochromatic light for planar device with various Pb_4 film thicknesses. (e–g) Extracted average PCE, J_{SC} and V_{OC} as a function of film thickness. The J_{SC} for a device with methyl ammonium lead triiodide ($MAPbI_3$) as an absorber in the same structure is measured as a comparison in f (black curve). Error bars in (e, f) were s.e.m. collected over eight devices of various absorber thickness for statistics	48
4.4	the energy band diagram for (a) 300nm and (b) 620nm perovskite thickness at three different external bias conditions.	50
4.5	Light intensity dependence with device J–V characteristics. Normalized light J–V curves for a device with absorber thicknesses of (a) 220 nm and (b) 375 nm under various illumination intensities. (c) J_{SC} value as a function of light power over a wide illumination range. (d) V_{OC} as a function of illumination intensities for two device thicknesses. (e, f) Calculated band energy as a function of film thickness and (g, h) normalized recombination profile as a function of distance in the device for two typical thicknesses. (i, j) Schematics illustrating the carrier recombination processes in thin film and thick film in the quantum well-layered perovskite structure. . . .	52
4.6	Device characterization under low temperatures. (a), normalized light J-V curves under 1-Sun illumination for device with absorber thickness of 220 nm. (b), J_{SC} , (c), V_{OC} and (d), fill factor (FF) as a function of temperature, dashed line is guidance to the eye. (e), extracted J-V slope at SC at various temperatures with dashed line as fitting curve and (f), the linear plot following Arrhenius equation by plotting the inverse J-V slope in natural log scale against $1/T$, dashed line is linear fit.	55
4.7	Model and simulation results. (a), the model shows potential wells that can prevent carriers from escaping. (b) and (c), the thickness dependence of J-V curves and J_{SC} . Very thick structures increase the recombination in wells and reduce J_{SC} . (d), intensity dependence of normalized J-V curves. (e-h), Temperature dependence of J-V curves and the extracted J_{SC} , V_{OC} and FF as a function of temperature. The simulated normalized J-V curves are shifted by 5% of J_{SC} at T=200 K to account for temperature dependent carrier generation. The experimental data taken from Fig. 4.3 and Fig. 4.6 in grey symbols are plotted along with the simulated data to directly compare the two.	57

Figure	Page
4.8 (a) Experimental and simulated V_{OC} as a function of temperature. (b) The mobility values used in the drift-diffusion simulator were fitted by the Gaussian-disorder mobility model to find μ_{∞} and c	59
4.9 Energy band diagram and normalized total recombination at T=150 K. At (a,d) short circuit (b,e) maximum power point and (c,f) open circuit. More than 92% of total recombination happens inside the quantum wells. Low temperature does not provide enough thermal energy for carriers to leave the wells efficiently.	60
4.10 Energy band diagram and normalized total recombination at T=300 K. At (a,d) short circuit (b,e) maximum power point and (c,f) open circuit. Less than 75% of total recombination occurs inside the quantum wells since thermal energy helps the carriers to escape the wells.	61
5.1 (a) A schematic of a section of a solar cell and locations where three types of degradation may occur. Simple schematics of how corrosion changes the metal contacts and current path in the fingers, busbars, ribbon, and Si wafer when (b) metal thinning (c) metal delamination and (d) solder bond failure occur. (i) Before degradation, (ii) After degradation. (The glass frit allows electrical contact to the silicon surface after deposition of the anti-reflective coating during contact firing. [161])	65
5.2 (a) A schematic of the Five-parameter model. (b) Two-dimensional grid connection of the five-parameter model in Griddler. The magnitudes of the circuit elements depend on the location within the cell. (c) Voltage map distribution of a pristine cell. The difference between V_{min} and V_{max} is in order of $\frac{k_B T}{q}$, allowing highly efficient current collection from any location within the cell.	67
5.3 (a) A schematic diagram of grid configuration associated with finger thinning. (b) and (c) show corresponding voltage map at V_{MP} where $40.0\mu m$ and $59.5\mu m$ out of $60.0\mu m$ of the finger width have been corroded. Arrows show a general current collection path. Thinner arrows indicate less current is being collected due to finger thinning. Shaded area in (a) corresponds to the brighter part in (b) and (c) that have higher voltage drop. A large portion of current in shaded area is being sunk in the strongly turned on diodes and does not contribute to total collected current. . . .	71
5.4 I-V curves associated with five different corroded finger widths. The output power follows the I_{MP} trend. The slight I_{SC} increase is due to partial removal of the contacts and reduced shading of contacts. Significant output power reduction starts after $50\mu m$ corrosion of the finger width. . . .	72

Figure	Page
5.5 (a) Finger delamination schematic and (b) voltage map at V_{MP} where 3 cm out of 15.6 cm finger length has been delaminated. Arrows show a general current collection path. Thinner arrows show less current is being collected due to finger delamination. Shaded area in (a), corresponding to brighter part in (b), does not contribute to total collected current. All of the current in this part marked by “x” is being sunk in the strongly turned on diodes and turns to heat.	74
5.6 I-V curves for five different corroded lengths. The output power follows the I_{MP} trend. The voltage drop is not significant when 0.5 cm of length is corroded, therefore, the I_{SC} does not drop.	75
5.7 (a) Solder bond failure schematic and (b) voltage map at V_{MP} where 7 bonds (tabbing points) out of 15 have been broken. Arrows show a general current collection path from fingers to busbars and then ribbons. The portion of current in shaded area (a) goes through a longer and more resistive path in the busbar to reach the first healthy tabbing point. Due to the metallic resistivity of the path that current goes through the voltage drop is not high enough to turn the diodes on and sink current significantly at low bias.	76
5.8 I-V curves as a function of the number of broken solder bonds. Since the voltage drop is not significant at I_{SC} there is no change in I_{SC} even when almost half of the bonds are broken. However, the I_{MP} drops as the voltage drop over the broken bonds increases.	77
5.9 (a) A schematic of the degraded cells within a module. Here, N is the number of degraded cells $N = (r + c - 2) \times 2$, whereas M is the number of healthy cells $M = r \times c - N (M = 10, N = 26)$. We assume only the edge cells in the gray area degraded due to corrosion. Module level I-V curves synthesized using cell level results of Griddler I-V curves for different degradations involving: (b) metal finger thinning, (c) finger delamination, and (d) solder bond failure.	78
5.10 Breakdown of power output for cells and module as a function of (a) corroded width (metal finger thinning), (b) corroded length (finger delamination), and (c) number of broken bonds (solder bond failure).	79
5.11 The changes of series resistance and shunt resistance are plotted as a function of (a,b) corroded width, (c,d) corroded length, and (e,f) the number of broken solder bonds. Here, $R_{S_{Pristine}} = 4.2 \times 10^{-3} \Omega$	80
5.12 The I-V characteristics compare PID vs. various degrees of finger thinning (e.g. $57 \mu m$ and $59 \mu m$ out of $60 \mu m$ width). We assume that the area affected due to these two degradation mechanisms are equal.	81

Figure	Page
5.13 Irradiance dependence of efficiency. At lower irradiance, a real shunt (related to PID, for example) reduce the cell efficiency much more significantly compared to a fake shunt (associated with finger corrosion).	82
5.14 Irradiance dependence of efficiency. At lower irradiance, a real shunt (related to PID, for example) reduce the cell efficiency much more significantly compared to a fake shunt (associated with finger corrosion).	83
6.1 (a-d) EL/PL/DLIT help characterizing local resistance of the cell since they contain spatially-resolved information on the position of increased resistance. In contrast, (e) the I-V measurements give us information about module-level series resistance. (f) The EL image highlights the location of back-side solder pads, and there is higher EL signal near certain solder pads. The DLIT shows non-uniform heating at back side solder pads. (g) The zoomed in schematic shows that solder bond failure can lead to series resistance degradation, which manifests itself as localized hotspots in DLIT/EL images.	87
6.2 (a) Top view of a typical solar cell with the ribbons connected to the busbar through eight solder bonds. (b) Side view of the pristine module showing current transfer pathways from the ribbon to the busbar, through healthy solder bonds (white boxes). (c) Top view of a solar cell with a broken tabbing point and corresponding redistribution of current. (d) Side view of modified current transfer pathways between the ribbon and the busbar. Current cannot go through the broken bond, hence more current will go through the remaining healthy bonds. Localized failure within the backside solder pads is governed by the same principle and therefore leads to a similar current redistribution.	90
6.3 Power dissipation map of solar cells with (a) zero, (b) one, (c) two, (d) three, and (e) four alternating broken solder bond(s) on each ribbon. The black crosses show the broken bonds and the white dots show the healthy ones. It is possible to pinpoint the broken tabs. Because more current goes through the healthy tabs and they become hotter (hotspots). (f) Measured DLIT image indicating the regions closer to current injection points at the bottom solder-pads contain characteristic asymmetric doublet hotspots.	92
6.4 (a) Schematic solar cell and zoomed in elements of the half-cell simulated in HSPICE. Sub-cells include the silicon (semiconductor) part and finger resistance. (b) Power dissipation in different parts of the cell in (b) Pristine, (c) Half-broken, and (d) Fully broken condition of second solder bond (R_{SB_2}). (e) Relative change in power dissipation before and after the second solder bond breaks. Only adjacent metallic parts show a significant change.	100

Figure	Page	
6.5	There is a strong correlation between power loss, series resistance, and number of hot spots increase in the experimental set. If the internal circuitry has degraded the root cause can only be series resistance increase due to solder bond failure.	101
6.6	Severely degraded module (a) and mildly degraded module (b). DLIT images show severely degraded modules have more hot spots validating that more broken bonds cause more hotspots and more power loss. . . .	102
7.1	(a) The temperature variation causes the module to expand and contract. (b) Initial and degraded cell with one broken bond.	105
7.2	Top view of a cell with three busbars and eight solder bonds on each busbar. Horizontal red lines show fingers while vertical blue lines show busbars. The healthy solder bonds are shown as circles and broken ones are the black crosses. One row of solder bonds breaks when the module/cell is exposed to $5kPa$ of accumulated damage.	107
7.3	(a) Module temperature and (b) reversal temperature crossing as a function of time from April to November. (c) Accumulated damage (red line) and the number of broken solder bonds (black circles) as a function of time starting at time zero.	109
7.4	(a) J-V curve of a cell with a different number of broken bonds, (b) non-linear dependence of normalized efficiency as a function of the number of broken bonds, and (c) normalized efficiency (black circles) and accumulated damage (red line) as a function of time.	112
7.5	(a) series resistance as a function of the number of broken bonds. (b) Increasing series resistance as a function of time.	112
7.6	(a) Distribution of the number of cells with n rows of broken bonds N_n . (b) Distribution of the number of cells with n rows of broken bonds N_n at ten different points in time in bar plot for easier visualization.	115
7.7	(a) J-V curve of a module undergoing solder bond failure at different times. (b) The efficiency of the module as a function of time saturates close to the end.	115
7.8	(a) Discrete and sudden drops in efficiency due to solder bond failure results of (a) simulation and (b) extracted from measurement.	116
8.1	PID assisted corrosion process needs the circuit to be completed by drifted sodium ions	127

Figure	Page
8.2 Electrical equivalent of Butler-Volmer equation of a freely corroding system. A stands for anode, C for cathode, Ox for oxidation, and Red for reduction. β is the Tafel slope and positive values are used in the equation, and E values are SHE reduction potential.	128
8.3 The causes, phenomena, and electrical signatures due to causes influencing the parameters in the five-parameter model. The list is not comprehensive.	129
A.1 Thickness dependence of perovskite cell characteristics.	153
A.2 Thickness dependence of HIT cell characteristics.	154
B.1 The energy band diagram of the perovskite (PVK) sub-cell under short circuit condition.	155
B.2 The energy band diagram of the HIT sub-cell under short circuit condition.	156

ABSTRACT

Asadpour, Reza Ph.D., Purdue University, December 2020. Exploring the Potential of Low-cost Perovskite Cells and Improved Module Reliability to Reduce Levelized Cost of Electricity. Major Professor: Muhammad A. Alam Professor.

The manufacturing cost of solar cells along with their efficiency and reliability define the levelized cost of electricity (LCOE). One needs to reduce LCOE to make solar cells cost competitive compared to other sources of electricity. After a sustained decrease since 2001 the manufacturing cost of the dominant photovoltaic technology based on c-Si solar cells has recently reached a plateau. Further reduction in LCOE is only possible by increasing the efficiency and/or reliability of c-Si cells. Among alternate technologies, organic photovoltaics (OPV) has reduced manufacturing cost, but they do not offer any LCOE gain because their lifetime and efficiency are significantly lower than c-Si. Recently, perovskite solar cells have showed promising results in terms of both cost and efficiency, but their reliability/stability is still a concern and the physical origin of the efficiency gain is not fully understood.

In this work, we have collaborated with scientists industry and academia to explain the origin of the increased cell efficiency of bulk solution-processed perovskite cells. We also explored the possibility of enhancing the efficiency of the c-Si and perovskite cells by using them in a tandem configuration. To improve the intrinsic reliability, we have investigated 2D-perovskite cells with slightly lower efficiency but longer lifetime. We interpreted the behavior of the 2D-perovskite cells using randomly stacked quantum wells in the absorber region. We studied the reliability issues of c-Si modules and correlated series resistance of the modules directly to the solder bond failure. We also found out that finger thinning of the contacts at cell level manifests as a fake shunt resistance but is distinguishable from real shunt resistance by exploring the reverse

bias or efficiency vs. irradiance. Then we proposed a physics-based model to predict the energy yield and lifetime of a module that suffers from solder bond failure using real field data by considering the statistical nature of the failure at module level. This model is part of a more comprehensive model that can predict the lifetime of a module that suffers from more degradation mechanisms such as yellowing, potential induced degradation, corrosion, soiling, delamination, etc. simultaneously. This method is called forward modeling since we start from environmental data and initial information of the module, and then predict the lifetime and time-dependent energy yield of a solar cell technology. As the future work, we will use our experience in forward modeling to deconvolve the reliability issues of a module that is fielded since each mechanism has a different electrical signature. Then by calibrating the forward model, we can predict the remaining lifetime of the fielded module. This work opens new pathways to achieve 2030 Sunshot goals of LCOE below 3c/kWh by predicting the lifetime that the product can be guaranteed, helping financial institutions regarding the risk of their investment, or national laboratories to redefine the qualification and reliability protocols.

1. INTRODUCTION

The rapid increase in worldwide energy consumption over the past few decades has been generally satisfied by fossil fuel or nuclear energy, as shown in Fig. 1.1. In order to decrease the fossil-fuel pollution and alleviate recycling concerns regarding nuclear waste, there is an urgent need to increase the use of clean and renewable energy, such as hydro-power, wind, solar, etc. Historically, renewable energy has not been cost-competitive and economically viable. Over the last decade, therefore, there have been coordinated and persistent worldwide research and development efforts to reduce to cost of renewable energy and make the technologies viable alternatives to fossil fuel and nuclear energy.

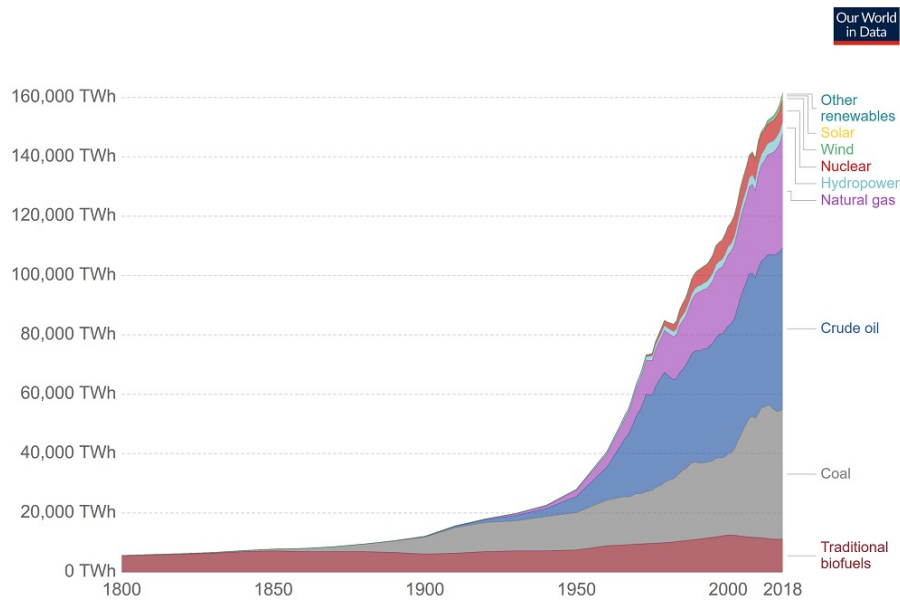


Fig. 1.1. Global primary energy consumption, measured in terawatt-hours (TWh) per year. Here 'other renewables' are renewable technologies not including solar, wind, hydro-power and traditional bio-fuels. [1]

Renewable energies are clean, but more expensive compared to fossil fuels based on a measure/metric called the "levelized cost of electricity" (LCOE). The metric compares the cost of generating a unit of energy by different sources. A comparison of the LCOE is summarized in Fig. 1.2.

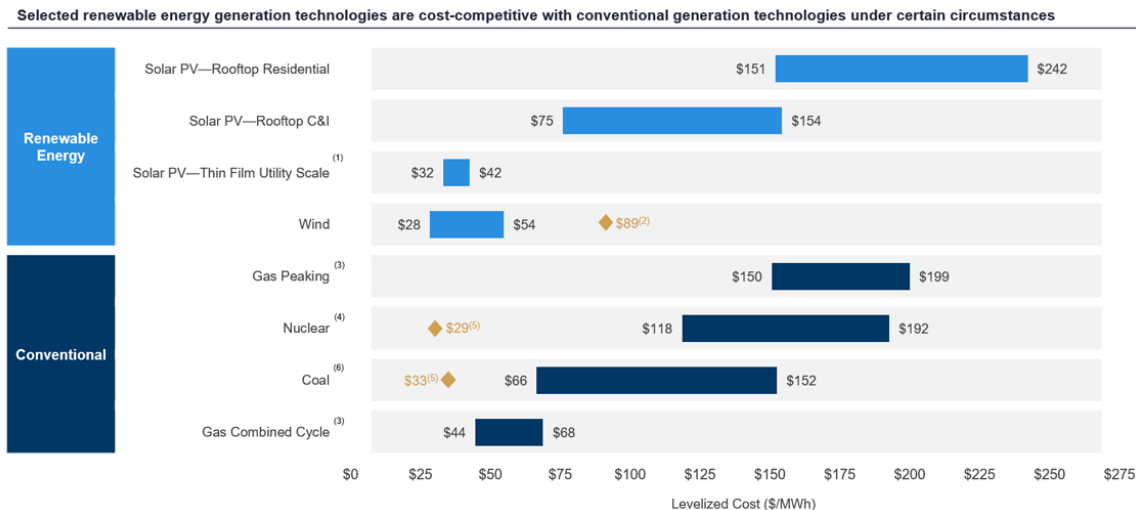


Fig. 1.2. Selected renewable energy generation technologies are cost-competitive with conventional generation technologies under certain circumstances. [2]

1.1 A Brief History of Solar Energy

The Sun has been the driver of life on earth and solar energy has been harvested by various passive techniques since the earliest days of history. By the 7th century B.C., historical records show that the use of magnifying glass to concentrate sunlight and start a fire. Between the 1st to 4th centuries A. D., Romans used south-facing windows to warm their "sun-rooms" and by the seventeenth century, there have been reports of solar-powered steamboats [3]. The use of direct conversion of sunlight to electricity gathered steam by the late 1800s related to curious effects of increased conductivity in electro-chemical cells and semiconductors such as selenium when exposed directly to

sunlight. The research eventually culminated in 1954 with the discovery of modern solar cells. Within just four years, these 10% efficient silicon solar cells received widespread attention as a breakthrough technology by powering Vanguard I for the space application [3]. Since then, successive government initiatives have supported the development of solar cells. Over the years, efficiency and reliability have increased dramatically, and manufacturing and installation techniques have been perfected. In just 10 years since 2010, the price of silicon solar cells has dropped by a factor of 10. However, the price reduction has plateaued in recent years as the single-junction silicon solar cell efficiency (26.7%) is beginning to approach the theoretical efficiency defined by the Shockley-Queisser limit ($\sim 29.7\%$) [4], [5]. Moreover, it is been difficult to further reduce the material, manufacturing, and installation cost.

To explore new opportunities to reduce cost further, it is helpful understand the cost components that define LCOE, as shown in Eq. 1.1.

$$\text{LCOE} = \frac{\text{sum of costs over lifetime}}{\text{sum of electrical energy produced over lifetime}} = \frac{\sum_{t=1}^n \frac{I_t + M_t + F_t}{(1+r)^t}}{\sum_{t=1}^n \frac{E_t}{(1+r)^t}} \quad (1.1)$$

where I_t is investment expenditures in the year t , M_t is operations and maintenance expenditures in the year t , F_t is fuel expenditures in the year t , E_t is electrical energy generated in the year t , r discount rate, and n is expected lifetime of system or power station. The solar irradiance is free, therefore the fuel expenditure is zero, which defines the key economic advantage of solar energy compared to other sources of energy.

Eq. 1.1 may be further simplified as a figure of merit that has three major parts $\frac{\text{Cost (\$)}}{\text{Power (kW)} * \text{Lifetime (h)}}$ [6]. This simplified formulation helps with the terminology and defines opportunities for cost reduction.

The total cost of solar cell technology consists of different aspects. For example, the fabrication cost of c-Si solar modules (e.g. the cost of silicon material and wafer processing) accounts for more than 25% of the overall cost. Metallization and miscellaneous costs contribute an additional $\sim 10\%$ of the overall cost of a module per

Watt peak [7, 8]. A thin-film technology (e.g. CdTe, organic PV, or perovskite PV) with reduced material cost and faster throughput would reduce LCOE significantly.

Another key driver of LCOE is the power output of solar cell technology. In addition to improvement in cell technologies (e.g. passivated emitter rear-contact, PERC, or heterojunction with intrinsic thin layer, HIT), the output power can be improved by tracking the sunlight instead of using a fix-tilt rack for installation of the panels. Also, bifacial modules that allow light absorption from the backside of the panels enhance the energy output of the panel. Stacking more than one material that absorbs the sunlight in one solar cell is another way to improve the efficiency and output energy of a module. The resulting structure is called a tandem solar cell and it absorbs a broader range of the solar spectrum. Fig. 1.3 shows how these technologies, either independently or in combination, can reduce the LCOE significantly. Finally,

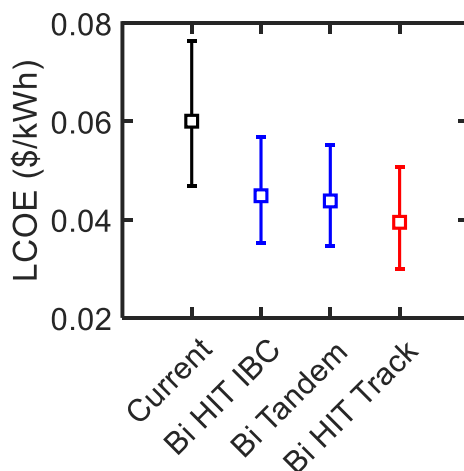


Fig. 1.3. LCOE improvement of HIT cells if the structure is conventional, bifacial, bifacial tandem, or when sun tracking is utilized.

increasing lifetime by making solar cells more reliable provides another opportunity to reduce cost. By industrial standards, a panel is replaced when its efficiency reduces below 80% of its initial power output. Although the panel can still generate energy, the system is not economically viable. The lifetime plays an important role in reducing the LCOE as shown in Fig. 1.4. The LCOE has been calculated for Kansas City in

Missouri (MO) as an example of a city that has an average amount of solar irradiation in the US. If the lifetime increases from 10 years to 25 years then the LCOE improves 35%.

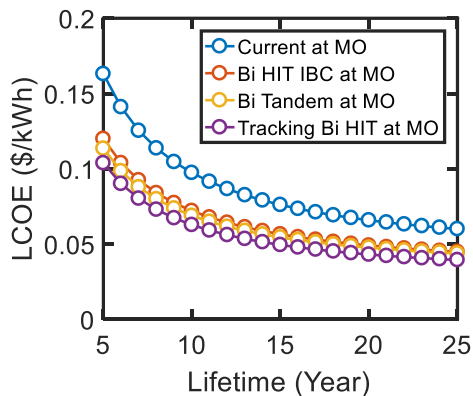


Fig. 1.4. LCOE as a function of the lifetime of the solar panel at Kansas City, MO.

1.2 Techniques of LCOE Reduction Discussed in This Thesis

As mentioned earlier LCOE includes three major parts. The first part is the cost that starts from fabricating the panel, transportation, installation, land cost, the balance of system, etc. to decommissioning. The second part is the energy produced by the panels that depend on the location of the panel and efficiency. The third part is the lifetime of the solar panel which shows the durability and reliability of the panel. To decrease the LCOE one needs to reduce the cost during the lifetime, increase the energy output, and then enhance the lifetime of the panels. The chapters are arranged to explore ways to improve each part of the LCOE.

1.2.1 Decreasing the Cost by using Thin-Film Solar Cell Technology

As discussed earlier, wafer processing and silicon material make more than 25% of the fabrication cost of c-Si solar modules. Therefore, in chapter 2, we analyze

the performance limits of perovskite solar cells as a way to decrease the cost of fabricating solar cells and panels. The solution processing of the perovskite cells makes it a cheaper fabrication process. Also due to high light absorption of the perovskite material, a perovskite absorber (~ 200 to 450 nm [9, 10] can be 1000 times thinner compared to silicon or poly-Si absorber (~ 100 to 200 μm) [11, 12]). The thin-film perovskite is amenable to a roll-to-roll fabrication process method. This method helps with faster material to product which means higher throughput [13–15]. We conclude Chapter 2 by explaining why c-Si and perovskite solar cells achieve comparable efficiency.

1.2.2 Increasing the Energy Output by Using Silicon-Perovskite Tandem Solar Cells

In chapter 3, we discuss the potential use of the silicon-perovskite tandem solar cells to further increase the energy output of a solar farm. By adding a lower bandgap sub-cell (i.e. silicon to the perovskite), we can absorb a larger fraction of the solar spectrum and enhance the energy output of the system. However, we have to use a bifacial tandem structure to alleviate the constraints of the current matching and thickness sensitivity of the perovskite sub-cell. Therefore, we will first explore the issues of optimizing a series-connected mono-facial perovskite-silicon tandem structure. Then address them by using a bifacial tandem structure.

1.2.3 Increasing the Lifetime/Reliability of Perovskite Solar Cells

The existing 3D perovskite solar cells are not sufficiently reliable to be cost-competitive and integrated silicon solar cells. In chapter 4, we investigate the lifetime of bulk perovskite solar cells at room temperature and compare it to a 2D perovskite material called Ruddlesden-Popper (RP). Due to organic slabs between the inorganic layers of the RP perovskite, this material has higher formation energy and protection against moisture. Therefore, the 2D RP perovskite is intrinsically more reliable

compared to 3D or bulk perovskite. Then we propose an energy landscape that explains the thickness and temperature dependence of this material compared to 3D perovskite. The final section of this thesis focuses on the degradation mechanisms of the c-Si solar panels.

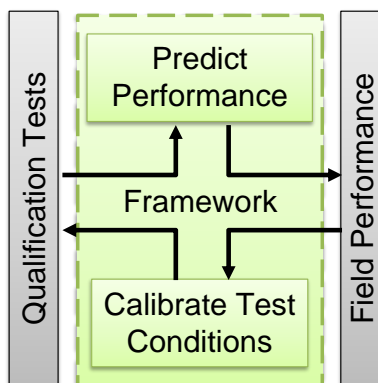


Fig. 1.5. Tests help forward modeling framework that predicts life-time/performance and by using field data framework can help calibrating test conditions.

1.2.4 Degradation Modes and Potential Increase of c-Si Projected Lifetime

Solar manufacturing companies guarantee their products for 25 to 30 years before it fails. The lifetime projection is based on accelerated and standard tests to evaluate the reliability of their products. The standard tests are designed by national or international agencies to check the quality of the products. For example, IEC 61215 is a test sequence to determine whether the module is capable of withstanding the prolonged exposure to in climates described in the scope of the test. It was designed and revised by the international electrotechnical committee (IEC). It includes damp heat test, thermal cycling test, hail test, etc. as a sequence [16]. It is a pass or fails circumstance and if the product withstands the test then it will be certified. However, depending on the location of the module worldwide, the sequence may be too harsh

or not harsh enough compared to real conditions. In the final chapter we will discuss a method called forward modeling to help predict the lifetime and energy output based on the environmental data and standard (qualification) tests as shown in Fig. 1.5 [17].

There is an emerging consensus that improving a deeper understanding of the degradation pathways and region-specific design of silicon solar cells may increase the lifetime and reduce the LCOE of c-Si cells. In chapter 5, first, we describe how corrosion and delamination of the contacts along with solder bond failure impact the output power and J-V characteristics of the solar cells/panels through simulation. We will see that finger thinning manifests itself as a "fake shunt" resistance in the J-V curves and may be mistaken with the real shunt. Also, we show that solder bond failure causes the series resistance to increase both at the cell and module level.

In chapter 6, we validate the simulation results of solder bond failure via dark lock-in thermography (DLIT), photoluminescence (PL), and electroluminescence (EL) measurements. We explain how DLIT specifically helps to locate the hotspots created by the solder bonds that failed locally in a panel. Then we realize that by measuring the series resistance of the panels we can identify the panels that suffer from solder bond failure without the need to disassemble them and do the aforementioned measurements in the laboratory.

In chapter 7, we develop a model that predicts the impact of the solder bond failure on the lifetime of a cell/module. We start from a semi-empirical model that calculates the damage accumulated in the module due to daily and seasonal temperature variation. Then use a relationship between the number of broken bonds and damage to find the performance at the cell level as a function of time. We then include the statistical nature of the solder bond failure at the module level to predict the lifetime and performance at the module level.

This modeling is a part of an extensive model that can predict the performance of the solar panels installed in the field. These panels may undergo many degradation mechanisms simultaneously that have intertwined impacts on the performance of the

panels. Since we already know the electrical signature of each mechanism i.e. how they impact photo-generation, shunt resistance, series resistance, or saturation diode currents, we can forecast the energy output. Needless to say, we need to know the initial condition of the module and have access to possible weather data based on the location of the installation.

This is called forward modeling since we do not possess the performance data of the panels installed in the field. If we have access to the output power of a fielded panel, is it possible to backtrack the degradation mechanisms and predict future performance more accurately? That is the topic of future work and we call it reverse modeling. This modeling helps us calibrating the forward modeling parameters needed for our prediction.

Such modeling provides the necessary information for the solar companies pinpointing the bottleneck of their products that are shipped to be installed in the field. Also, it helps financial institutions should they want to invest in solar energy and analyze the risk and return of investment. In addition, since solar energy is not available the whole day long we need to include other sources of energy as a hybrid to ensure the continuity and reliability of generated electricity. To do so one needs an accurate weather forecast in collaboration with a model that predicts the output energy in real-time so that other sources can compensate when the solar energy is not meeting the energy demand. Finally, we summarize and conclude the thesis.

1.3 Conclusions

Our thesis is focused on reducing LCOE based on new material technology (e.g. perovskite solar cells), innovative cell technology (e.g. silicon-perovskite bifacial tandem), and a deeper understanding of location-specific reliability based on forward and inverse modeling (e.g. solder bond failure). However, we must emphasize that there are other important system considerations not discussed in this thesis. For example, there is an important issue of generation vs. demand of the energy or the

”duck chart”. Briefly, the solar energy generation peaks during the afternoon (i.e. generally from 12 pm to 3 pm), while the demand peaks during the evening after the sun has set. To resolve this issue, one may use fossil-fuel-based power-plants to support the excess-load, or develop extensive energy storage infrastructure [18, 19] to funnel energy generated during the day to satisfy night time demand. Recycling of the solar module is another concern not reflected in the LCOE. In short, only a comprehensive and integrated perspective can define a clear pathway regarding the emergence of renewable energy as the dominant and sustainable source of energy for the global population.

2. BULK PEROVSKITE SOLAR CELL

Note: The material in this chapter has been adapted from Ref. [20]

State-of-the-art photovoltaics utilize high-purity, large-area, wafer-scale single-crystalline semiconductors grown by sophisticated, high temperature crystal-growth processes. Here, we demonstrate a new solution-based hot-casting technique to grow continuous, pin-hole free thin-films of organometallic perovskites with millimeter-scale crystalline grains. Our collaborators at Los Alamos National Laboratory (LANL) fabricated planar solar cells with efficiencies approaching 20%, with little cell-to-cell variability. The devices show hysteresis-free photovoltaic response, which had been a fundamental bottleneck for stable operation of perovskite devices. Our simulation and modeling attribute the improved performance to reduced bulk defects and improved charge carrier mobility in large grain devices. We anticipate that this technique will lead the field towards synthesis of wafer-scale crystalline perovskites necessary for the fabrication of high-efficiency planar solar cells and be applicable to several other material systems plagued by defects and grain boundary recombination in solution-processed thin-films.

2.1 Introduction

Perovskite solar cells were first reported in 2005, when the use of perovskite as the new absorber in a dye-sensitized solar cell (DSSC) increased its efficiency from 0.4 to 2.1% [21]. The cell structure has evolved over time and the efficiency increased further when solid-state hole transport material [22] replaced the liquid ionic conductor. Fig. 2.1 [23] shows the rapid progress of perovskite solar cells in comparison with some other thin-film technologies. A typical high-efficiency heterojunction perovskite solar cell uses solid state electron transport material (ETM) and hole transport material

(HTM) as charged carrier collectors. The perovskite absorber sandwiched in the middle of ETM and HTM can be a p-type material (p-p-n structure) or an intrinsic material (p-i-n structure). This structure reaches a high efficiency of 22.7% that is close to highest c-Si efficiency of 26.1% [24]. We want to explain the reasons behind such high efficiency of perovskite and ways the efficiency could be improved further.

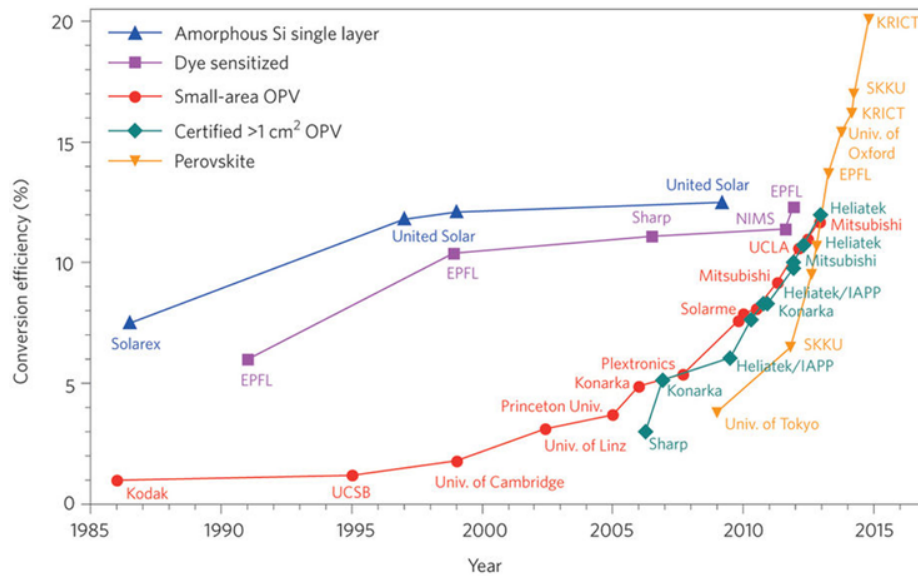


Fig. 2.1. Progress of perovskite solar cells compared to other thin-film technologies

Recent discovery of organic-inorganic perovskites offers promising routes for the development of low-cost solar-based clean global energy solutions for the future [25–28]. Solution-processed organic-inorganic hybrid perovskites planar solar cells, such as $CH_3NH_3PbX_3$ ($X = Cl, Br, I$) have achieved high average power conversion efficiencies (PCE) of $\sim 16\%$ using Titania based planar structure [25–31] or $\sim 10\text{--}13\%$ in the PCBM based architecture [32–34]. Such high PCE has been attributed to strong light absorption and weakly-bound excitons that easily dissociate into free carriers with large diffusion length [35–37]. The average efficiency is typically lower by 4–10% compared to the reported most efficient device, indicating persistent challenges of stability and reproducibility. Moreover, hysteresis during device operation, possibly due

to defect assisted trapping, has been identified as a critical roadblock to the commercial viability of perovskite photovoltaic (PV) technology [38–41]. Therefore, recent efforts in the field have focused on improving film surface coverage [42], increasing the crystal size and improving crystalline quality of the grains [43], which is expected to reduce the overall bulk defect density and mitigate hysteresis by suppressing the charge trapping during solar cell operation. Although approaches such as thermal annealing [44, 45] varying of precursor concentrations and carrier solvents [46] and using mixed solvents [47] have been investigated, control over structure, grain size and degree of crystallinity remain key scientific challenges for the realization of high performance devices.

2.2 Hot-casting Method Improves Efficiency by Increasing Grain Size

In this chapter, we report a solution-based hot-casting technique to achieve $\sim 18\%$ efficient solar cells based on mm-scale crystalline grains, with relatively small variability ($\sim 2\%$) in the overall PCE from one solar cell to another. Fig. 2.2a schematically describes our hot-casting process for deposition of organometallic perovskite thin-films. Our approach involves casting a hot ($\sim 70^\circ\text{C}$) mixture of PbI_2 and MACl solution onto a substrate maintained at a temperature of up to 180°C and subsequently spin-coated (15 sec) to obtain a uniform film (Fig. 2.2a). In the conventional scheme, the mixture of lead iodide (PbI_2) and methylamine hydrochloride (MACl) is spin-coated at room temperature and then post-annealed for 20 min on a hot plate maintained at 100°C . Fig. 2.2b-d illustrates the obtained crystal grain structures using this “hot-casting” technique for various substrate temperatures and processing solvents. We chose PbI_2 and MACl molar ratio of 1:1 in all experiments described in this report to achieve the basic perovskite composition and the best morphology. We observed large, mm-scale crystalline grains, with a unique leaf-like pattern branching out from center of the grain.

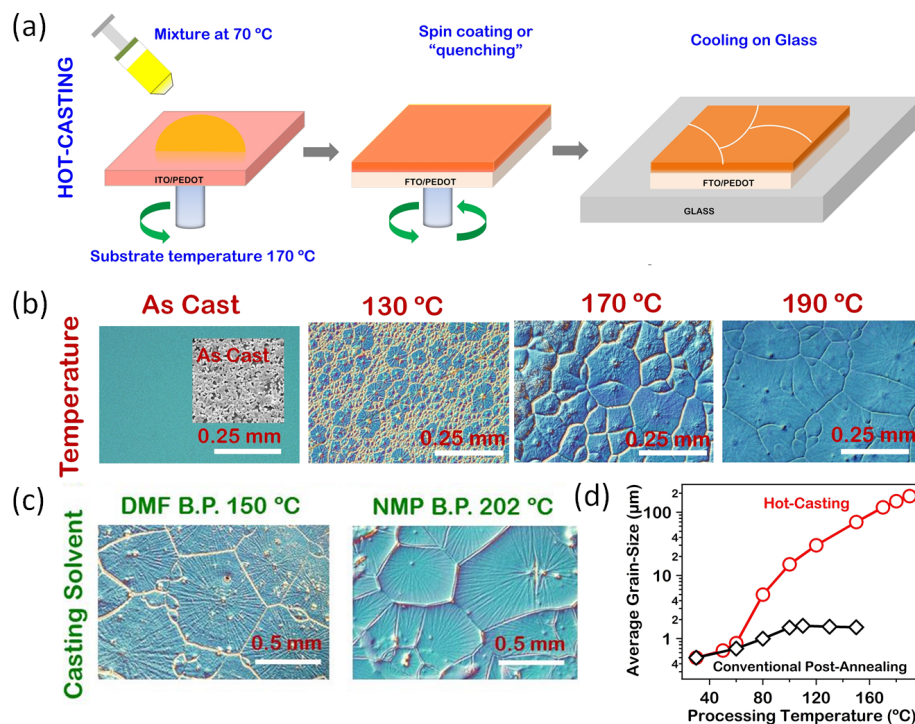


Fig. 2.2. Processing scheme for perovskite thin-film using hot casting methods and observations for large-area mm-scale crystal grain formation for perovskite ($PbCH_3NH_3I_{3-x}Cl_x$) based thin-film. (a) Hot-casting scheme for large-area crystal growth. Optical micrographs illustrating grain formation as a function of substrate temperature with the casting solution maintained at ($70^\circ C$) and (b) Large area grain formation using casting solvents with high boiling points. (c) Compares the grain size as a function of processing temperature obtained for the hot-casting and the conventional post-annealing methods for the substrate processing temperature.

The grain size increases dramatically as the substrate temperature (Fig. 2.1b, d) increases from room temperature up to $190^\circ C$ or using solvents with a higher boiling point (N-Methyl-2-pyrrolidone, NMP) (Fig. 2.2c). Our method leads to grain sizes of 1-2 mm, in comparison with the $\sim 1 - 2\mu m$ size grains obtained using the conventional post-annealing process. The major difference between hot-casting and conventional post-annealing is the presence of solvent when heating the substrate. For hot-casting, there is excess solvent present when the substrate is maintained above

the crystallization temperature for the formation of the perovskite phase. This allows for the prolonged growth of the perovskite crystals, yielding large crystalline grains.

Thus, the use of high boiling point solvents such as DMF or NMP (Fig. 2.2b) provides the ideal conditions for the growth of large crystalline grains as the excess solvent allows more time for the growth of large grain size crystal. Optical (Fig. 2.2b, c) microscopy illustrates that the perovskite thin-films produced with the hot-casting method (from $100^{\circ}C$ up to $180^{\circ}C$) are uniform, pin-hole free and cover the entire substrate.

Our collaborators fabricated the mixed-halide organometallic perovskite photovoltaic devices using the hot-casting technique in planar device architecture as illustrated in Fig. 2.3a. The current-voltage curves for device fabricated at various temperatures measured under simulated AM 1.5 irradiance at $100mW/cm^2$ calibrated using a NIST certified mono-crystalline Si solar cell (Newport532 ISO1599) are illustrated in Fig. 2.3b. During measurements, a mask was used to confine the illuminated active area to avoid edge effects. The PCE (left) and short-circuit current density (J_{SC}) (right) are plotted as a function of perovskite grain size in Fig. 2.3c. An optimal perovskite film thickness of $\sim 450nm$ was fixed for all devices to exclude variations in optical absorption or interference effects due to changes in film thickness. We observed a dramatic increase in J_{SC} ($3.5mA/cm^2$ to $22.4mA/cm^2$, 2.3c), open circuit voltage (V_{OC}) (0.4 V to 0.92 V, Fig. 2.4a) and fill factor (FF) (0.45 to 0.82, Fig. 2.4b) when the grain size increases from $\sim 1\mu m$ up to $\sim 180\mu m$, which translated to an increase in the overall PCE from 1% to $\sim 18\%$. The J_{SC} of the devices are in good agreement with the calculated J_{SC} obtained by integrating the external quantum efficiency (EQE). In addition to the high PCE, we found that the solar cell device performance was hysteresis free, with negligible change in the photocurrent density with either the direction of voltage sweep or the scan-rate (or voltage delay time) (Fig. 2.3d, e). The devices exhibited a high degree of reproducibility in the overall PCE as illustrated in Fig. 2.3f.

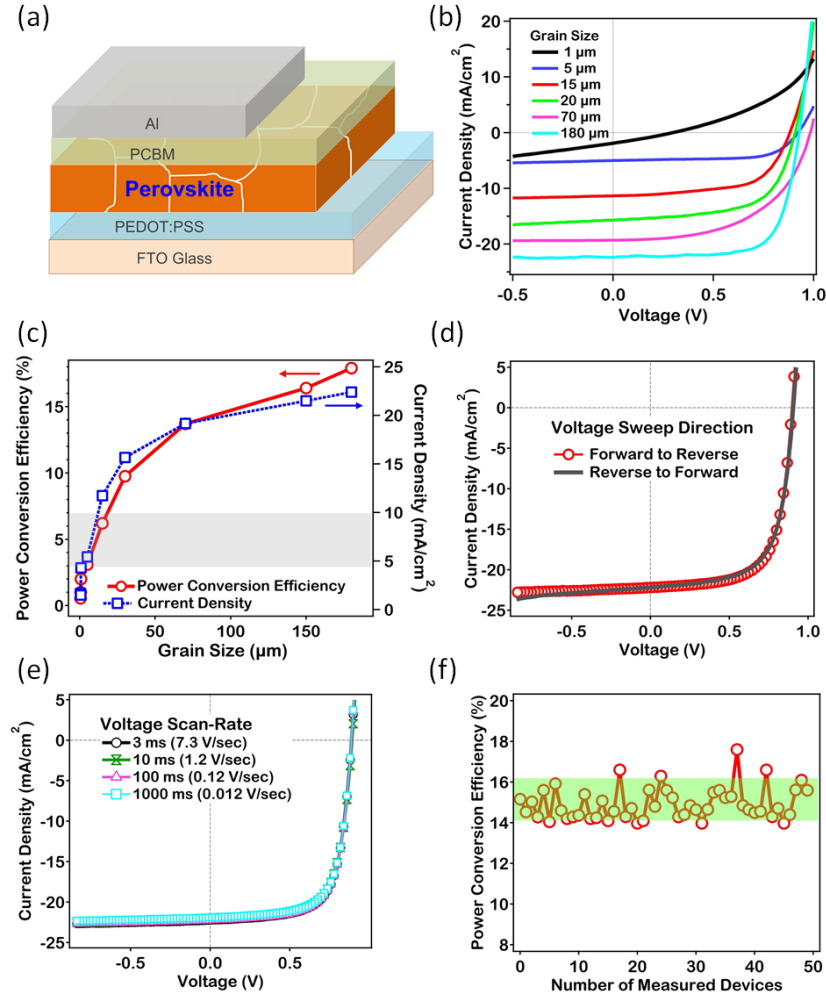


Fig. 2.3. Solar cell device architecture and performance (a) Planar device configuration used for this study and (b) J-V curves obtained under AM 1.5 illumination and (c) overall PCE (left) and J_{SC} (right) as a function of crystalline grain size. Grey box represents the range of PCE obtained using the conventional post-annealing process. (d) Average J-V characteristics resulted by sweeping the voltage from forward to reverse and reverse to forward bias demonstrates the absence of hysteresis. These were curves were obtained by averaging 15 sweeps in each direction. (e) J-V curves at different voltage scan-rates in voltage delay time (ms) or Volts/sec again demonstrate negligible hysteresis. (f) Describes the variation in the PCE for 50 measured devices.

High performance cells have previously been reported with micron-sized grains [25, 48–50], therefore, we believe that there are two primary benefits of growing crys-

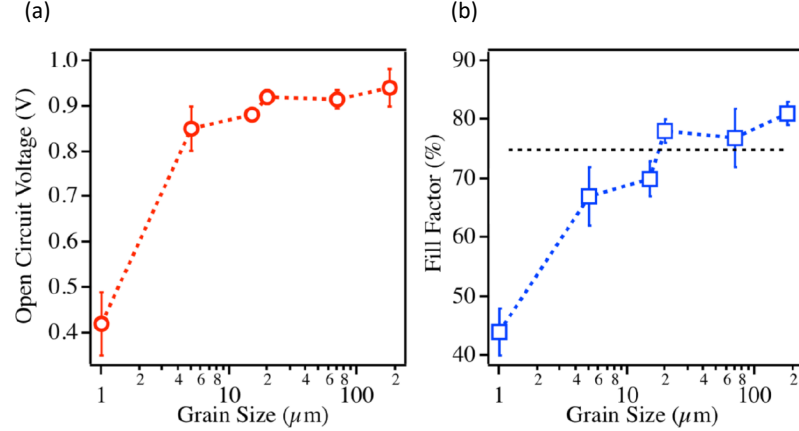


Fig. 2.4. Solar cell parameters measured under AM 1.5 illumination. (a) Open circuit voltage (V_{OC}) and (b) FF extracted from J-V curve under AM 1.5 illumination at 100 mW/cm^2 solar simulator for planar perovskite solar cell as a function of grain size.

tals with large grain size: First, reduced interfacial area associated with large grains suppresses charge trapping, and eliminates hysteresis (regardless the direction of voltage sweep or the scan-rate); second, larger grains have lower bulk defects and higher mobility, allowing for the photo-generated carriers to propagate through the device without frequent encounters with defects and impurities.

The current-voltage characteristics in Fig. 2.3b support the hypothesis. For example, the reduction in defect-assisted recombination in larger grains is reflected in the observed increase in the V_{OC} from 0.4 V to 0.94 V and fill factor from 0.4 to 0.83 with increase in grain size. The short circuit current of $J_{SC} = 22.4 \text{ mA/cm}^2$ is at par with the highest values reported in literature. Indeed, the measured J_{SC} , V_{OC} and FF values for the large grain device compare favorably with the Shockley–Queisser theoretical limit ($J_{SC} \sim 26.23 \text{ mA/cm}^2$, $V_{OC} \sim 1.02 \text{ V}$, and $FF \sim 0.90$) for the given device architecture and band-alignment.

2.3 Simulation Framework

We performed a self-consistent optoelectronic simulation involving solution of Maxwell, Poisson, and drift-diffusion equations as follows. These simulations support the hypothesis of improved material quality for larger grains as discussed later (see Fig. 2.3a-c).

2.3.1 Optical Modeling

Optical absorption in different layers of the OPV cell is calculated by the full-wave solution of Maxwell's equations with the input of AM 1.5 illumination. The materials in different layers of the cell are characterized by absorption coefficient and refractive indices that are obtained from literature [51–53]. Transfer matrix method (TMM) [54] calculations are used for the optical studies of the planar cell structure. In this approach, the entire solar cell stack, including the contact layers, is modeled using a series of interface and phase matrices. The central quantity which is calculated in this approach is the point-wise optical absorbance $[A(\lambda, r)]$ inside various layers of the cell. The wavelength range of 300–900 nm has been used for our calculations. The spatially-resolved absorption profile is integrated over the wavelength range to create the generation profile for the electron and holes for self-consistent carrier transport simulation, as described below.

2.3.2 Self-consistent transport simulation

The transport of charged carriers (electrons and holes) is modeled by generalized drift-diffusion formalism [55]. Photo-generation is calculated from the optical absorption profile (integrated over the wavelengths) discussed in the previous sub-section. The electron and hole transport inside the cell is simulated by a self-consistent solution of Poisson and continuity equations by a commercial grade device simulator *MEIDCITM* [56]. The generation term in the e–h continuity equations is calculated

from the solution of photo-generated profile. The recombination term in continuity consists of direct and SRH recombination with life time found from literature. We do not account for hot electron effects. The excitons – if any – are presumed to dissociate into free electron and hole pairs immediately after generation. See Table 2.1 for model equations and see Table 2.2 for simulation parameters. The parameters with references are taken from the literature; the rest are assumed to match the data for single grain size. We emphasize that the parameterization is not arbitrary: the parameters obtained by fitting the J-V characteristics of single grain size are held fixed for all other grain sizes; the J-V data for samples with other grain sizes are reproduced without any further parameterization except for mobility and slight change in band-alignment.

Table 2.1.
Equations for carrier transport

Name	Equation
Poisson	$\epsilon_r \epsilon_0 \nabla^2 \psi = -q (n_h - n_e)$
Continuity	$\nabla J_{e,h} = (G_{e,h} - R_{e,h}(n_e, n_h))$
Drift-Diffusion	$J_{e,h} = \mu_{e,h} n_{e,h} (-\nabla \psi) \pm D_{e,h} \nabla n_{e,h}$
Recombination	$R_{e,h}(n_e, n_h) = B (n_e n_h - n_i^2) + \frac{n_e n_h - n_i^2}{\tau(n_e + n_h)}$

2.3.3 Importance of grain sizes for electronic transport of electrons and holes

Fig. 2.5 (a) and Fig. 2.5 (b) indicate the importance of bulk grain size in dictating the cell performance: the higher mobility of larger grains suppresses bulk recombination and allows a more efficient collection of charges via drift dominated transport. Specifically, any increase in the bulk mobility reduces the hole and electron concen-

Table 2.2.
The simulation parameters used in numerical simulation of Perovskite cell

Properties	PEDOT:PSS	Perovskite	PCBM
Thickness	40nm	350nm	20nm
Doping (cm^{-3})	$N_A = 3 \times 10^{17}$	$N_A = 1 \times 10^{16}$	$N_D = 5 \times 10^{17}$ [57]
Hole mobility (cm^2/Vs)	9×10^{-3} [58]	1.0	1×10^{-2}
Electron mobility (cm^2/Vs)	9×10^{-3}	1.0	1×10^{-2} [57]
Hole lifetime (s)	1×10^{-6}	9.6×10^{-9}	1×10^{-6}
Electron lifetime (s)	1×10^{-6}	9.6×10^{-9}	1×10^{-6}
Bandgap (eV)	1.55 [59]	1.55 [60]	2.0 [61]
Electron affinities (eV)	3.63	3.73 [62]	4.13 [63]
Contact properties	Ohmic contacts, $s_f = 10^7 cm/s$ for both contacts		

trations within the absorber (solid vs. dashed lines in Fig. 2.5(a)). The reduction in electron and hole concentrations, in turn, reduces Shockley-Read-Hall recombination (see Fig. 2.5(b)) and improve PCE. In addition, it appears that self-doping is reduced considerably for larger grains. As a result, the absorber is fully depleted and will have high electric field inside. Therefore, the transport of charge carriers is dominated by drift and the charges are efficiently collected by the respective contacts. Finally note that, the PCBM-perovskite interface acts as the dominant source of recombination for the larger grain cells. This suggests that even higher efficiency might have been achieved if this recombination could be suppressed by (i) passivating the interface to reduce the defect density, and by (ii) improving the matching between the mobilities

of the PCBM and perovskite layers so that the charge build-up at the interface is suppressed (see inset in Fig.2.5 (a)).

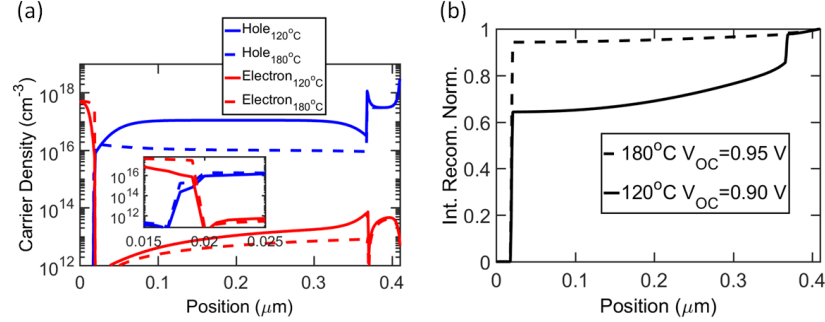


Fig. 2.5. Carrier densities and recombination profiles within small and large grain solar cells: (a) Carrier densities inside the cell at the open circuit condition for small grain cells processed at 120°C (solid lines) and large grain cells processed at up to 180°C (dashed lines), respectively. The inset magnifies the carrier concentrations at the PCBM-Perovskite interface. (b) Corresponding normalized cumulative recombination rates inside the cell for small grain cells (solid line) and large grain cells (dashed line), at the open circuit condition.

Based on independently calibrated material parameters summarized in Table 2.2 and bulk defect density and mobility as fitting parameters and a slight change of bandgap, Fig. 2.6a illustrates that the model quantitatively reproduces all the salient features of the J-V characteristic of both 17.7% (large grain) and 9.1% (small grain) cells. The key to the efficiency gain is the suppression of defect-assisted recombination in the bulk region: it contributes to 5% charge carrier loss in large grain cells (vs. 40% loss in devices with smaller grains), see Fig. 2.5(b). Moreover, the energy band diagram of large grain 17.7% cell (Fig 2.6b) shows that the absorber region is fully depleted and the built-in electrical field and the high mobility allows efficient charge collection. Consistent with the hypothesis, we find that the experimental results can be interpreted only if one assumes that mobility is correlated to grain size (Fig. 2.6c).

To understand recombination of photogenerated carriers during device operation, we measured V_{OC} as a function of light intensity for large- and small-grain devices

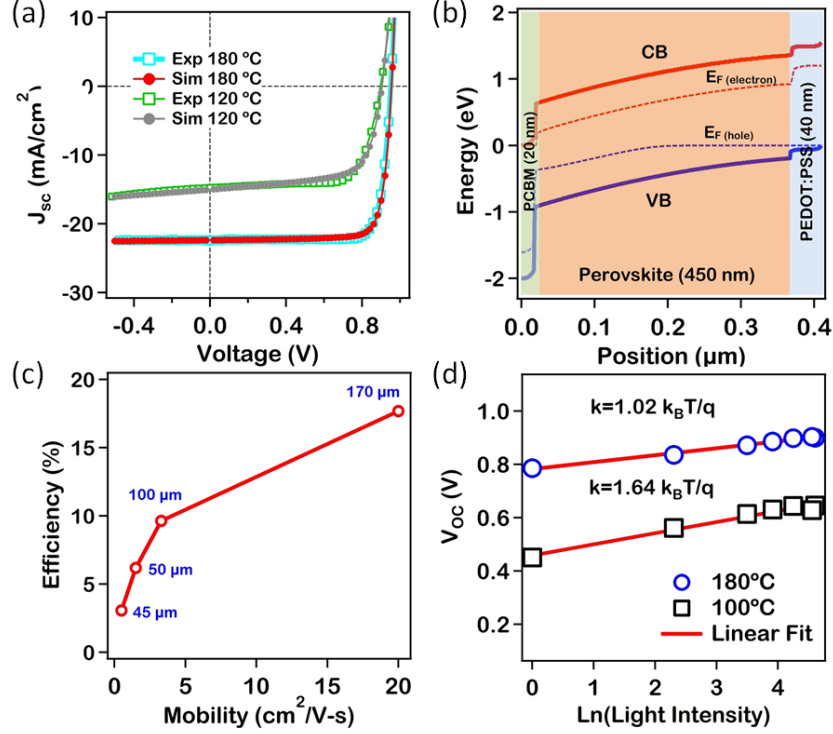


Fig. 2.6. Self-consistent device simulation attributes the process-dependent PCE gain to the improved mobility of films with larger grains. (a) The simulated J-V characteristics for large- and small-grain devices reproduce the salient features of the corresponding experimental data. (b) Typical energy band diagram at short circuit (SC) indicates the importance of a semi-intrinsic (reduced self-doping) fully depleted absorber in directing the charge carriers to their respective contacts; otherwise, the charge carrier would be lost to recombination in the field-free regions. (c) With all other parameters characterized and/or obtained from the literature, the PCE values appear to be correlated to the bulk mobility of the absorber (labels correspond to the average grain size). (d) Experimental data for V_{OC} as a function of illumination light intensity for a large-grain device (180°C) and a small-grain device (100°C) along with the linear fit (red line).

(Fig. 3D). By linearly fitting V_{OC} versus log-scaled light intensity [$\ln(I)$], we obtained a slope of $\sim 1.0 k_B T/q$ (where k_B is the Boltzmann constant, T is absolute temperature, and q is elementary charge) for a large-grain device (hot-cast at 180°C), which suggests that SRH recombination process dominates during device operation [64–66],

similar to that observed in high quality semiconductors such as silicon and GaAs. In contrast, for the small-grain device (hot-cast at 100°C), a slope of $1.64 k_B T/q$ is measured, that is an indicator of trap-assisted recombination

2.4 Summary and Conclusion

To summarize, we have developed a new approach for crystal growth that achieves macroscopic (mm-scale) grain sizes in organometallic perovskite thin-films deposited from solution. These films yield solar cells with PCE values approaching $\sim 18\%$, which is among the highest reported in the field of perovskite-based light-to-energy conversion devices. Most importantly devices with large grain size are free of degradation commonly observed with the direction or the scan-rate of the applied voltage, suggesting that larger grains reduce interfacial area for charge trapping and help improve the bulk crystalline property by reducing bulk defect density and enhancing mobility. This hypothesis is supported by self-consistent device modeling, as well as spectrally, temporally-resolved optical spectroscopy studies and dependence of V_{OC} on light intensity. Further enhancement in efficiency can come by improving the interface between Perovskite/PCBM, matching mobility, better band-alignment and using an inverted structure. From the perspective of the global photovoltaics community, these results are expected to lead the field towards the reproducible synthesis of wafer-scale crystalline perovskites necessary for the fabrication of high-efficiency single-junction and hybrid (semiconductor and perovskite) tandem planar cells. The possible tandem structure will be discussed in detail in the next chapter to investigate the potential of combining the best features of c-Si and perovskite cells.

3. BIFACIAL PEROVSKITE-HIT TANDEM STRUCTURE TO PRODUCE HIGHLY EFFICIENT SOLAR CELL

Note: The material in this chapter has been adapted from Ref. [67]

As single junction PV technologies, both Si heterojunction (HIT) and perovskite based solar cells promise high efficiencies at low cost. Intuitively, a traditional tandem cell design with these cells connected in series is expected to improve the efficiency further. Using a self-consistent numerical modeling of optical and transport characteristics, however, we find that a traditional series connected tandem design suffers from low J_{SC} due to band-gap mismatch and current matching constraints. Specifically, a traditional tandem cell with state-of-the-art HIT ($\eta = 24\%$) and perovskite ($\eta = 20\%$) sub-cells provides only a modest tandem efficiency of $\eta_T \sim 25\%$. Instead, we demonstrate that a bifacial HIT/perovskite tandem design decouples the optoelectronic constraints and provides an innovative path for extraordinary efficiencies. In the bifacial configuration, the same state-of-the-art sub-cells achieve a normalized output of $\eta_T^* = 33\%$, exceeding the bifacial HIT performance at practical albedo reflections. Unlike the traditional design, this bifacial design is relatively insensitive to perovskite thickness variations, which may translate to simpler manufacture and higher yield.

3.1 Background and Motivation

In recent years, the search for low-cost highly efficient solar cells has resulted in two cell technologies (inorganic a-Si/c-Si heterojunction and organic perovskite) with comparable, but complementary characteristics. On one hand, the standard a-Si/c-Si heterojunction (HIT) technology is poised to capture a significant proportion of traditional c-Si solar cells due to its high efficiency and better temperature coefficients.

[68, 69] On the other hand, the recent dramatic gain in efficiency of perovskite cells promises to finally realize the presumed cost advantages of organic solar cells. [32, 70, 71] With significant efforts in device analysis [72–77] and optimization [78–81], several groups have achieved efficiency $\eta \geq 22\%$ HIT cells. [82] In the case of perovskite based solar cells, with improvements in processing and material quality, the state-of-the-art cells have reached an efficiency of $\sim 20\%$. [83–85]

A perovskite/HIT tandem design that can suppress individual bottlenecks and take advantage of their complementary characteristics may improve the efficiency further. Recently, the efficiency gain of tandem designs with perovskite as the top cell and a range of bottom cell have been explored. Using a four terminal configuration, Bailie et al. [86] obtained a 17% and 18.6% efficient tandem cell with mc-Si ($\eta \sim 11\%$) and copper indium gallium selenide (CIGS, $\eta \sim 17\%$) bottom cells, respectively. Similarly, Löper et al. [87] obtained a 13.4% efficient tandem cell with presumably a highly efficient a-Si:H/c-Si heterojunction bottom cell using the same configuration. Finally, Mailoa et al. [88] used a c-Si bottom cell in a two terminal tandem design to demonstrate a 13.7% cell. These studies indicate that a poor performing top cell can significantly limit the performance of these traditional tandem cell designs. The tandem efficiency improvement may saturate for the state-of-the-art sub-cells.

There have been some efforts to predict the theoretical limits for these traditional tandem designs using perovskite sub-cell on top of c-Si [89] or a-Si/c-Si heterojunction bottom cell. [90] These studies are generally not self-consistent; they rely only on detailed optical modeling. The conclusions based on carrier transport modelled by simple one-diode compact model may not be definitive, at least in the case of a-Si/c-Si heterojunction solar cells. [74]

From the above discussion, we observe that there have been some efforts to push the practical conversion efficiency using the traditional tandem designs. However, the gain using traditional tandem designs is not significant and theoretical limits based on fully self-consistent optoelectronic simulations are still lacking. In this chapter, using detailed optical and carrier transport modeling, first, we re-explore the traditional

tandem cell design. Starting from state-of-the-art cell parameters for the sub-cells ($\sim 20\%$ efficient perovskite cell, $\sim 24\%$ efficient HIT cell), an optimized tandem cell offers only a modest improvement, $\eta_T \sim 25\%$. Moreover, the optimization dictates a strict control over the perovskite layer thickness —even a $\sim 20\text{nm}$ deviation from the optimum thickness would degrade the net efficiency by 1%.

Instead, we suggest that another design involving a HIT and perovskite bifacial tandem cells can circumvent the constraints of the traditional design, and increase the normalized output to $\eta_T^* \sim 33\%$ (output power normalized to 1-sun). Indeed, the bifacial tandem would outperform the bifacial HIT cell for typical albedo reflection ($R_A < 40\%$). Further, the bifacial tandem design would be insensitive to the sub-cell thickness variation which obviates the need for layer optimization. The output gain is not restricted to state-of-the-art champion cells; even sub-optimal perovskite cell and standard HIT cell would benefit substantially from this strategy.

For this study, we consider a perovskite solar cell with the absorber layer ($CH_3 - NH_3PbI_3$) sandwiched between PEDOT:PSS hole transport material (HTM) and PCBM electron transport material (ETM) [34, 70] This perovskite sub-structure is then contacted by ITO and Al. A schematic of this configuration is shown in Fig. 3.1(b). The HIT cell uses c-Si as the active material with p+ and n+ doped a-Si passivation layers which act as the emitter (i.e., HTM) and the back surface field (ETM), respectively. The cell is contacted with ITO at the front and ITO/Al at the back.

The traditional tandem cell consists of the higher bandgap perovskite ($E_G^{PVK} \sim 1.55\text{eV}$) sub-structure stacked on top of the lower bandgap ($E_G^{cSi} \sim 1.12\text{eV}$) c-Si HIT-subcell (see Fig. 3.1(b)).

The bifacial tandem cell has a similar design except for the absence of an Al back contact. This allows the absorption of light reflected from the ground, as shown in Fig. 3.1(c). We will consider both traditional and bifacial tandem designs, to demonstrate why and how bifacial tandem design outperforms the traditional design.

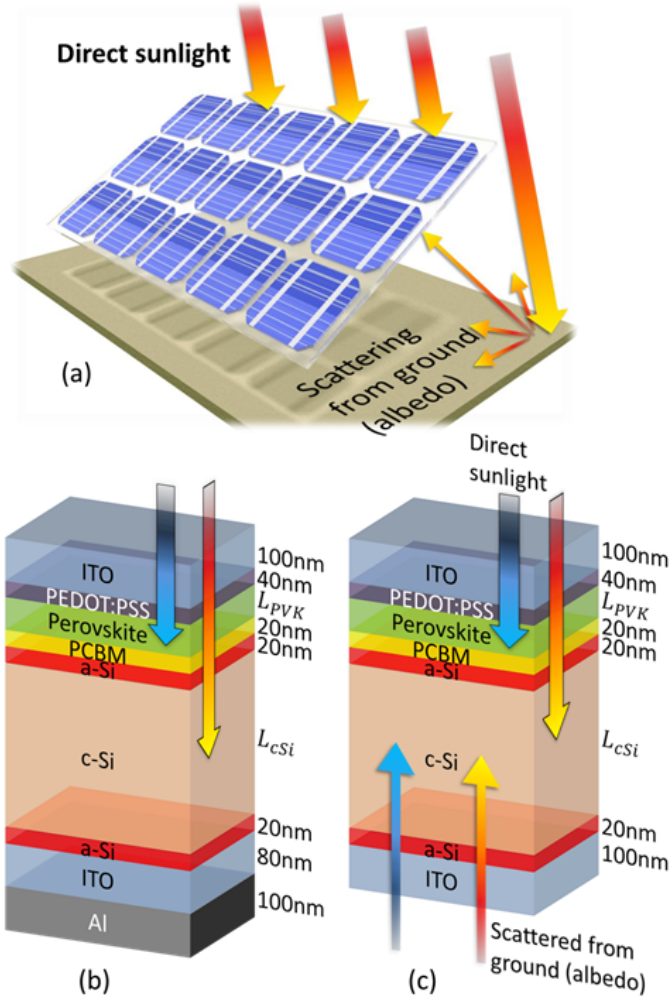


Fig. 3.1. (a) A solar panel generally utilizes the direct illumination of sunlight. A fraction of the light can also be scattered from the ground onto the back of the panel. (b) Traditional tandem structure, and (c) a bifacial tandem structure.

3.2 Simulation Framework

The absorption spectrum and the spatial photo-generation profile in the layered solar cell structure is calculated by solving the Maxwell's equations using the Transfer Matrix Method (TMM). [54] Illumination of AM 1.5G solar spectrum over the wavelength range 300–1500nm is used in this simulation. The materials in different

layers of the cell are characterized by experimentally measured absorption coefficient and refractive indices reported in the literature. [51,52,91] For this study, we assume planar structures. For the bifacial tandem, a perfect antireflective coating is assumed at the back.

Fig. 3.2 shows the absorption spectrum for the optimized tandem structure. Most of the high energy photons ($\lambda < 500nm$) are absorbed in the perovskite sub-cell. This suppresses parasitic absorption in a-Si layer, a beneficial effect of the tandem configuration. The overall thick structure with a back mirror (Al) causes Fabry-Perot-like resonances in PEDOT absorption beyond the Si band-edge ($\lambda > 1100nm$). Such oscillations would not be observed in practical systems due to surface roughness or non-uniformity of the layer thickness. For the bifacial configuration, the thick perovskite layer absorbs almost all the photons above its band-edge, as shown in Fig. 3.3. This eliminates the possibility of parasitic absorption in a-Si.

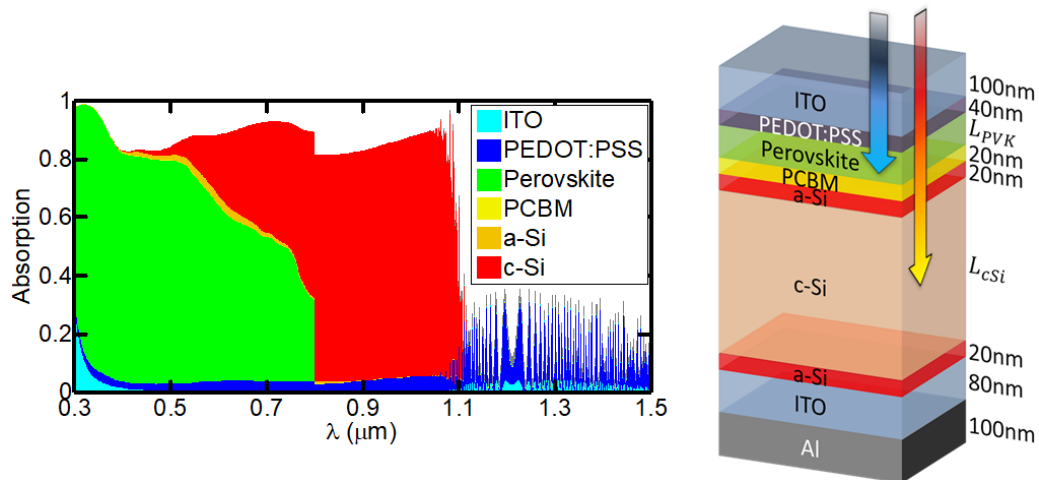


Fig. 3.2. Absorption spectrum of optimum-thickness classical tandem solar cell.

For simulation of the light incident from the bottom of the cell (in the bifacial configuration), we assumed perfect impedance matching from air into the a-Si layer (the ITO has been neglected in this case). Such matching can be achieved by anti-

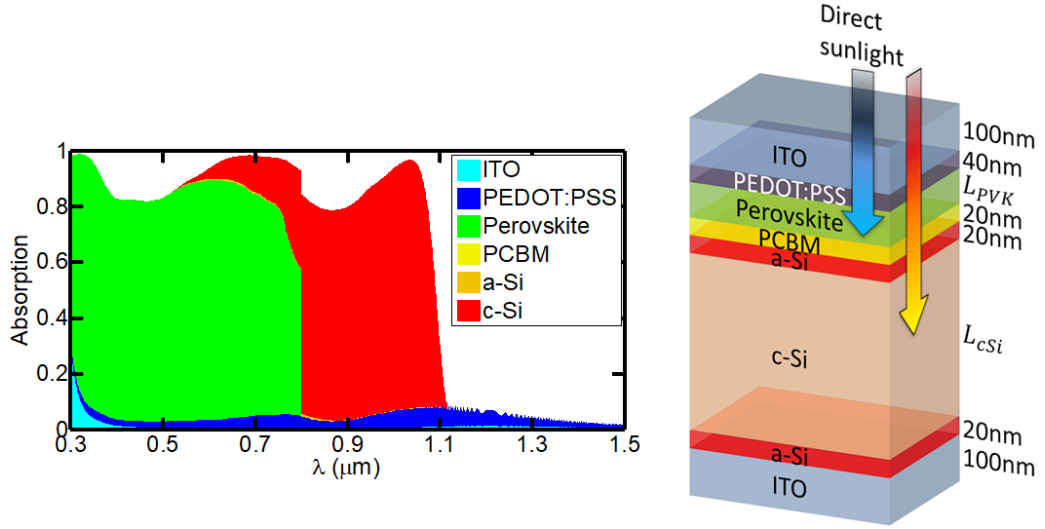


Fig. 3.3. Absorption spectrum of top incident light for bifacial tandem solar cell.

reflection coatings or by textured surfaces. In this case, as shown in Fig. 3.4, there is a significant parasitic absorption in back a-Si layer. The rest of the photons are absorbed in the c-Si (above the band-edge). Since c-Si is a material with a smaller bandgap, there is no absorption in the perovskite layer when light is incident from the back surface.

The transport of the charged carriers (electrons and holes) is modeled by the generalized drift-diffusion formalism [55], using MEDICITM device simulator. [92] The contacts are presumed to be ohmic. See Table 3.1 for model equations, and Table 3.2 and Table 3.3 for simulation parameters. The parameters are consistent with literature yielding in experimentally observed device characteristics.

Here, ϵ_r is the relative dielectric constant of the material, $n_{e,h}$ is the electron/hole concentration, $G_{e,h}$ is the generation profile coming from optical simulation, $R_{e,h}$ is the recombination term including direct and Shockley-Read-Hall recombination in case of perovskite cell and also Auger recombination in case of HIT cell, $\mu_{e,h}$ is the electron/hole mobility, $D_{e,h}$ is the electron/hole diffusion coefficient, n_i is the intrinsic

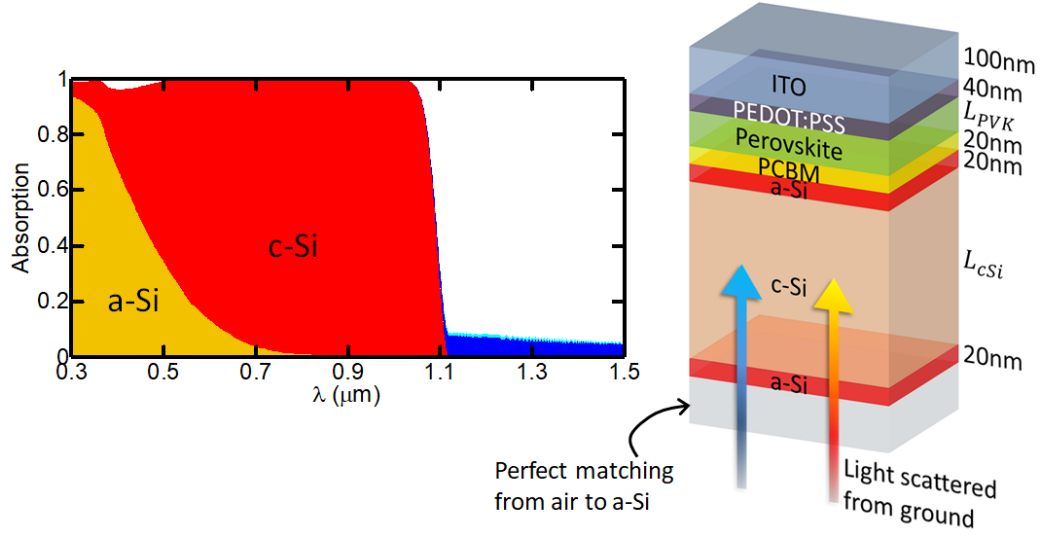


Fig. 3.4. Absorption spectrum of bottom incident light (Albedo reflection) for bifacial tandem solar cell.

Table 3.1.

Equations for carrier transport

Name	Equation
Poisson	$\epsilon_r \epsilon_0 \nabla^2 \psi = -q (n_h - n_e)$
Continuity	$\nabla J_{e,h} = (G_{e,h} - R_{e,h}(n_e, n_h))$
Drift-Diffusion	$J_{e,h} = \mu_{e,h} n_{e,h} (-\nabla \psi) \pm D_{e,h} \nabla n_{e,h}$
Recombination	$R_{e,h}(n_e, n_h) = B (n_e n_h - n_i^2) + \frac{n_e n_h - n_i^2}{\tau (n_e + n_h)}$

carrier concentration, B is the direct recombination coefficient, and τ is electron/hole lifetime.

Table 3.2.: The simulation parameters used in numerical simulation of HIT cell [77]

Properties	p-layer	i-layer	c-Si	i-layer	n-layer
Thickness	10mm	10mm	$200\mu m$	10mm	10mm
Doping (cm^{-3})	$N_A = 5 \times 10^{19}$	-	$N_D = 5 \times 10^{15}$	-	$N_D = 5 \times 10^{19}$
Hole mobility (cm^2/Vs)	0.2	2	330	2	2
Electron mobility (cm^2/Vs)	1	20	1030	20	10
Hole lifetime (s)	-	-	5×10^{-4}	-	-
Electron lifetime (s)	-	-	5×10^{-4}	-	-
Bandgap (eV)	1.7	1.7	1.12	1.7	1.7
Electron affinities (eV)	3.9	3.9	4.05	3.9	3.9

continued on next page

Table 3.2.: *continued*

Properties	p-layer	i-layer	c-Si	i-layer	n-layer
Conduction	N_{tail}	N_{tail}	-	N_{tail}	N_{tail}
Band Tail States	$10^{19} cm^{-3} eV^{-1}$	$10^{19} cm^{-3} eV^{-1}$		$10^{19} cm^{-3} eV^{-1}$	$10^{19} cm^{-3} eV^{-1}$
	$E_{tail} = 0.05eV$	$E_{tail} = 0.019eV$		$E_{tail} = 0.019eV$	$E_{tail} = 0.05eV$
	$C_h = 10^{-16} cm^{-2}$	$C_h = 10^{-16} cm^{-2}$		$C_h = 10^{-16} cm^{-2}$	$C_h = 10^{-16} cm^{-2}$
	$C_n = 10^{-16} cm^{-2}$	$C_n = 10^{-16} cm^{-2}$		$C_n = 10^{-16} cm^{-2}$	$C_n = 10^{-16} cm^{-2}$
Valence band tail states	N_{tail}	N_{tail}	-	N_{tail}	N_{tail}
	$10^{19} cm^{-3} eV^{-1}$	$10^{19} cm^{-3} eV^{-1}$		$10^{19} cm^{-3} eV^{-1}$	$10^{19} cm^{-3} eV^{-1}$
	$E_{tail} = 0.1eV$	$E_{tail} = 0.049eV$		$E_{tail} = 0.049eV$	$E_{tail} = 0.1eV$
	$C_h = 10^{-16} cm^{-2}$	$C_h = 10^{-16} cm^{-2}$		$C_h = 10^{-16} cm^{-2}$	$C_h = 10^{-16} cm^{-2}$
	$C_n = 10^{-16} cm^{-2}$	$C_n = 10^{-16} cm^{-2}$		$C_n = 10^{-16} cm^{-2}$	$C_n = 10^{-16} cm^{-2}$

continued on next page

Table 3.2.: *continued*

Properties	p-layer	i-layer	c-Si	i-layer	n-layer
Donor-like defects	$N_{t1} = 10^{16} cm^{-3}$ $E_{t1} - E_i = 0.31 eV$ $\sigma_{t1} = 0.08 eV$ $\tau_{p1} = 10^{-9} s$ $\tau_{n1} = 10^{-9} s$ $N_{t2} = 10^{18} cm^{-3}$ $E_{t2} - E_i = -0.26 eV$ $\sigma_{t2} = 0.15 eV$ $\tau_{p2} = 10^{-9} s$ $\tau_{n2} = 10^{-9} s$	N_{t1} $5 \times 10^{15} cm^{-3}$ $E_{t1} - E_i = 0.21 eV$ $\sigma_{t1} = 0.08 eV$ $\tau_{p1} = 2 \times 10^{-9} s$ $\tau_{n1} = 2 \times 10^{-9} s$	-	N_{t1} $5 \times 10^{15} cm^{-3}$ $E_{t1} - E_i = 0.21 eV$ $\sigma_{t1} = 0.08 eV$ $\tau_{p1} = 2 \times 10^{-9} s$ $\tau_{n1} = 2 \times 10^{-9} s$	$N_{t1} = 10^{16} cm^{-3}$ $E_{t1} - E_i = 0.31 eV$ $\sigma_{t1} = 0.08 eV$ $\tau_{p1} = 10^{-9} s$ $\tau_{n1} = 10^{-9} s$ $N_{t2} = 10^{18} cm^{-3}$ $E_{t2} - E_i = -0.26 eV$ $\sigma_{t2} = 0.15 eV$ $\tau_{p2} = 10^{-9} s$ $\tau_{n2} = 10^{-9} s$

continued on next page

Table 3.2.: *continued*

Properties	p-layer	i-layer	c-Si	i-layer	n-layer
Acceptor-like defects	$N_{t1} = 10^{16} cm^{-3}$	N_{t1}	-	N_{t1}	$N_{t1} = 10^{16} cm^{-3}$
	$E_{t1} - E_i = -0.21 eV$	$5 \times 10^{15} cm^{-3}$		$5 \times 10^{15} cm^{-3}$	$E_{t1} - E_i = -0.21 eV$
	$\sigma_{t1} = 0.08 eV$	$E_{t1} - E_i = 0.11 eV$		$E_{t1} - E_i = 0.11 eV$	$\sigma_{t1} = 0.08 eV$
	$\tau_{p1} = 10^{-9} s$	$\sigma_{t1} = 0.08 eV$		$\sigma_{t1} = 0.08 eV$	$\tau_{p1} = 10^{-9} s$
	$\tau_{n1} = 10^{-9} s$	$\tau_{p1} = 2 \times 10^{-9} s$		$\tau_{p1} = 2 \times 10^{-9} s$	$\tau_{n1} = 10^{-9} s$
		$\tau_{n1} = 2 \times 10^{-9} s$		$\tau_{n1} = 2 \times 10^{-9} s$	
Contact properties	Ohmic contacts, $s_f = 10^7 cm/s$ for both contacts				

Table 3.3.
The simulation parameters used in numerical simulation of perovskite cell

Properties	PEDOT:PSS	Perovskite	PCBM
Thickness	40nm	135nm and 350nm	20nm
Doping (cm^{-3})	$N_A = 3 \times 10^{17}$	$N_A = 1 \times 10^{16}$	$N_D = 5 \times 10^{17}$ [57]
Hole mobility (cm^2/Vs)	9×10^{-3} [58]	40	1×10^{-2}
Electron mobility (cm^2/Vs)	9×10^{-3}	40	1×10^{-2} [57]
Hole lifetime (s)	1×10^{-6}	20×10^{-9}	1×10^{-6}
Electron lifetime (s)	1×10^{-6}	20×10^{-9}	1×10^{-6}
Bandgap (eV)	1.55 [59]	1.55 [60]	2.0 [61]
Electron affinities (eV)	3.63	3.73 [62]	4.17 [63]
Contact properties	Ohmic contacts, $s_f = 10^7 cm/s$ for both contacts		

To model the tandem cell designs, first, we perform optical simulations of the full structure. Then, the carrier generation profiles so obtained are used in the transport simulator to separately characterize J-V for sub-cells. Finally, the sub-cells are connected in series using a circuit model (with negligible series resistance) to obtain the final J-V characteristics of the tandem cell.

3.3 Traditional Tandem Configuration

The electronic properties of the materials (perovskite, a-Si, and c-Si) considered in this study are chosen in such a way that we obtain the state-of-the-art efficiencies

of 24% for HIT cell and 20% for the perovskite cell. (see Table 3.2 and Table 3.3 for parameter list). The corresponding J-V characteristics are provided in Fig. 3.6a. In the following discussions, we will show how these two technologies can be arranged in tandem to achieve high performance solar cells.

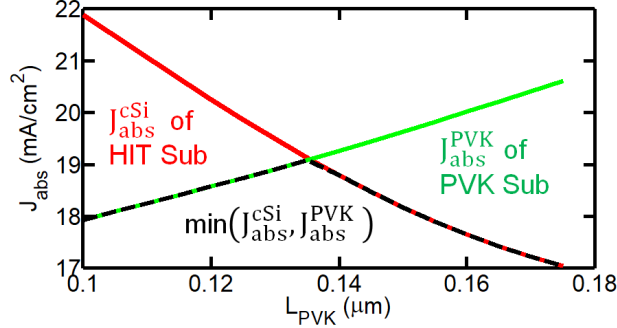


Fig. 3.5. Absorbed sunlight (in terms of corresponding current density J_{abs}) is shown for perovskite (green) and HIT (red) subcells as a function of L_{PVK} (perovskite layer thickness). The short circuit current of the series tandem will be limited to $\min(J_{abs}^{cSi}, J_{abs}^{PVK})$ as shown by the dashed black lines. We set $L_{cSi} = 200\mu m$

For a traditional tandem solar cell, a sufficiently thick top sub-cell should absorb all the photons above its bandgap, transmitting the rest of the solar spectrum to the bottom cell. The bottom sub-cell then absorbs above its bandgap from the remaining part of the spectrum. The optimum bandgap for the top cell is selected such that, the sub-cell currents are matched and output power is maximized under the above mentioned operation principles. Ideally, a top cell with $E_G \sim 1.7eV$ is required to match current produced by the c-Si bottom sub-cell, to achieve the maximum efficiency for the combination [93].

Unfortunately, in the case of the perovskite/HIT series tandem cell (see Fig. 3.1 (b)), the perovskite bandgap (1.55eV) is considerably smaller than the optimum bandgap of the top-cell ($E_G \sim 1.7eV$). [93] This makes the traditional tandem design sub-optimal, because, 300-400nm thick typical perovskite top-cell would absorb so

many photons that the bottom c-Si cell would not be able to produce sufficient J_{SC} . This mismatch in J_{SC} dramatically suppresses the power output from the tandem cell. Even for a relatively thin top-cell (e.g., $L_{PVK} \sim 170nm$, see Fig. 3.5), the currents are mismatched by $4 mA/cm^2$ (red line, J_{abs}^{cSi} ; green line, J_{abs}^{PVK}). Therefore, a delicate thickness control is essential in designing the traditional tandem cell with these mismatched sub-cells.

Fig. 3.5 shows that the sub-cell currents can be matched by varying the thickness of the perovskite (L_{PVK}) layer. The minimum absorption between the two sub-cells approximately defines the tandem J_{SC} . Therefore, we maximize $\min(J_{abs}^{PVK}, J_{abs}^{cSi})$ for achieving the highest overall current (black dashed line in Fig. 3.5). As the sensitivity of $J_{SC} \sim \min(J_{abs}^{PVK}, J_{abs}^{cSi})$ on the c-Si layer thickness is negligible, $L_{cSi} = 200\mu m$ in HIT cell is chosen for the optimized tandem cell. In contrast, the matched current is highly sensitive to L_{PVK} and even 20nm variation will lead to more than $1mA/cm^2$ lowering of short circuit current—this translates to more than 1% loss in tandem cell efficiency. The optical simulation indicates that the efficiency would be optimal at $L_{PVK} = 135nm$ (see absorption spectrum in Fig. 3.2). A more detailed thickness analysis of individual perovskite and HIT cells are shown in the Appendix A.

Once the cell thicknesses are determined from optical simulation, the analysis of carrier transport produces the full J-V characteristics (see Appendix B for energy band diagram of individual sub-cells). First, consider the individual J-V characteristics of perovskite and HIT cells shown in Fig. 3.6(a). The HIT solar cell has a higher J_{SC} but lower V_{OC} compared to the perovskite cell (as $E_G^{cSi} < E_G^{PVK}$). In a tandem structure, the sub-cell currents must be matched, as shown in Fig. 3.6(b). J_{SC} in the tandem cell ($\sim 18mA/cm^2$) after current matching is lower than both the perovskite ($\sim 24.5mA/cm^2$) and HIT ($\sim 40.5mA/cm^2$) cells. The V_{OC} in the tandem cell adds up to $\sim 1.65V$ from the sub-cells. The total efficiency is $\eta_T \sim 25\%$, which is only slightly higher than the individual cells, $\eta_{HIT} \sim 24\%$ and $\eta_{PVK} \sim 20\%$. Therefore, with careful layer optimization, it is possible to obtain modest efficiency gains through traditional tandem configurations; however, it may not be cost effective.

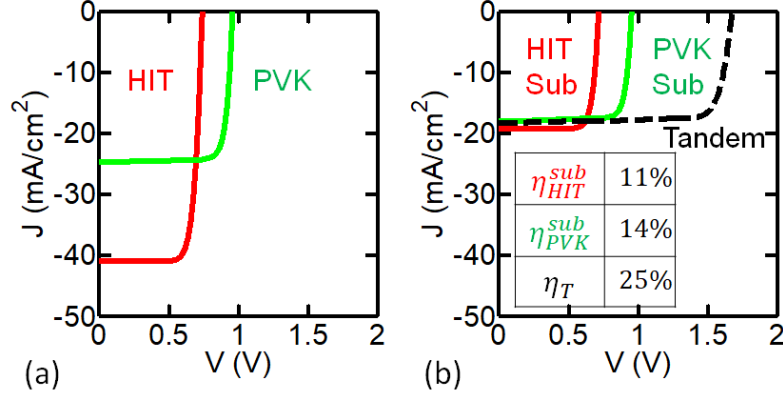


Fig. 3.6. $J - V$ characteristics of (a) individual HIT and perovskite cells (b) HIT (red) and perovskite (green) sub-cell $J - V$ characteristics are shown along with the tandem cell (black dashed line). Inset table shows sub-cells contribution to the efficiency

3.4 Bifacial Tandem Configuration

The efficiency (η_T) gain in traditional tandem configuration, unfortunately, is highly sensitive to L_{PVK} ; any deviation from the optimum (Fig. 3.5, 135nm) erodes the gain considerably. In practice, it is difficult to control L_{PVK} within 20-30nm by spin or drop-casting, causing the average gain to be much lower than the optimal. Also, in a tandem cell, the sub-cells underperform compared to their individual limits ($\eta_{PVK}^{sub} \sim 14\%$ vs. $\eta_{PVK} \sim 20\%$; $\eta_{HIT}^{sub} \sim 11\%$ vs. $\eta_{HIT} \sim 24\%$). A reduced coupling between the sub-cells is desired and the characteristic bifacial configuration of the HIT cell (see Fig. 3.1(c)) offers a simple solution, with normalized output $\eta_T^* \rightarrow 33\%$ (output power normalized to 1-sun illumination), as discussed below. The bifacial design allows light to enter the device from both top and bottom faces. In a HIT cell, the back ITO must be inserted between a-Si and metal contact to improve the optical properties and reliability [94], so that a transparent back-contact is available at no extra cost. Fig. 3.1(a) shows that the bifacial panel accepts direct solar illumination from the front and albedo reflected light from the background (grass, concrete, snow, etc.). The traditional and the bifacial perovskite-HIT tandem are identical (Fig.

3.1(b) vs. 3.1(c)), except for the back Al contact. As a result, slight increase in series resistance is expected for the bifacial design; for this study, we assume that this effect is negligible.

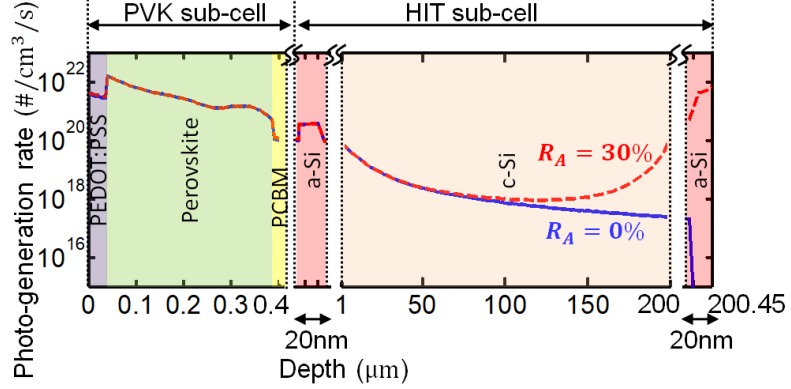


Fig. 3.7. Spatial photo-generation profile in the convention and bifacial tandem cell. The primary sunlight is from the left

The front side of the cell is exposed to direct sunlight—the high energy part of the spectrum for $> E_G^{PVK}$ ($1.55eV$) is now mostly absorbed in a 350nm perovskite sub-cell (see absorption spectrum in Fig. 3.3). The bottom HIT sub-cell absorbs few photons from the remaining spectrum, (see the blue line in Fig. 3.4). In a typical tandem, with no albedo reflectance ($R_A = 0$), η_T^* would be severely affected. However, the partially reflected light from the ground/surroundings, characterized by the albedo reflectance ($R_A < 100\%$), improves photo-generation in the HIT sub-cell considerably (red dashed line in Fig. 3.7). For the traditional tandem cell discussed earlier, η_T was limited by the constraint of matched sub-cell currents. Since the bifacial tandem cell improves J_{SC}^{HIT} , one can use a thicker perovskite to improve J_{SC}^{PVK} , free from typical constraints of the tandem cell, i.e., restriction on L_{PVK} vs. L_{cSi} . For this analysis, we choose these thicknesses to be 350nm and $200\mu m$ respectively.

We can now compare the bifacial HIT cell and the bifacial tandem for varying R_A . For low $R_A (< 20\%)$, the perovskite has higher current than the HIT sub-cell (see Fig.

3.8(a)), and the efficiency is limited by the HIT cell. As we increase scattered light entering through the bottom cell, the absorption in the HIT sub-cell will increase linearly with R_A . However, the tandem J_{SC} will be limited by the lower of the two sub-cells currents, shown by the black line in Fig. 3.8(a). Beyond $R_A > 20\%$, the tandem current is limited by the perovskite sub-cell. This also explains why the tandem cell output η_T^* increases with R_A and then saturates to $\sim 33\%$ beyond $R_A > 20\%$ (see Fig. 3.8(b)). Further, from Fig. 3.8(b) we observe that for a practical range of $R_A < 40\%$ the tandem design (black line) outperforms the typical bifacial HIT cell (blue solid line) by a considerable margin. Obviously, this bifacial design requires a slightly modified stacking of the cells.

The bottom HIT sub-cell can be grown with conventional deposition technologies [82] PCBM, perovskite, and PEDOT:PSS layers can be grown using solution process techniques—these use organic solvents and low temperatures. Thus the processing of the perovskite sub-cell is unlikely to damage the bottom sub-cell. However, the deposition of ITO using sputtering can be challenging and may damage the organic layers. Fortunately, it is possible to use other transparent electrodes such as Ag-NW nets [86], or graphene-NW co-percolating networks [95]. Some of these electrodes have been demonstrated to work on organic photovoltaics and perovskite cells [96,97]. Although the bifacial perovskite-HIT tandem seems promising, the exact structure and processing steps would require further research.

3.5 Summary and Conclusion

In this chapter, we have explored the performance potential of perovskite-HIT tandem cell based on state-of-the-art sub-cells. We find that a traditional tandem design requires an optimized perovskite thickness of $L_{PVK} \sim 135nm$ to provide a modest 25% efficient cell. Unfortunately, the efficiency gain is compromised due to sensitivity to L_{PVK} and both the cells underperform compared to their individual efficiencies. Through a bifacial tandem design one can resolve the current match-

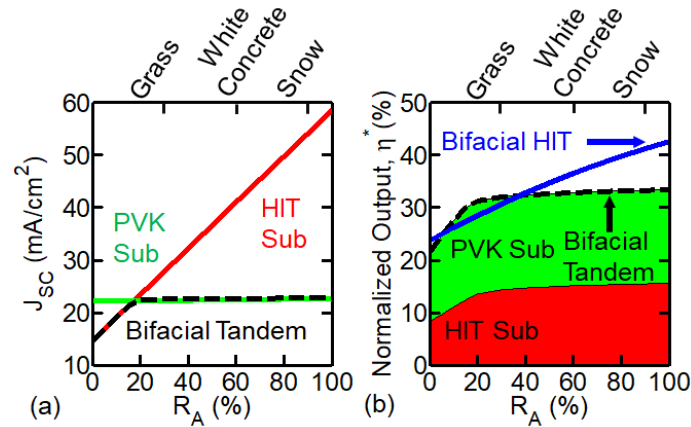


Fig. 3.8. (a) The J_{SC} of the sub-cells and bifacial tandem as function of albedo R_A . (b) Output η_T^* (normalized to 1-sun) of the perovskite and HIT sub-cells (green and red areas) are shown. The bifacial tandem (black dashed line) outperforms the bifacial HIT cell (blue solid line) for $R_A < 40\%$. Common backgrounds such as grass, white concrete, and snow have R_A of approximately 30%, 60%, and 90%, respectively [98].

ing problem and improve the performance to 33%. As an additional advantage, we observe that this efficiency gain is insensitive to thicknesses of perovskite and c-Si layers. Further, it outperforms the bifacial HIT cell over a practical range of albedo reflection. Therefore, it offers a viable, robust HIT-perovskite tandem for low-cost, highly-efficient PV technology.

Although the bifacial tandem structure offers many advantages, the stability issues of the 3D perovskite causes this configuration to be less promising. In the next chapter we study a class of 2D perovskite material called Ruddlesden-Popper that offers more stability and reliability when in contact with moisture and air with lower output power.

4. 2D PEROVSKITE SOLAR CELLS- A WAY TO IMPROVE THE RELIABILITY

Note: The material in this chapter has been adapted from Refs. [99, 100]

Bulk perovskite shows promising performance and efficiency, but the long-term stability of the fabricated devices is a concern. Multiple reliability issues, such as ion migration [101–103], absorber decomposition due to humidity [104, 105] or heat [106], degrades the performance of the perovskite cells. There have been efforts to improve the stability of the cells by encapsulating the device [107, 108], using buffer layers [109], improving the electron transport material (ETM) or hole transport material (HTM) quality [110, 111], etc., therefore, in this chapter, we will discuss the use of a new class of 2D Ruddlesden-Popper phase perovskite material [112, 113] to address the absorption layer instability issue. These 2D materials have lower efficiency due to reduced absorption compared to 3D (bulk) perovskite (see Fig. 4.1b). However, their planer structure improves charge transport inside the slabs (see Fig. 4.2a), and interlocking stacked configuration prevents phase segregation. Moreover, we explain the light, temperature and voltage dependence of the performance of the solar cells based on a 2D stacked quantum-well energy landscape.

Our LANL collaborators fabricated and characterized the device and we created the necessary theoretical foundation to interpret the reduced efficiency and improved lifetime of these devices. We realized that reduced photo absorption along with the lower mobility and higher bandgap is the main reason for lower performance compared to bulk perovskite.

Density functional theory (DFT) computations predict that $(BA)_2(MA)_{n-1}Pb_n-I_{3n+1}$ compounds have a direct bandgap, with gap energies essentially related to the number of inorganic layers. The bandgap energy (E_g) can indeed be tuned experimen-

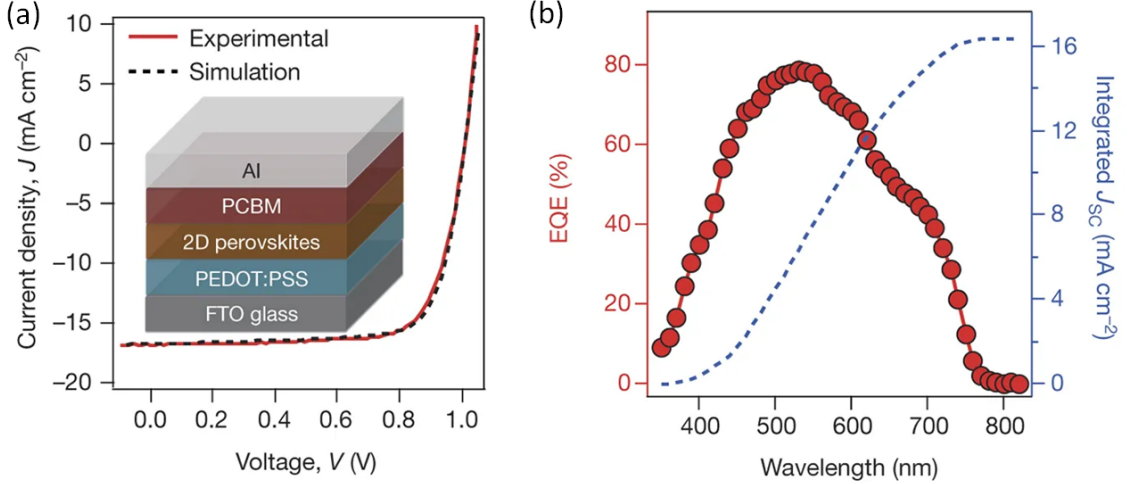


Fig. 4.1. (a) Experimental (red line) and simulated (black dashed line) current-density–voltage (J – V) curves under an AM.1.5G solar simulator for planar devices using 2D $(BA)_2(MA)_3Pb_4I_{13}$ perovskites as the absorbing layer at optimized thickness (230 nm). The inset shows the device architecture. Al, aluminum; PCBM, [6,6]-phenyl-C61-butyric acid methyl ester; PEDOT:PSS, poly(3,4-ethylenedioxythiophene) polystyrene sulfonate; FTO, fluorine-doped tin oxide. (b), External Quantum Efficiency (EQE; red circles and line) and integrated short circuit current density (J_{SC} ; blue dashed line) as a function of wavelength.

tally from $E_g = 1.52\text{eV}$ for $n \rightarrow \infty$, similar to 3D $MAPbI_3$, to $E_g = 2.43\text{eV}$ for a single atomic layer ($n = 1$), in good agreement with experimental results [108, 113, 114]. Despite lower absorption, 2D perovskite shows a high efficiency which is attributed to its high J_{SC} and fill factor. We assign this increase to the enhanced charge transport and mobility facilitated by the near-perfect vertical orientation of the $\{(MA)_{n-1}Pb_nI_{3n+1}\}^{2-}$ slabs, as demonstrated in Fig. 4.2b, relative to the FTO substrate. The excellent crystallinity (see Fig. 4.2a) and thin-film uniformity that are realized by the hot-casting technique lead to continuous charge-transport channels that enable the highly mobile photo-generated carriers to travel through the two-dimensional $\{(MA)_{n-1}Pb_nI_{3n+1}\}^{2-}$ slabs across device electrodes, without being blocked by the insulating spacer layers.

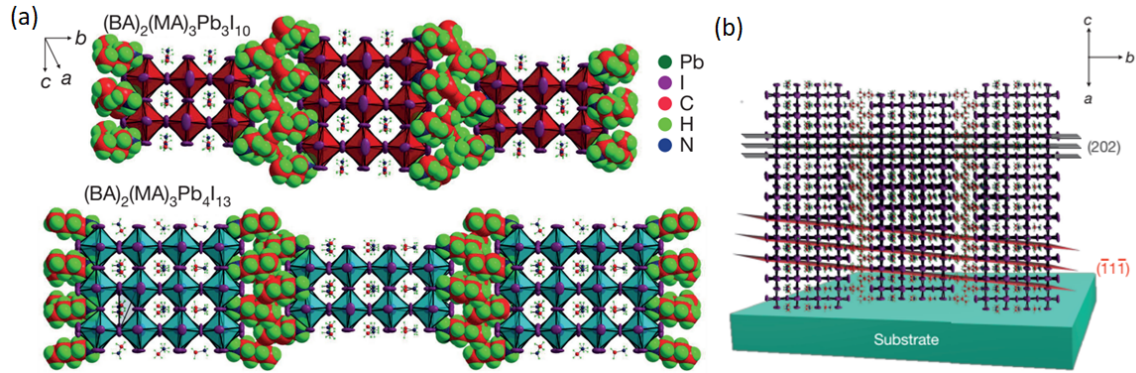


Fig. 4.2. (a) The crystal structure of the Ruddlesden–Popper $(BA)_2(MA)_3Pb_3I_{10}$ and $(BA)_2(MA)_3Pb_4I_{13}$ layered perovskites, depicted as n polyhedral blocks, where n refers to the number of layers; the BA spacer layers are depicted as space-fill models to illustrate the termination of the perovskite layers. (b), Schematic representation of the (101) orientation, along with the (111) and (202) planes of a 2D perovskite crystal

Now that we understood the molecular structure of the 2D perovskite, we explain the other effects that the structure has on the performance of the solar cells.

4.1 background

State-of-the-art quantum well based devices such as photovoltaics, photodetectors, and light emission devices were enabled by understanding the nature and the exact mechanism of electronic charge transport. Ruddlesden-Popper phase halide perovskites are two-dimensional solution-processed quantum wells and have recently emerged as highly efficient semiconductor for solar cell, approaching 14% in power conversion efficiency. However, further improvements will require an understanding of charge transport mechanisms, which are currently unknown and further complicated by the presence of strongly bound excitons. Here, we unambiguously determine that dominant photocurrent collection is through electric-field assisted electron-hole pairs separation and transport across the potential barriers. This is revealed by

in-depth device characteristics, coupled with comprehensive device modeling, which can self-consistently reproduce our experimental findings. These findings establish the fundamental guidelines for the molecular and device design for layered 2D perovskites based photovoltaics and optoelectronic devices and are relevant for other similar quantum confined systems.

Ruddlesden–Popper phase layered perovskites (RPLPs) are quantum-well structures naturally formed by n blocks of inorganic $[PbI_6]^{2-}$ octahedral slab separated by bulky organic cations. While the organic spacers act as an intrinsic protection and passivation layer against moisture, they also lead to a strong quantum and dielectric confinement, which plays an important role on the optoelectronic properties [115–118]. These confinement effects not only widen the optical bandgap relative to the 3D perovskites, but also confine electron-hole pairs to form bound excitons with binding energy greater than room temperature [119–123]. Both properties are non-ideal for photovoltaic devices which requires strong light absorption that overlaps with the solar spectrum and separation of electron-hole pairs for photocurrent collection. Until recently, its use as light absorbers for solar cells has been motivated by the breakthrough in synthesis of layered 2D perovskites with higher n values ($n > 3$) [113, 114, 124, 125] with broader light absorption across the solar spectrum [112, 126–129]. This coupled with our capability to grow highly crystalline Ruddlesden–Popper layered perovskite thin-films with preferential out-of-plane orientation [128], have enabled photovoltaic cells with power conversion efficiency approaching 14% in a simple planar configuration [127]. Moreover, our recent work also elucidated a unique internal charge separation of the optically generated excitons via a lower energy states in layered 2D perovskites with $n > 2$ [130]. However, despite these promising breakthroughs along with the demonstration of technologically relevant environmental and photo-stability, it has been challenging to achieve power conversion efficiencies on par with the 3D perovskites. To realize the tremendous potential of layered 2D perovskites for photovoltaics and other efficient optoelectronic devices, it is critical to understand the

fundamental charge transport mechanisms that limit the efficient charge transport in these systems.

In this part, through extensive device characterization and modeling, we elucidate the dominant charge transport mechanism during solar cell operation and identify the key bottlenecks that limit the overall efficiency in layered 2D perovskites. The thickness dependent device characteristics reveal that, while the absorption can be enhanced with thicker layer, the overall performance is then limited by transport. Therefore, planar $p-i-n$ junction cell efficiency reaches a peak value with 200nm absorber thickness where photo-generated carriers separation and transport are highly efficient assisted by the strong internal electrical field. However, in sharp contrast to 3D perovskites, the recombination for 2D perovskite device gets higher as the light absorber thickness increases. Light intensity dependent measurements suggest that photo-generated carriers can be efficiently collected at short circuit condition while the performance is undermined by radiative recombination in the low field regime. In addition, we show that the electronic transport is thermally activated suggesting that charge carriers need to surmount potential barriers before they are collected at the contacts. To interpret all the observations, we propose a model based on stacked quantum wells where charge collection occur through transporting across multiple potential barriers, similar to classical semiconducting quantum well systems [131]. The potential barriers are thought to arise from the presence of imperfect stacking of the inorganic slabs in thin films, which may introduce organic spacers, which intermittently disrupt the conducting pathway leading to field dependent charge collection. As the thickness of the film increases, the density of barriers arising from misalignment also increases. Our model self-consistently reproduces our experimentally observed device behavior, thus validating that the key bottleneck limiting the photocurrent collection is indeed field-dependent charge separation through the barriers. Our results provide the fundamental guidelines for the design of layered 2D perovskites for high efficiency photovoltaic devices, which will require improving the light absorption, engineer highly doped contacts to facilitate efficient charge separation and collection for

thicker films or investigate incorporation of conducting (organic or inorganic) spacer molecules to reduce the potential barriers.

4.2 Experimental Results

This section focuses on the solar cell characteristics in planer $p-i-n$ device configuration employing layered 2D $BA_2MA_3Pb_4I_{13}$ material (Pb_4 unless otherwise mentioned) as the light absorbing layer (Fig. 4.3) sandwiched between p-type (poly(3,4-ethylenedioxythiophene-polystyrenesulfonate, PEDOT: PSS) and n-type ([6,6]-phenyl- C_{61} -butyric acid methyl ester, PCBM) contact layers (See Fig. 4.3a for layered 2D perovskite structure and device architecture).

4.2.1 Thickness Dependence of the Performance

To understand the solar cell operation principles, we first vary the absorbing layer thickness and characterize the solar cell performance (see Fig.4.3). Fig. 4.3c shows the current density-voltage (J-V) curve of the planer cell with various absorber layer thicknesses (from 100-620 nm) under Air mass 1.5 global (AM 1.5G) solar simulator illumination with 1-Sun equivalent light intensity ($100mW/cm^2$). Along with the J-V curve, external quantum efficiencies (EQE) for those devices are illustrated in Fig. 4.3d. The EQE curves indicate an absorption onset value of 1.63 eV (760nm), that is consistent with the bandgap expected for the 2D Pb_4 perovskite thin film [113,132]. From the J-V and EQE, we observe a strong dependence of the photovoltaic performance on the layered perovskite film thicknesses, strongly reflected in the magnitude and shape of the short circuit current density curves, and consequently the amplitude of EQE spectrum.

We analyze the results by extracting the power conversion efficiency (PCE), short circuit current density (J_{SC}) and open circuit voltage (V_{OC}) from the light J-V curves, and plot them as a function of film thicknesses as illustrated in Fig. 4.3e-g. As a comparison, the thickness dependent J_{SC} for 3D methyl ammonium lead triiodide

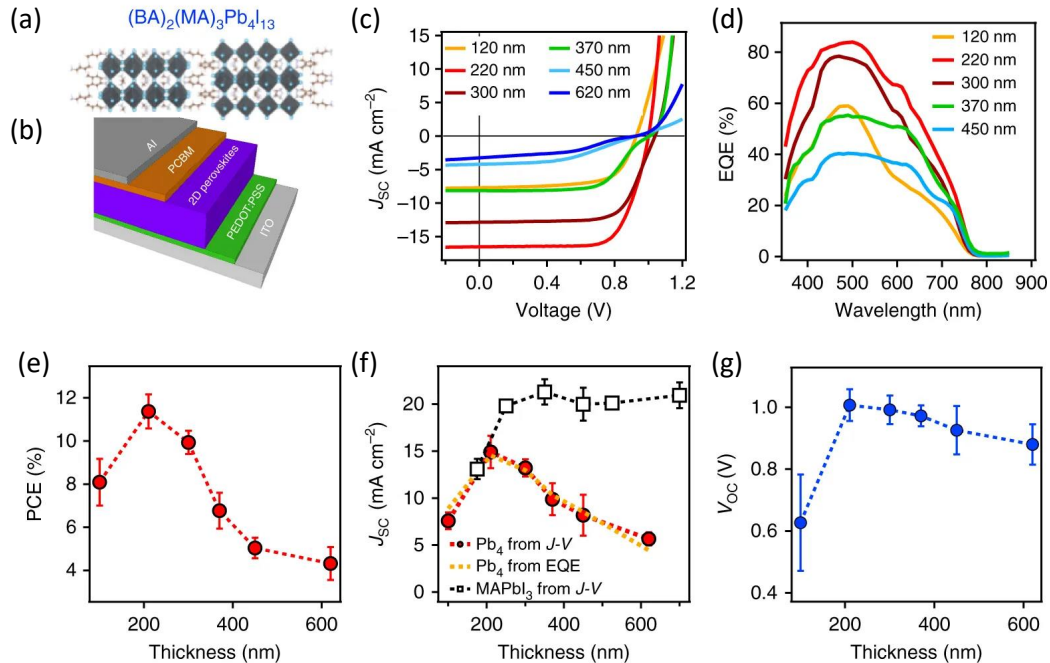


Fig. 4.3. Photovoltaics with various absorber thickness evaluated by J–V characteristics. (a) Molecular structure of $BA_2MA_3Pb_4I_{13}(Pb_4)$ and (b) planar solar cell device structure used in this study. (c) J–V curve under AM 1.5G solar-simulated light with 1-Sun equivalent power and (d) EQE spectrum collected under short-circuit condition with monochromatic light for planar device with various Pb_4 film thicknesses. (e–g) Extracted average PCE, J_{SC} and V_{OC} as a function of film thickness. The J_{SC} for a device with methyl ammonium lead triiodide ($MAPbI_3$) as an absorber in the same structure is measured as a comparison in f (black curve). Error bars in (e, f) were s.e.m. collected over eight devices of various absorber thickness for statistics

($MAPbI_3$) absorber in the same device structure is also plotted in Fig. 1e. The overall PCE of the layered perovskite cell plotted in Fig. 1d increases sharply as the film thickness increases from 120 nm ($PCE \sim 7 \pm 1.21\%$) and reaches a maximum value for a thickness of 220 nm ($PCE \sim 11.37 \pm 0.97\%$). This is mainly due to the enhancement in the absorption with increasing film thickness as confirmed by the EQE spectra in Fig. 4.3d. However, beyond a film thickness of 220 nm, we observe a significant drop in the PCE down to $6.89 \pm 1.17\%$ for 450 nm film thickness. Analysis

of the J_{SC} as a function of thickness curve (Fig. 4.3e) exhibits a peak value for a thickness value of 220 nm followed by a monotonic decrease for the thicker films. Such dependence is consistent with the integrated J_{SC} value from the EQE spectrum (Fig. 4.3d) taken under short circuit condition, validating the J-V measurement. Comparison of the thickness dependence of the J_{SC} from the 2D and 3D perovskite device in Fig. 4.3f shows that the J_{SC} for 3D perovskite devices (black curve) are insensitive to the film thickness between 250 nm and 600 nm range.

From the thickness dependent results, we conclude that charge collection is the most efficient for the optimized film thickness, which leads to high fill factor (FF) value ($74.1\% \pm 2.2\%$) and J_{SC} ($14.92\text{mA}/\text{cm}^2 \pm 1.73\text{mA}/\text{cm}^2$). High V_{OC} value ($\sim 1.0\text{V} \pm 0.05\text{V}$) is an indication of low non-radiative recombination at open circuit. This excellent efficiency in a simple planar device architecture is unusual considering the fact that photo-generated carriers in these 2D perovskite systems are excitonic in nature [119–121]. However, once the thickness is above 200 nm, photo-generated carrier decay to ground states before being collected at the contact, leading to inefficient collection that reduces the J_{SC} , FF, and thus the PCE. This is consistent also with the trend observed for V_{OC} as a function of thickness in Fig. 4.3g, which decreases as the film thickness increases. In contrast, the J_{SC} for 3D perovskite cell is less sensitive to the film thickness in 300 ~ 500 nm range, because optical excitation produces free carriers [35, 133, 134] can be efficiently collected at the contacts, even for thicker layers as the cell operates in the non-Langevin type of recombination regime.

The increased absorber thickness leads to two changes in the system; first the distance between two electrodes is enlarged (while orientation remains similar) and second, the net field that drops across the film is reduced (see Fig. 4.4 for simulated field profile for higher absorber thicknesses). At SC, the charge collection relies on electron-hole pair separation followed by transport drifting by the internal field. In contrast, at OC the net field is low and the collection relies on carrier diffusion, and any potential barriers (insulator or trap states) will significantly reduce the collection efficiency. In our case specifically, the photocurrent collection for layered perovskite

solar cells with a thickness of 220 nm is highly efficient resulting in a high fill factor. Beyond 300 nm, the carrier diffusion at OC is greatly limited by the large distance and small field between HTM and ETM selective contacts, which increases the probability of carrier recombination losses. This is because layered perovskite is an intrinsic semiconductor with low doping density [128] and the depletion region width in a planar device configuration is 200 ~ 300 nm, beyond which flattening of electrical field profile occurs. This thickness is thus the upper limit for the field drop across the device as determined by device simulations (Fig. 4.4). Therefore, the photo-generated carrier collection especially at the center of the film for the layered perovskite system is strongly field dependent leading to a reduction in the J-V slope near OC, while the SC slope remains flat. For film thickness exceeding 500 nm, both drift and diffusion are inefficient, which essentially lowers the photo-current collection in both conditions.

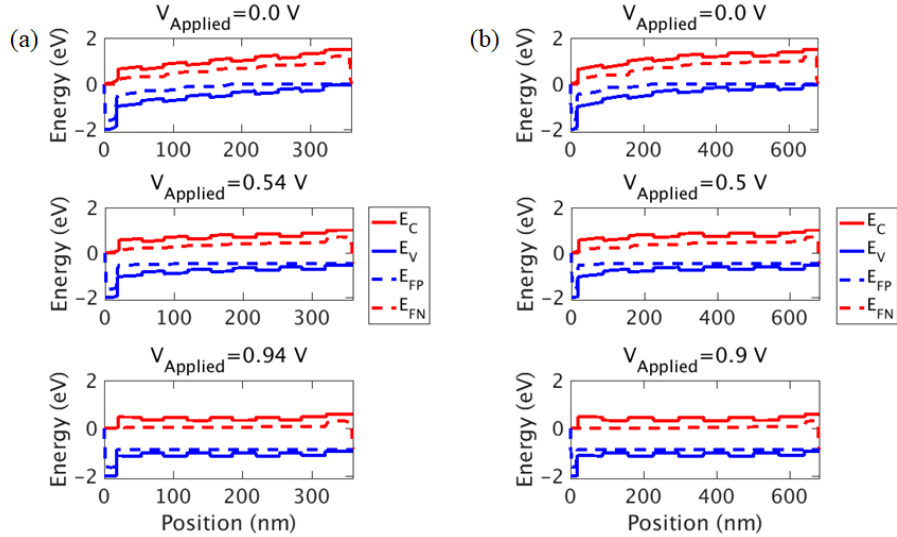


Fig. 4.4. the energy band diagram for (a) 300nm and (b) 620nm perovskite thickness at three different external bias conditions.

As a summary, the final performance of layered perovskite solar cell is a competing process between photo-generation (absorption) and carrier transport through the layer thickness. A simple increase in film thickness would improve the absorption but

in the mean-time reduce the carrier transport, which does not lead to an increase in the overall efficiency.

4.2.2 Light Intensity Dependence

To understand the exact loss mechanism at SC and OC, we performed light intensity dependent J-V characteristics for the layered perovskite device with two thicknesses and are described in Fig. 4.5. These experiments allow to probe the absorption and transport trade-off for charge collection through an energy landscape dominated by quantum wells independently. Fig. 4.5a-b shows the normalized J with J_{SC} as a function of effective internal field ($V - V_{OC}$) under various light intensities from 10 mW/cm^2 to 500 mW/cm^2 for the thickness of 220 nm and 375 nm devices respectively. The extracted J_{SC} and V_{OC} as a function of light power are plotted in Fig. 4.5c-d. In Fig. 4.5a-b, we found that the slopes near SC for both thicknesses do not vary. The J_{SC} values as a function of light intensity follow an almost linear dependence in the power range of 1-500 mW/cm^2 as shown in Fig. 4.5c. Both these data suggest that the charge collection efficiency or charge recombination loss is independent of incident light intensity (carrier density) at SC [64, 135]. In both cases, the radiative recombination process, which is highly carrier density dependent, does not contribute to the photocurrent loss at SC, where all the free carrier can be collected due to the presence of a strong internal electric field [135–137]. The majority loss should be through the monomolecular process from either Coulombically bound electron-hole pair recombination or a trap assisted process [64, 137, 138]. In contrast, the slope near low field (from MPP to OC) changes the most dramatically for higher light intensities. This is attributed to the enhanced radiative recombination at low fields and higher carrier densities [135–137, 139]. For a 375 nm thick film the change in slope occurs at a lower threshold than that in 220 nm film with varying light intensity (Fig. 4.5b). This is because of both the enlarged absorption and the higher

probability of radiative recombination in thicker films as carriers must diffuse through a larger distance to be collected.

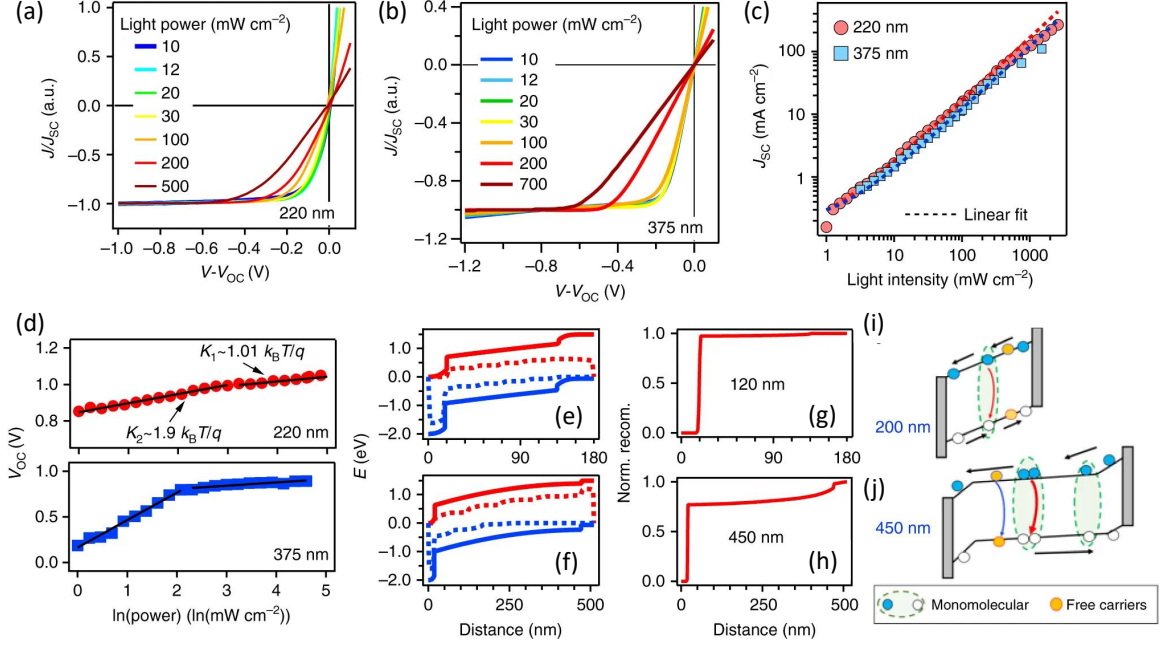


Fig. 4.5. Light intensity dependence with device J–V characteristics. Normalized light J–V curves for a device with absorber thicknesses of (a) 220 nm and (b) 375 nm under various illumination intensities. (c) J_{SC} value as a function of light power over a wide illumination range. (d) V_{OC} as a function of illumination intensities for two device thicknesses. (e, f) Calculated band energy as a function of film thickness and (g, h) normalized recombination profile as a function of distance in the device for two typical thicknesses. (i, j) Schematics illustrating the carrier recombination processes in thin film and thick film in the quantum well-layered perovskite structure.

Next, we plot V_{OC} against the natural log of light power in Fig. 4.5d to investigate the carrier recombination losses near OC. The data reveals that the V_{OC} follows two linear regimes, one at high power with a slope of $\sim 1k_B T/q$ and the other near low light with a slope of $\sim 2k_B T/q$ (where K_B is Boltzmann constant, T refers to temperature and q is the elementary charge) [138]. The thicker film again shows a much lower threshold for the change in the slope of V_{OC} . The linear dependence is indicative

of the recombination process near OC. It first follows a monomolecular process at lower light intensities but then switches to a radiative recombination process. This suggests that at lower light powers, the quasi-fermi level splitting is reduced with carrier density and consequently decreases the built-in field. [138, 140–142].

The recombination analysis is further supported by band diagram calculated from device simulation in the layered perovskite device and the recombination profile based on the charge density distribution, as shown in Fig. 4.5e-f. The band diagram clearly shows that the internal electrical field drop at short circuit condition through a thin device is uniformly strong throughout the film; while that for a thicker layer is reduced especially at the center of the film, featuring with a flatten region. Such field drop at thicker layer will promote recombination and therefore, the recombination profile as a function of distance differ dramatically in the two cases (Fig. 4.5g-h). In the thin layer, the recombination majorly occurs near the interface because the film is fully depleted by the internal field. However, when film grows thicker, the recombination occurs both at bulk and near the interface due to the weakened field near the center.

To corroborate the above discussion, we draw a schematic illustration that describes the different recombination processes during the planar cell operation in Fig. 4.5i-j. For thin layers (in $200 \sim 350\text{nm}$ range) when the field is strong across the device, the bound carriers can be separated into free carriers (Fig. 4.5i), which are subsequently collected by the strong internal field at SC. The major loss mechanism is diffusion limited free carrier recombination at low field (near OC), and larger thicknesses will lead to more free carrier recombination loss. However, the free carriers can be collected near SC quite efficiently as evidenced by the linear relationship of J_{SC} versus power curve within this thickness range, and the reduction in J_{SC} from 200 nm to 375 nm is thus attributed to monomolecular loss. When the film thickness increases to ~ 450 nm (Fig. 4.5j), the internal field drop is greatly reduced especially near the center of the film. The photo-generated carriers can only undergo a partial separation, and non-separated carriers generated in the center of the film recombine strongly through the monomolecular process, that results in strong field dependence

near SC as well as OC. Such picture agrees with the recombination analysis based on the V_{OC} as a function of light intensity curves for both of the thicknesses in Fig. 4.5d and the recombination profile in Fig. 4.5g-h.

4.2.3 Temperature Dependence

To differentiate possible origins leading to the monomolecular recombination, we conducted device J-V characteristics under low temperatures that are presented in Fig. 4.6. The J-V curves plotted in Fig. 4.6a are normalized by J_{SC} values to compare the field dependent behavior from SC to MPP. As temperature reduces, the slope near SC is greatly enhanced, this suggests an emergence of field dependence in the photocurrent collection [123, 135]. The J_{SC} and V_{OC} values as a function of temperature extracted from the J-V curves are also plotted in Fig. 4.6b-c. When the temperature decreased from 300 K to 200 K, the device loses J_{SC} and FF monotonically as expected for inefficient charge collection (see Fig. 4.6c-d). The V_{OC} first increases as the temperature is lowered to 260 K, which is consistent with lowered dark injection (recombination) current at low temperature [135, 143]. Further, the V_{OC} tends to saturate as the temperature is further lowered to ~ 200 K, most likely due to the competition between the suppressed thermal recombination and enhanced radiative recombination, which otherwise should continue to increase linearly with T. To quantify the collection efficiency with temperature near SC, we plot the slope of J-V curve as a function of T in Fig. 4.6d. The slope decreases exponentially with temperature, which is expected from a classical temperature dependence described using a thermally activated model. The inverse slope $\ln(d(J/J_{SC})/dV) - 1$ against $1/T$ is plotted in Fig. 4.6e following Arrhenius equation to obtain an activation energy (E_a). From the linear fit, the E_a is estimated to be ~ 130 meV (in the temperature range of 300 K to 200 K).

The emergence of J-V slope near SC and OC both indicate the presence of energy barriers for photocurrent collection, intrinsically existing in the thin device, and is

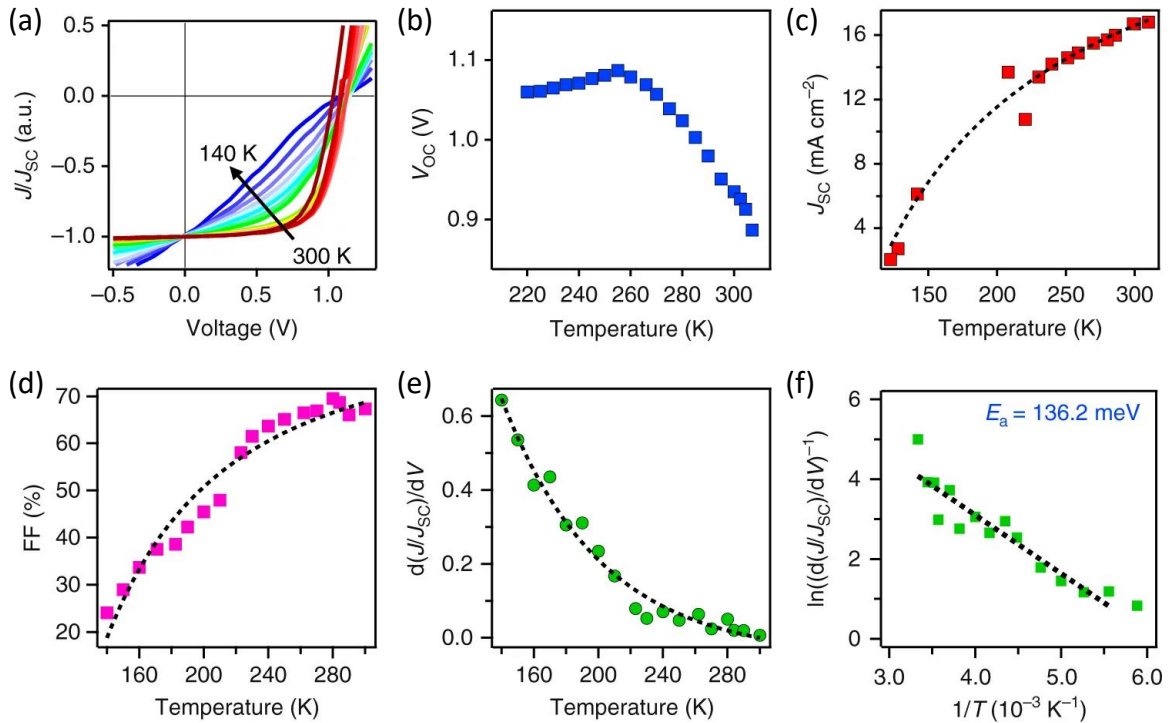


Fig. 4.6. Device characterization under low temperatures. (a), normalized light J-V curves under 1-Sun illumination for device with absorber thickness of 220 nm. (b), J_{SC} , (c), V_{OC} and (d), fill factor (FF) as a function of temperature, dashed line is guidance to the eye. (e), extracted J-V slope at SC at various temperatures with dashed line as fitting curve and (f), the linear plot following Arrhenius equation by plotting the inverse J-V slope in natural log scale against $1/T$, dashed line is linear fit.

more pronounced at a lower temperature. As the temperature gets lower, the carriers lose their thermal energy, thus making it harder for carriers to surmount the barrier although the barrier height remains unchanged. This results in the loss of charge carriers in the process of hopping across the potential barriers, which decreases the overall photocurrent.

4.3 Simulation Results

Finally, to consistently interpret all the experimental observed data from three independent measurements, we propose a model specially designed for the 2D perovskite system where vertically stacked quantum well are present throughout the film thickness. Based on that, we conduct theoretical device modeling to interpret all the data consistently as demonstrated in Figure 4.7. Fig. 4.7a schematically illustrates the energy-band landscaped, reflecting the fact that in a layered 2D perovskite quantum wells system. Unlike the conventional quantum wells where wide bandgap materials are stacked in a layer by layer fashion out of plane, in our case those quantum wells are stacked vertically as demonstrated by our previous work [116]. Even though the thin films were growth with preferred vertical out-of-plane direction, the slight mismatch and imperfect crystal packing in thin-films (in comparison to single crystals) manifests as potential barriers created by the partially intercepting organic spacers between conducting inorganic slabs that could interrupt the transport pathway (Fig. 4.7i). This band diagram thus identifies two types of carriers: quasi-bound carriers localized in low energy levels in inorganic regions and free delocalized carriers outside the potential barriers. The electrons and holes are repeatedly trapped into and de-trapped from the quasi-bound states as they are moving towards their respective contacts.

Based on this model, the experimental J-V characteristics trends can be mostly reproduced by simulation as shown in Fig. 4.7b-f, the calculated band diagram with multiple potential barriers is shown in Fig. 4.4 in SI. For example, Fig. 4.7b-c explain the thickness-dependent turn-around of the photocurrent shown in Fig. 4.3b and 4.3e. For very thin absorbers ($< 200nm$), the photo-absorption is incomplete, therefore even though the high internal field ($E \propto V_{bi}/W$) assists in the collection of most of the photo-generated carriers resulting in high internal quantum efficiency are comparable to best performing device, the short circuit current is still low. Here, V_{bi} is the built-in voltage and W is the absorber thickness of the solar cell. For thicker

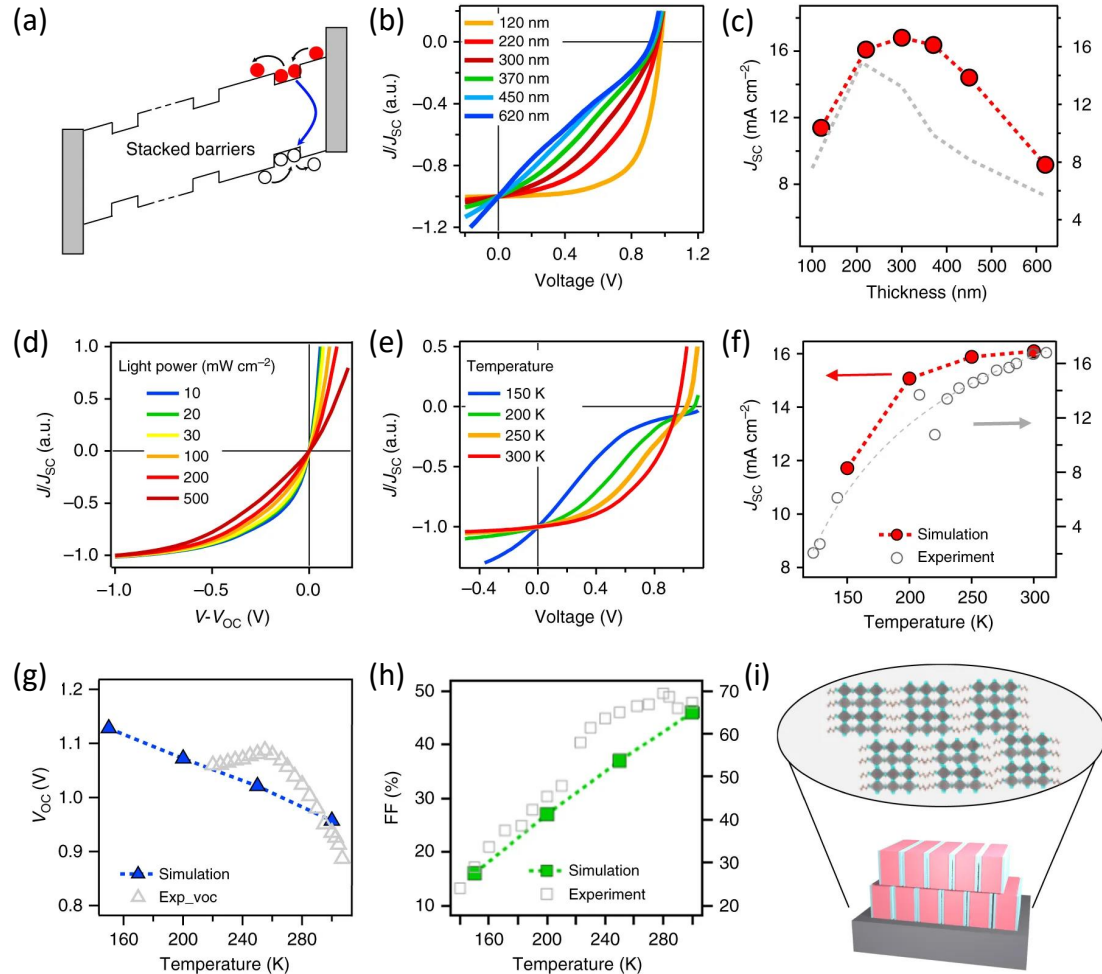


Fig. 4.7. Model and simulation results. (a), the model shows potential wells that can prevent carriers from escaping. (b) and (c), the thickness dependence of J-V curves and J_{SC} . Very thick structures increase the recombination in wells and reduce J_{SC} . (d), intensity dependence of normalized J-V curves. (e-h), Temperature dependence of J-V curves and the extracted J_{SC} , V_{OC} and FF as a function of temperature. The simulated normalized J-V curves are shifted by 5% of J_{SC} at $T=200$ K to account for temperature dependent carrier generation. The experimental data taken from Fig. 4.3 and Fig. 4.6 in grey symbols are plotted along with the simulated data to directly compare the two.

absorber ($> 200nm$), the absorption is essentially complete, but the internal field is now too weak to extract the free carriers through the energy-landscaped dominated

transport through trapping and de-trapping repeatedly. Consistent with Fig. 4.3, the photocurrent is maximized at $W \sim 200nm$ when the photo-absorption is balanced by photo-generation and charge transport. In addition, the J-V characteristics in Fig. 4.7b also shows that the evolution of differential conductance (as a function of W) is an intrinsic feature of charge collection through such a complex energy landscape and is unrelated to series and shunt resistances of typical solar cells.

Regarding the temperature dependence of the V_{OC} as shown in Fig. 4.8 the simulated results follow the same trend as experiments. Although the absolute values do not match and V_{OC} shows a turnover that has been seen in the heterojunction systems before [144]. In the simple model, however, we did not account for temperature-dependent mobility, nor the temperature dependent increase in the bandgap of 2D perovskite. Hence, we refined two aspects of our simulation set; 1) Bandgap increase with temperature is incorporated based on experimental data from [130], and 2) a Gaussian-disorder mobility model [145] of the form $\mu = \mu_{\infty} \exp\left(-\left(c\frac{\sigma}{kT}\right)^2\right)$ has been incorporated for transport within the barrier and the quantum well regions. Here, μ_{∞} is asymptotic high-temperature mobility limit, σ Gaussian-disorder width, and previous work in related material has found $c \sim 2/3$ [146]. With this modification included, the V_{OC} vs. T characteristics is reproduced, as shown in Fig. 4.8a. With $\sigma = 50 meV$, we find $\mu_{\infty} = 53.9$, $c = 0.669$, see Fig. 4.8b.

Similarly, the same model is employed to predict the light intensity and temperature dependent plots as summarized in Fig. 4.7d and 4.7e. The result provides consistent validation of the experimental data reported in Fig. 4.5 and Fig. 4.6, respectively. The linear increase in J_{SC} with intensity shown in Fig. 4.5c is intuitively obvious. More interesting, Fig. 4.7d explains the non-intuitive reduction in FF (as seen in Fig. 4.5b) as a consequence of increased recombination of quasi-bound carriers at a higher intensity. Finally, Fig. 4.7e-f explains the reduction of J_{SC} and FF with temperature. Lowering the temperature decreases the thermal energy of the carriers trapped within the energy wells: the carrier cannot escape as easily, and thus the recombination is greatly enhanced. Beyond the 280-300 °C, the carriers have suffi-

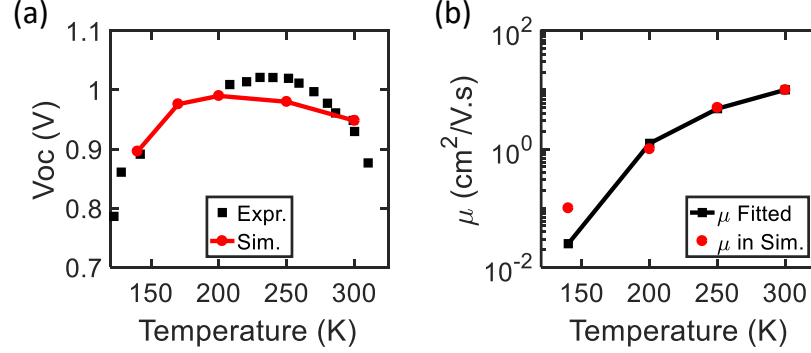


Fig. 4.8. (a) Experimental and simulated V_{OC} as a function of temperature. (b) The mobility values used in the drift-diffusion simulator were fitted by the Gaussian-disorder mobility model to find μ_{∞} and c .

cient energy to surmount the energy barrier, and thus J_{SC} begins to saturate beyond the temperature. On the other hand, the FF of the device drops drastically with temperature (Fig. 4.7h), indicating a thermally activated charge collection in the system. Consistent with the activation energy of photocurrent collection following Arrhenius relationship of J-V slope against $1/T$ in Fig. 4.6e, the barriers between the regions differ by 150-200 mV from device simulation. We acknowledge that the relative bandgap value may change with temperature, which can alter the absolute magnitude of solar cell figure-of-merits. However, the trend for carrier transport under low temperature does not change. This is supported by the trend by comparing the experimental data to simulated curves on J_{SC} and FF (Fig. 4.7f-h), because the relative barrier height remains invariant (Fig. 4.9-4.10), which is the dominant factor that influences the carrier transport.

Based on the above results and discussions, we establish that the key bottleneck in the layered perovskite quantum well photovoltaic devices is the field limited carrier collection. Such limitation arises from the presence of multiple potential wells, which requires a strong built-in electric field for thicker 2D perovskite films. Independent of whether the photo-generated carrier is an exciton or free carrier, a strong electric field is necessary for the carriers to surmount the potential barrier before they recombine.

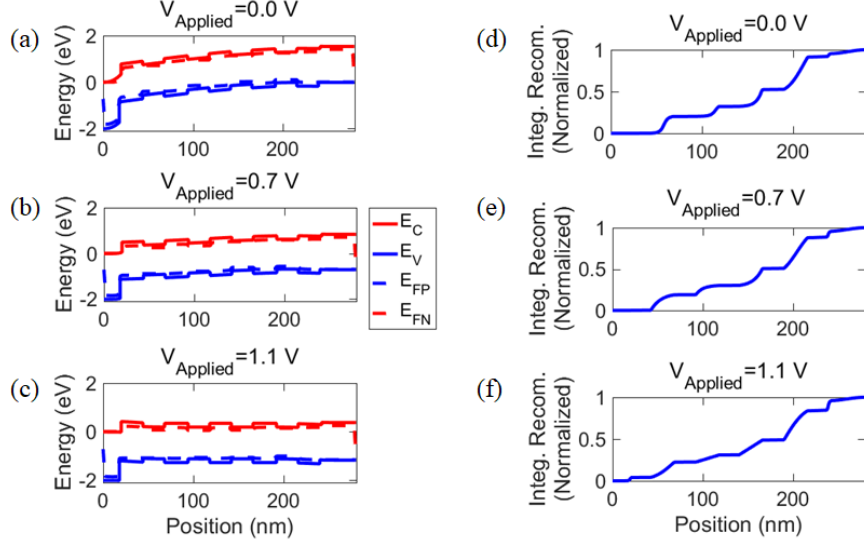


Fig. 4.9. Energy band diagram and normalized total recombination at $T=150 \text{ K}$. At (a,d) short circuit (b,e) maximum power point and (c,f) open circuit. More than 92% of total recombination happens inside the quantum wells. Low temperature does not provide enough thermal energy for carriers to leave the wells efficiently.

In our analysis, the magnitude of the potential barrier incorporates any effects associated with the exciton binding energy. Because such a phenomenological approach is validated by the fact that the model can self-consistently explain three independent experimental data (i.e. intensity, field dependence, and temperature dependence), we can propose the mechanism without explicitly invoking the exact nature of carriers.

4.4 Conclusions

In summary, based on our results, we have identified the key bottleneck for the charge transport for vertically stacked layered perovskite quantum well photovoltaic devices arises from recombination losses of charge carriers across potential barriers created. These findings present opportunities for the design of 2D perovskite structures, where long-range vertical packing for facilitating conducting pathways can be

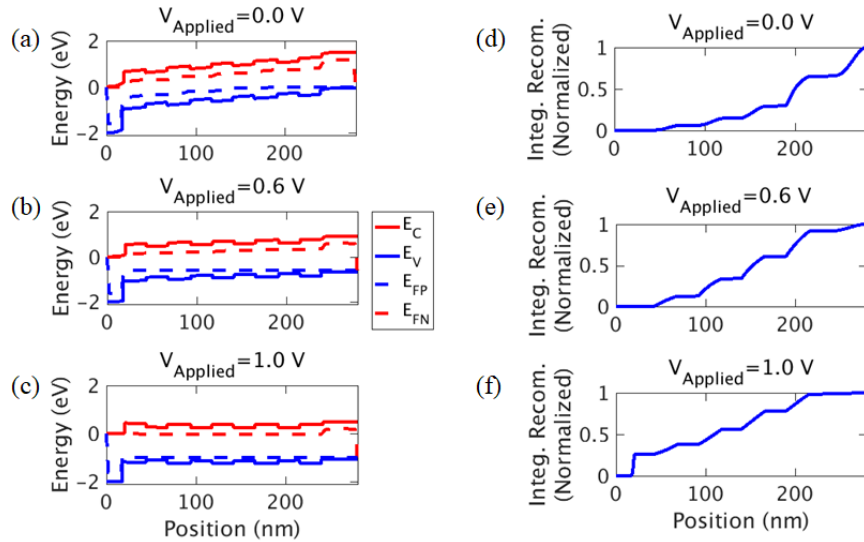


Fig. 4.10. Energy band diagram and normalized total recombination at $T=300$ K. At (a,d) short circuit (b,e) maximum power point and (c,f) open circuit. Less than 75% of total recombination occurs inside the quantum wells since thermal energy helps the carriers to escape the wells.

achieved that result in reduced numbers of potential barriers. Alternatively, doping the organic spacers to reduce the dielectric contrast, which could result in lowering the potential barriers for efficient charge transport. We anticipate that our work will lead the next steps for the incorporation of such strategies, which could overcome this fundamental bottleneck for transport in 2D perovskites and lead to high-efficiency photovoltaics and other optoelectronic devices.

Now that we have described the mechanism behind the transport and higher stability of the 2D perovskite, we will focus on investigating the reliability issues of the c-Si solar cell/panels. The next three chapters discuss the contact delamination, corrosion, and solder bond failure as second major reliability issues of c-Si solar panels.

5. RELIABILITY OF C-SI SOLAR MODULES

Note: The material in this chapter has been adapted from Ref. [147]

The levelized cost of electricity (LCOE) of solar energy can be reduced by lowering the manufacturing cost, increasing the efficiency of the cells, and enhancing the reliability of the modules. Thus, the ability to predict the lifetime and improve the reliability of modules plays a pivotal role in commercial PV systems. Among various reliability issues (e.g., yellowing, PID, partial shading, etc.), Jordan et al. identified Internal Circuitry (IC) discoloration caused by corrosion as the second most significant degradation mode in the systems installed in the last 10 years [148]. Indeed, Corrosion, Delamination, and Solder bond failure (CDS) have always played a critical role in defining module lifetime [149, 150]. PV degradation can be monitored and predicted in one of the two ways: pre-installation accelerated qualification tests and post-installation off-line field tests. In accelerated qualification tests, well-controlled environmental stressors (e.g., humidity, temperature) attempt to isolate/accelerate the specific degradation pathway (e.g., UV test for yellowing) [151–158]. In practice, a given combination of stress conditions may, in fact, accelerate more than one degradation modes. Misattribution of multiple degradation modes to a single presumed degradation mechanism makes predictive modeling difficult. Specifically, correlated degradation makes interpretation of I-V characteristics challenging. For example, depending on the stress condition used, a degradation mode (e.g. corrosion) may appear as a decreased shunt-resistance ($R_{sh} \sim (\frac{dJ}{dV})_{V=0}^{-1}$), loss of short-circuit current ($J_{SC} \equiv J(V = 0)$), and/or increase in series resistance ($R_s \sim (\frac{dJ}{dV})_{V=V_{oc}}^{-1}$), as have been reported in many experiments [151, 153, 158]. Any approach that considers R_s -increase as the sole signature of corrosion will miss important signs of early degradation related to finger corrosion, for example. The situation is even more

complicated for off-line testing of fielded modules. Here the environmental stress factors are uncontrolled, and therefore multiple degradation modes occur simultaneously. The concurrent degradation mechanisms make it difficult to isolate degradation modes [148, 150] based on I-V analysis by a traditional five-parameter model. In this chapter, we will establish a new physics-based approach to interpret I-V signatures for degradations involving CDS. These I-V signatures will simplify the interpretation of accelerated tests as well as off-line field data. We wish to emphasize that significant amount of physical modeling and material characterization work have already been done to establish the kinetics of moisture diffusion, the physics of Na ion transport, and the reaction products formed near the contact during CDS degradation [159, 160]. However, the implications of these degradations in terms of module I-V characteristics are not clear. Therefore, in this chapter, we wish to explore the physics of CDS and how they influence the electrical performance of the cells and modules. Then we will recommend a set of rules to differentiate these mechanisms and their features from other degradation modes. In Sec. II, we explain the simulation framework to study CDS failure effects. In Sec. III, we explain the corrosion geometry, solder bond failure, and their effects on I-V curves of the affected cell. Then we use the cell results to simulate I-V of modules to demonstrate the effects in module level in Sec. IV. We discuss the results in Sec. V and conclude in Sec. VI.

5.1 Theory and Modeling Framework

Solar cell consists of a substrate that absorbs sunlight and generates electron-hole pairs. Photo-generated carriers are transported away from the cell by metal contacts. In a c-Si cell, the front metal contacts are arranged in a hierarchical grid pattern to balance shading of the incident light vs. power lost to “series” resistance during charge collection. Typically, the H-shaped grid consists of (≈ 60 to $100\mu m$) thin fingers (red horizontal lines, Fig. 5.1a) carrying the current from semiconductor towards a wider ($\approx 1mm$) busbar (thick vertical blue lines, Fig. 5.1a). The busbars themselves are

contacted with ribbons (thinner vertical yellow lines, Fig. 5.1a) via tabbing points (white circles) to carry the current from one cell to the next in a module.

Corrosion can affect the metal grid in a variety of ways. For simplicity, we will discuss three specific types of grid corrosion. More complex corrosion pattern can be viewed as a superposition of these “elementary” processes. First, grid finger thinning shown in Fig. 5.1b causes the current to travel through a finger with a reduced cross-section (i.e. higher resistance). Second, grid delamination shown in Fig. 5.1 c prevents current pick-up by the finger so that the carriers must travel further through the semiconductor laterally to reach the un-delaminated section of the metal line. Third, busbar solder bond failure shown in Fig. 5.1d eliminates the tabbing points and current must travel through a longer, more resistive path to reach the next cell. The key insight in this chapter is that these corrosion processes affect the module I-V characteristics differently, and therefore the electrical I-V signatures can be used to infer the types of corrosion processes within the module. We will explain how variation of these markers may be misinterpreted as signatures of different degradation mechanisms.

5.2 Simulation Framework

We used a commercial cell simulator called GriddlerTM [162] to calculate the J-V curves of cells with variously corroded/delaminated finger and busbars. Griddler needs as an input a map of the busbar and fingers as a starting point of the simulation. Therefore, we first used AutoCAD software to draw the relevant (pristine or corroded) patterns of fingers, busbars and tabbing points on the front side of the wafer. The backside was presumed fully covered with an opaque metal. Griddler uses the front grid pattern as a guide to spatially resolve the cell into small segments. Each spatial segment (i.e. node) is represented by a double diode five-parameter compact model (see Fig. 5.2). The five-parameter equation is given by:

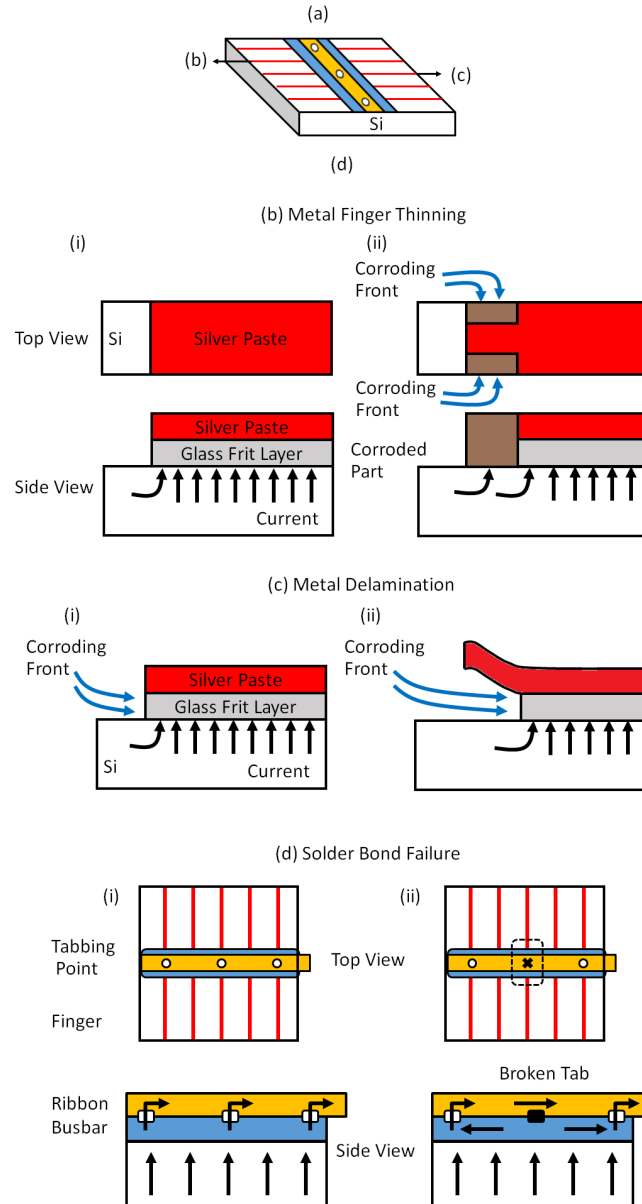


Fig. 5.1. (a) A schematic of a section of a solar cell and locations where three types of degradation may occur. Simple schematics of how corrosion changes the metal contacts and current path in the fingers, busbars, ribbon, and Si wafer when (b) metal thinning (c) metal delamination and (d) solder bond failure occur. (i) Before degradation, (ii) After degradation. (The glass frit allows electrical contact to the silicon surface after deposition of the anti-reflective coating during contact firing. [161])

$$\begin{aligned}
J(x, y) = & J_{ph}(x, y) - J_{01}(x, y) \left(e^{\frac{V(x, y) + J(x, y)R_s(x, y)}{k_B T/q}} - 1 \right) \\
& - J_{02}(x, y) \left(e^{\frac{qV(x, y) + J(x, y)R_s(x, y)}{2k_B T/q}} - 1 \right) - \frac{V(x, y) + J(x, y)R_s(x, y)}{R_{sh}(x, y)}
\end{aligned} \tag{5.1}$$

The five parameters are: (a) $J_{ph}(x, y)$, the photo-current density generated due to local illumination; (b) $J_{01}(x, y)$ is the diode recombination current with an ideality factor of one; (c) $J_{02}(x, y)$ is recombination current in the depletion region of the diode with an ideality factor of two; (d) $R_{sh}(x, y)$ is the local shunt resistant; and (e) $R_s(x, y)$, the series resistance. The baseline values that we used for different variables in the GriddlerTM simulator are summarized in Table 5.1. The variables are chosen for a typical c-Si cell with an efficiency of 18.8%.

Once the local five-parameter model is specified, Griddler connects the nodes in a two-dimensional grid (see Fig. 5.2b) with appropriate front/back contact resistance and then solves the Kirchhoff's equations related to the network with appropriate boundary conditions (e.g., voltage and current specified at the end of the busbars). A self-consistent solution of the Kirchhoff's law allows one to obtain a spatially resolved map of voltage and current distributions, $V(x, y)$ and $J(x, y)$. This map allows us to interpret cell I-V characteristics in terms of local processes.

For example, Fig. 5.2c shows the calculated voltage distribution for a pristine cell with two vertical busbars and a series of 82 horizontal fingers. The current is extracted at the bottom edge of the busbars (marked A and B), therefore these two points at the cell output (or module voltage, V_M) has the smallest voltage ($V_{min} = 0.555V$, black). The busbars are essentially at the same potential (vertical black lines), because the resistances of the busbar is small. The local voltage differential

$$\Delta V(x, y) \equiv V(x, y) - V_{min} = V(x, y) - V_M \leq \Delta V_{max}$$

depends on the distance from the initial charge collection point on the finger (e.g. C, D, and E) to the final extraction point (i.e. A and B) at the busbar. At the farthest point from the busbar (C, D, E), the voltage is the highest ($V_{max} = 0.596V$, white), with the corresponding maximum voltage differential ($\Delta V_{max} = V_{max} - V_{min} \sim 40mV$). Thus, for a pristine module, $\Delta V_{max} \sim 1.5 \frac{k_B T}{q} > \Delta V(x, y)$, therefore charge

collection from various points within the cell is essentially uniform, because exponential terms on the right hand side of Eq. 5.1 are essentially identical, i.e. $V(x, y) \equiv V_{min} + \Delta V(x, y) \sim V_{min}$. This conclusion does not hold once the fingers/busbars begin to corrode, with dramatic implications for cell performance, and I-V characteristics.

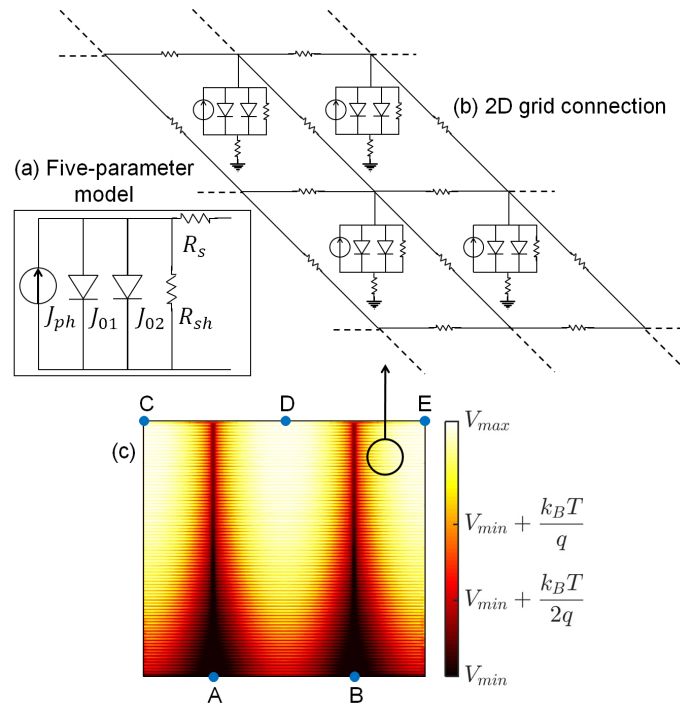


Fig. 5.2. (a) A schematic of the Five-parameter model. (b) Two-dimensional grid connection of the five-parameter model in Griddler. The magnitudes of the circuit elements depend on the location within the cell. (c) Voltage map distribution of a pristine cell. The difference between V_{min} and V_{max} is in order of $\frac{k_B T}{q}$, allowing highly efficient current collection from any location within the cell.

5.3 Effect of Finger Corrosion and Solder Bond Failure

When a module is installed in the field, it is exposed to environmental humidity. Moisture first penetrates the module through cracked sealant, power plugs, (fractured)

Table 5.1.
Baseline Simulation Parameters for Cells in Griddler

Property	Value
Finger sheet resistance	3 $m\Omega/sq$
Busbar sheet resistance	3 $m\Omega/sq$
Finger contact resistance	0 $m\Omega/sq$
Layer sheet resistance	80 Ω/sq
Wafer internal series resistance	0 $m\Omega.cm^2$
Internal shunt conductance	0 $1/(\Omega.cm^2)$
Ribbon width	1 mm
Ribbon sheet resistance	0.1 $m\Omega/sq$
Contact point resistance	0 $m\Omega$
Number of tabbing points on ribbon	15
1-sun J_{ph} , non-shaded area	39.6 mA/cm^2
J_{01} , passivated area	200 fA/cm^2
J_{01} , metal contact	600 fA/cm^2
J_{02} , passivated area	10 nA/cm^2
J_{02} , metal contact	50 nA/cm^2
Finger pitch	1.9 mm
Finger width	60 μm
Number of fingers	82
Busbar width	1.5 mm
Number of busbars	2
Cell area	243.36 cm^2
Front illumination	1 $Suns$

glass, and/or cracked backsheet. Subsequently, moisture diffuses through the encapsulant to eventually reach the solar cell. Moisture may corrode the fingers/busbar of a solar cell in two ways. First, in the dark-corrosion mode, moisture initially reacts with the encapsulant EVA to produce acetic acid [163]. The acid corrodes parts of glass frit layer in contact with silicon and the corresponding “delamination” increases the series resistance [164]. In the light-corrosion mode during normal daytime operation, moisture is directly hydrolyzed at the metal contacts and the OH^- molecule reacts with the metal to produce metal hydro-oxides (MOH^-). The hydro-oxides is eventually neutralized by PID-related Na^+ ions from the front glass [165]. This corrosion of the glass layer or the delamination of the electrode due to the build-up of H_2 gas (hydrolysis product) degrade current collection. The actual reactions are complex and still subject to intense study [165–168].

In this chapter, we will not focus on the kinetics of corrosion, but rather analyze the I-V signature of CDS once it has occurred. As discussed, corrosion can thin the grid finger by dissolving away the metal from the cell edges located close to the module edge (Fig. 5.3) or cause delamination of the contacts along the length of the finger (Fig. 5.5). These two phenomena are among several effects that can be associated with corrosion. Then we will explain the effects of each corrosion pattern in the following subsections. In addition, the busbar solder bond failure that occurs due to thermal expansion and contraction will be discussed with reference to Fig. 5.7.

5.3.1 Metal Finger Thinning

Thinning of the metal fingers occurs when the corrosion attacks the contacts from the edges. For simplicity, we assumed the thinning happens uniformly for a length of 3.0 cm (see Fig. 5.3a). This pattern may arise because corrosion is slower than moisture diffusion, although exact details of the corrosion pattern will not affect the key insights presented in this chapter. The simulation set-up only affects the finger

resistance. Therefore one expects that the changes of the I-V characteristics would be attributed to the increase in effective series resistance, R_S .

Interestingly, the thinning of the fingers does not affect I-V curve significantly until five-sixth of the initial width ($60\mu m$) is corroded (see Fig. 5.4). The fingers are over-designed to ensure high yield, therefore despite initial corrosion reducing the width of the finger, the voltage drop along the finger ($\Delta V(x, y)$) is relatively small and the voltage redistribution (Fig. 5.3b) and the cell performance (Fig. 5.4a) appears indistinguishable compared to pristine cells.

The voltage distribution (Fig. 5.3b) and the I-V characteristics (Fig. 5.4a) begin to change significantly when the finger width is reduced to $10 - 20\mu m$). Now the finger current travels laterally through the high resistance corroded section (or the semiconductor underneath) until it reaches the healthy section of the finger. The voltage over the corroded section in Fig. 5.3b approaches $V_{max} = 0.610V$ (white) or $\Delta V_{max} \sim 60mV > 2\frac{k_B T}{q}$. As $V_M (= V_{min})$ is increased, the distributed diodes in the corroded section are turned on even more strongly (due to their exponential dependence of $\Delta V(x, y)$, as in 5.1). The I-V characteristic in Fig. 5.4a gives the appearance of a weakly “shunted” cell. The output power is reduced as diodes now dissipate the local photo-current instead of allowing them to be collected by the busbar. Interestingly, Ref. [169] anticipated “fake shunt” as a consequence of two regions of a cell (pristine vs. degraded) being described by two different series resistances. The present work provides a detailed physical justification regarding the spatially distributed origin of the fake shunts.

Finally, when most of the finger is corroded (e.g., $59.5\mu m$ out of $60\mu m$), $\Delta V_{max} = 110mV$ (Fig. 5.3c, white section on the left) ensure that strong diode turn-on dissipates most of the local photo-current within the corroded section. The short-circuit current is reduced in a manner similar to yellowing or partial vertical shading. The situation is worse, because the hot spots formed will accelerate corrosion/delamination.

To summarize, initial corrosion may not affect the I-V characteristics at all. Intermediate corrosion ($40 - 55\mu m$) is reflected as a fake shunt resistance (indicated by

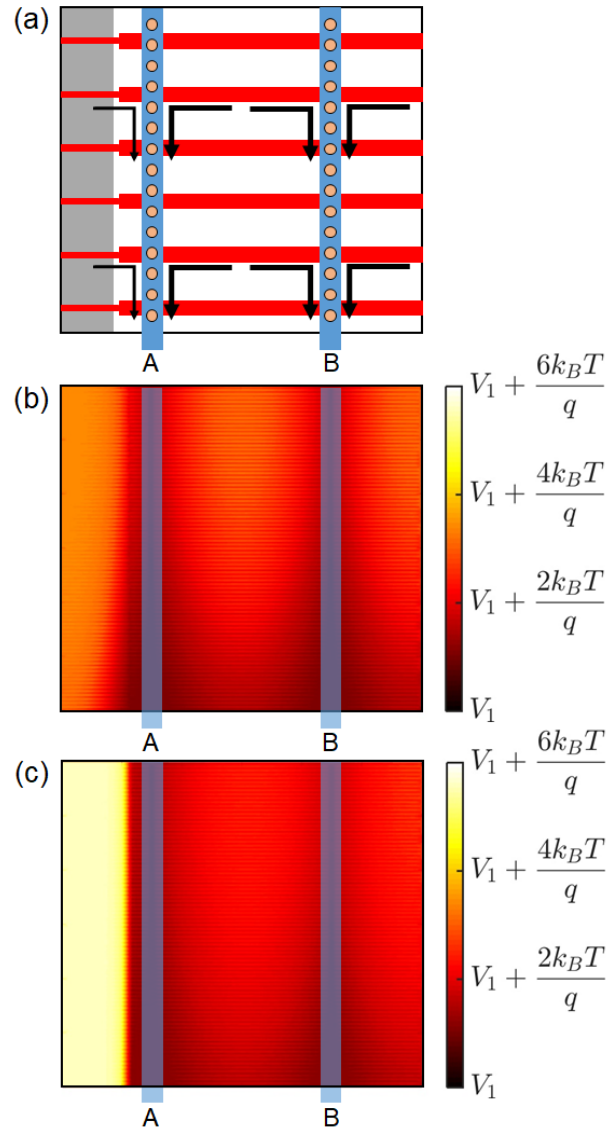


Fig. 5.3. (a) A schematic diagram of grid configuration associated with finger thinning. (b) and (c) show corresponding voltage map at V_{MP} where $40.0\mu\text{m}$ and $59.5\mu\text{m}$ out of $60.0\mu\text{m}$ of the finger width have been corroded. Arrows show a general current collection path. Thinner arrows indicate less current is being collected due to finger thinning. Shaded area in (a) corresponds to the brighter part in (b) and (c) that have higher voltage drop. A large portion of current in shaded area is being sunk in the strongly turned on diodes and does not contribute to total collected current.

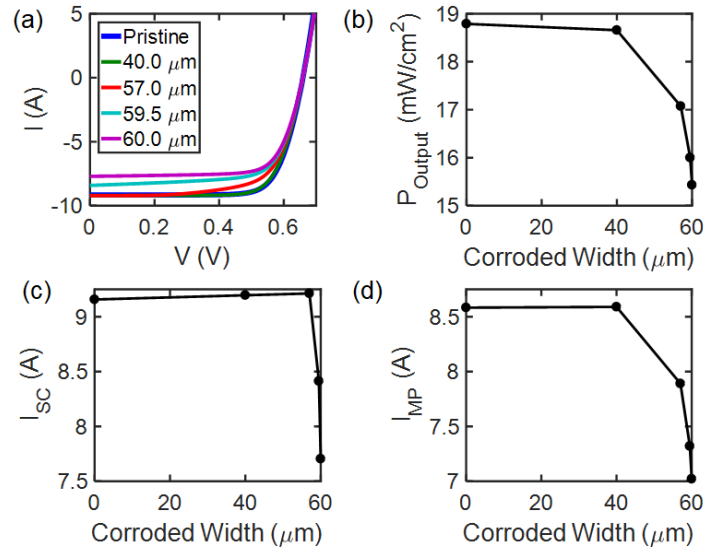


Fig. 5.4. I-V curves associated with five different corroded finger widths. The output power follows the I_{MP} trend. The slight I_{SC} increase is due to partial removal of the contacts and reduced shading of contacts. Significant output power reduction starts after $50\mu\text{m}$ corrosion of the finger width.

the slope at $V=0$) at the terminal I-V characteristics. At the final stages of corrosion, the I-V characteristics resemble partial shading and local yellowing. Thus, finger corrosion is susceptible to mischaracterization at the I-V level. This misinterpretation is especially dangerous when one wishes to differentiate Potential Induced Degradation (PID) (that affects the shunt resistance) from finger corrosion solely based on the terminal I-V characteristics.

5.3.2 Metal Delamination (Glass Frit Corrosion under Dark)

The dark and light corrosion can delaminate (or fully corrode) the fingers and busbars from the semiconductor underneath. For simplicity, let us assume that moisture diffuses uniformly from the side close to the module edge. Therefore, the fingers are fully delaminated the same length (see Fig. 5.5a), which is equivalent to the worst

scenario in metal finger thinning. Fully delaminated fingers cause the current to travel laterally towards the healthy parts of the finger through the semiconductor and be collected by the remaining fraction of the finger. Since the semiconductor resistance is relatively higher, $\Delta V(x, y) \gg \frac{k_B T}{q}$ is significant in the white delaminated section of the cell as shown in Fig. 5b. The turned-on diodes shunt the current, almost none of the photo generated carriers are collected from this region, the short-circuit current is reduced (Fig. 5.6c) and the power drops linearly with delaminated area. This effect is similar to yellowing or shading that also reduce the J_{SC} without any change in FF, again suggesting the possibility of mischaracterization. Visual inspection or IR imaging will differentiate the degradation modes: yellowing does not produce local hot spots, but grid delamination do.

In closing this section, let us reiterate that the series resistance has remained essentially unchanged even in this extreme case of finger corrosion. Does corrosion ever lead to series resistance increase, as presumed in the traditional literature? Yes, it does but only for solder bond failure – the topic of the next section.

5.3.3 Solder Bond Failure

Thermal expansion/contraction during thermal cycling or hourly/daily/seasonal temperature variation can cause solder bond failure or broken tabbing points. To model the solder bond failure in Griddler, we sequentially remove the tabbing points between the ribbon and the busbar. The ribbon is in contact with the whole length of the busbar and the transfer conductivity may increase slightly at the tabbing points. Therefore, the current is now forced to take alternate paths in higher resistance busbars, leading to a fundamentally altered voltage distribution pattern in the cell. The broken tabbing points are a discrete way of representing a failure that in principle could occur at any point along the busbar.

Pristine cell voltage map $V(x, y)$ is shown Fig. 5.2c, with ribbons and tabbing points intact. When a tabbing point fails, the current reroutes through the busbar and

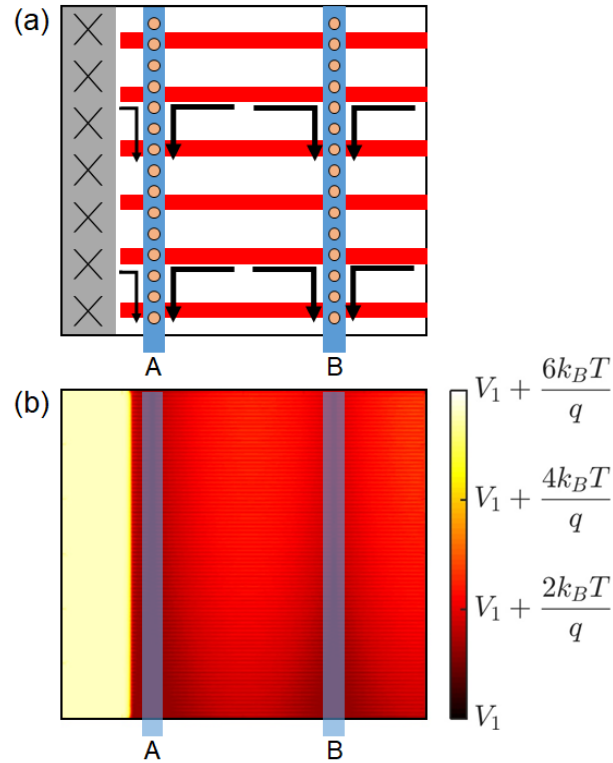


Fig. 5.5. (a) Finger delamination schematic and (b) voltage map at V_{MP} where 3 cm out of 15.6 cm finger length has been delaminated. Arrows show a general current collection path. Thinner arrows show less current is being collected due to finger delamination. Shaded area in (a), corresponding to brighter part in (b), does not contribute to total collected current. All of the current in this part marked by “x” is being sunk in the strongly turned on diodes and turns to heat.

reaches the adjacent tabbing point (see Fig. 5.1d). If the failed tabs are consecutive and close to current collection plugs (bottom of the cell at points A and B), this rerouted path leads to a large resistive drop, with a dramatic increase in $\Delta V(x, y)$, as shown in Fig. 5.7b (7 bottom tabbing points removed). The arrows indicated the rerouting of the current flow. As a result, the photo-generated current at the bottom edge of the cells (white region) may not be as efficiently collected. Interestingly, as the first tabbing points starts at the “middle” of the cell, the voltage is redistributed

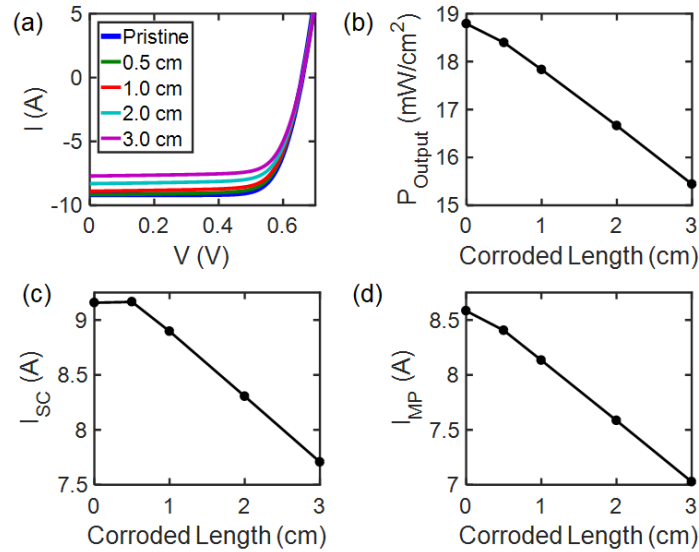


Fig. 5.6. I-V curves for five different corroded lengths. The output power follows the I_{MP} trend. The voltage drop is not significant when 0.5 cm of length is corroded, therefore, the I_{SC} does not drop.

leading to more efficient charge collection from the remainder of the cell, as shown in Fig. 5.7b.

Fig. 5.8a shows that solder bond failure manifests a distinct signature of series resistance both in FF and slope of the I-V curve close to V_{OC} . This is because any corrosion at the tabbing point and/or ribbons affects not the local current, but the integrated current of the cell. In addition, close to V_{MP} when the voltage drop is high enough for the distributed diodes to turn on, there is a significant loss of current collection. However, the drop is not high enough at I_{SC} , thus no reduction in I_{SC} .

5.4 Cell vs. Module I-V Characteristics

Degradation mechanisms such as corrosion reduce output power at the cell level, but how does corrosion affect the module performance that contains a combination of corroded and healthy cells? After all, qualification or field tests are done on the encapsulated module where the I-V characteristics of individual cells are not available.

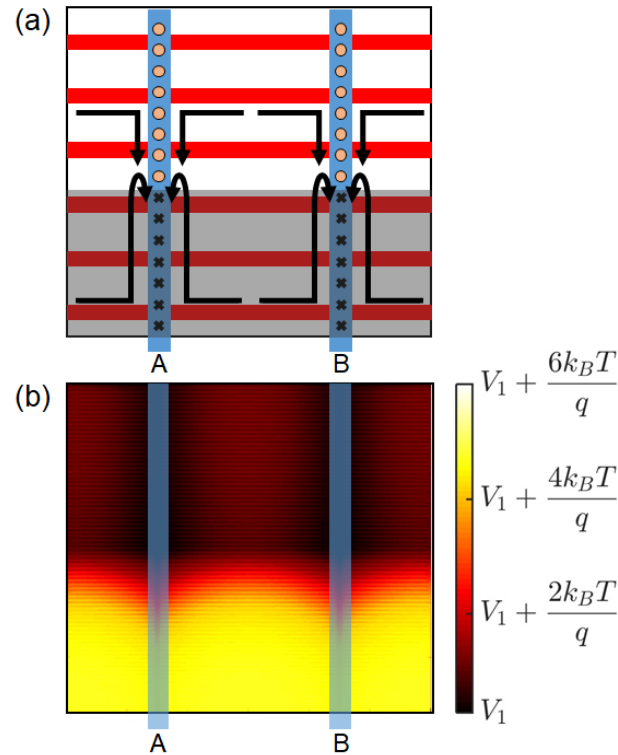


Fig. 5.7. (a) Solder bond failure schematic and (b) voltage map at V_{MP} where 7 bonds (tabbing points) out of 15 have been broken. Arrows show a general current collection path from fingers to busbars and then ribbons. The portion of current in shaded area (a) goes through a longer and more resistive path in the busbar to reach the first healthy tabbing point. Due to the metallic resistivity of the path that current goes through the voltage drop is not high enough to turn the diodes on and sink current significantly at low bias.

Since only a few cells of a module may be affected by CDS, it is important to know how the cell level degradation translates to module-level I-V characteristics. Many field inspections report degradation occurs at the edges of a module [170–172], especially when the module is encapsulated by a moisture resistant backsheet [173]. If the backsheet allows moisture penetration, however, then every cell of the module is degraded by moisture diffusing through the white spaces among the cells. Therefore, Fig. 5.9a shows N degraded cells along the edges of the module, with M healthy

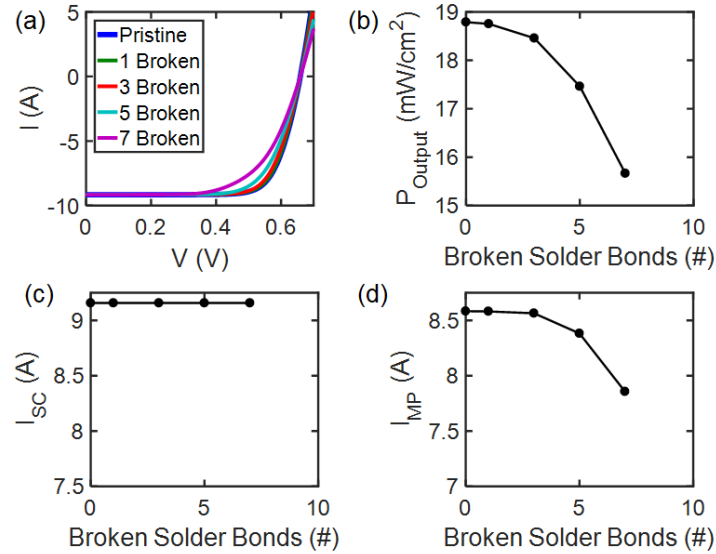


Fig. 5.8. I-V curves as a function of the number of broken solder bonds. Since the voltage drop is not significant at I_{SC} there is no change in I_{SC} even when almost half of the bonds are broken. However, the I_{MP} drops as the voltage drop over the broken bonds increases.

cells at the interior of the module. The exact location of the degraded cell in this series connected system is unimportant, so long M and N are specified. As shown in Fig. 5.9b-d, we find that the features of cell I-V characteristics (following CDS degradation) is preserved in module I-V characteristics. This occurs despite the complexity of the voltage and current redistributions among the degraded and pristine cells. For example, Fig. 9b shows that finger thinning at the cell level appears as a shunt resistance even at the module level. Similarly, finger delamination at the cell level translates to suppression of the module short-circuit current; see Fig. 5.9c. Finally, solder bond failure leads to an increase in the series resistance, as in Fig. 5.9d. Note that the presence of healthy cells reduces the magnitude of the series resistance seen at corroded cell I-V characteristics. When the effects are present simultaneously, (i.e. some cells are delaminated, while others have lost the tabbing contact) the module characteristics is defined by a convolution of the elemental features.

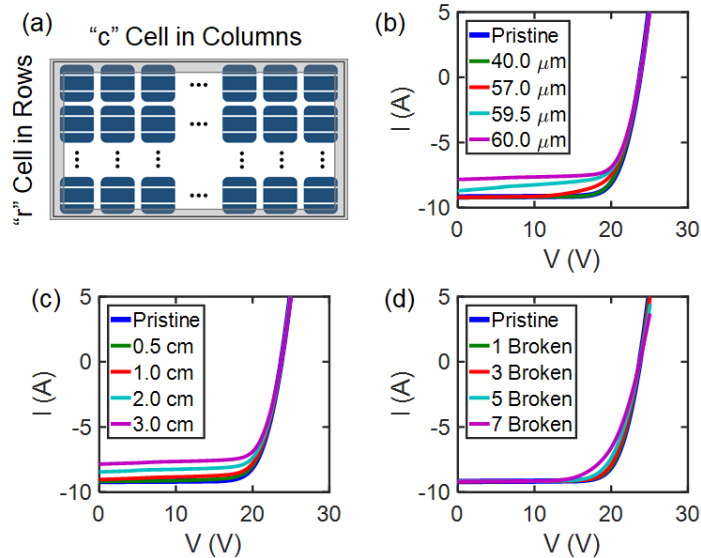


Fig. 5.9. (a) A schematic of the degraded cells within a module. Here, N is the number of degraded cells $N = (r + c - 2) \times 2$, whereas M is the number of healthy cells $M = r \times c - N$ ($M = 10, N = 26$). We assume only the edge cells in the gray area degraded due to corrosion. Module level I-V curves synthesized using cell level results of Griddler I-V curves for different degradations involving: (b) metal finger thinning, (c) finger delamination, and (d) solder bond failure.

Finally, in Fig. 5.10 we plot the power output of the pristine and damaged cells (as well as their combined effect on module performance) to show that the redistribution of the cell voltages alters the maximum power point of the module. This redistribution affects all of the cells (including the pristine cells) with the corresponding decrease in the power output.

5.5 Discussion

Since CDS manifest variously as R_{sh} decrease (finger thinning), I_{SC} loss (grid delamination), and/or R_S increase (solder bond failure), it is important to distinguish the signature of CDS from other degradation mechanisms, such as PID (R_{sh} decrease) and/or shadowing or yellowing (I_{SC} loss). First, it is clear that severe R_S -increase

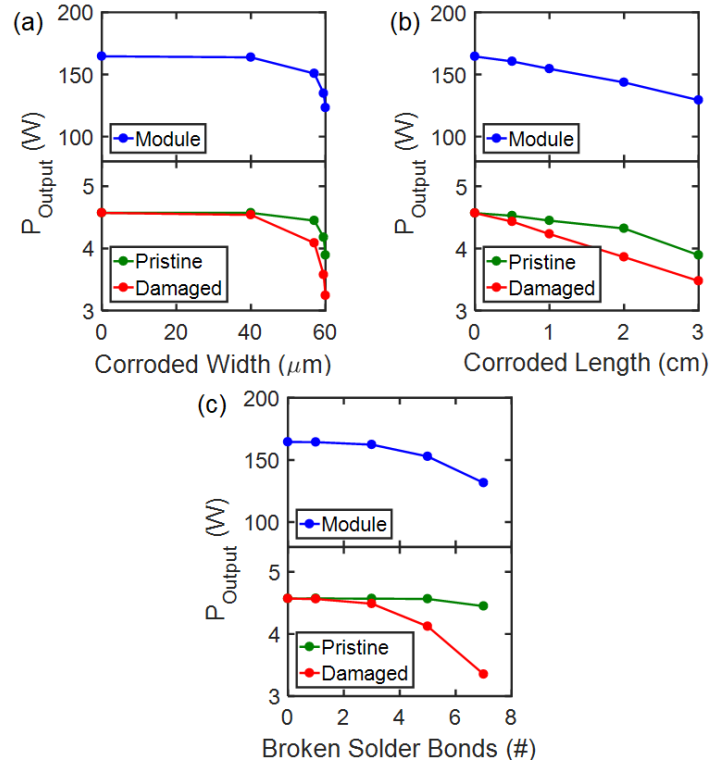


Fig. 5.10. Breakdown of power output for cells and module as a function of (a) corroded width (metal finger thinning), (b) corroded length (finger delamination), and (c) number of broken bonds (solder bond failure).

can always be positively correlated to solder-bond failure, provided that the failure is confined to the internal circuitry of the cell. However, the R_S -increase can be due to external component issues such as corroded external connectors, faulty junction box, broken ribbons, etc. We have extracted series resistance using the five-parameter model and plotted the results in Fig. 5.11. We find that the variation in R_S is significantly larger in case of solder bond failure ($\Delta R_S/R_S = 100\%$) compared to finger delamination ($\Delta R_S/R_S = 4\%$) or metal thinning ($\Delta R_S/R_S = 12\%$). For cross-validation, we recalculated R_S by taking the slopes of the I-V curves close to open-circuit condition, with essentially identical results. Hence, we conclude that severe changes in the series resistance is positively correlated solder bond failure. Similarly, R_{sh} extracted by the five-parameter model reflects the change in the I-V curve slope

close to the short-circuit condition. The physical shunt resistance included in the Griddler simulation is very high, and yet five-parameter model finds a (fake) shunt resistance (as shown in Fig. 5.11b,d), arising from the diode turn-on due to metal thinning and metal delamination. The R_{sh} extracted from the five-parameter model due to solder bond failure is comparable: initially, we find no-evidence of fake shunt because diode turnout due to the failure of a few tabbing points is essentially uniform. With increasing bond-failures, however, the non-uniformity of the diode turn-on is reflected in the dramatic decrease in the fake shunt resistance. The other effects may be differentiated by the following electrical/optical characterization methods.

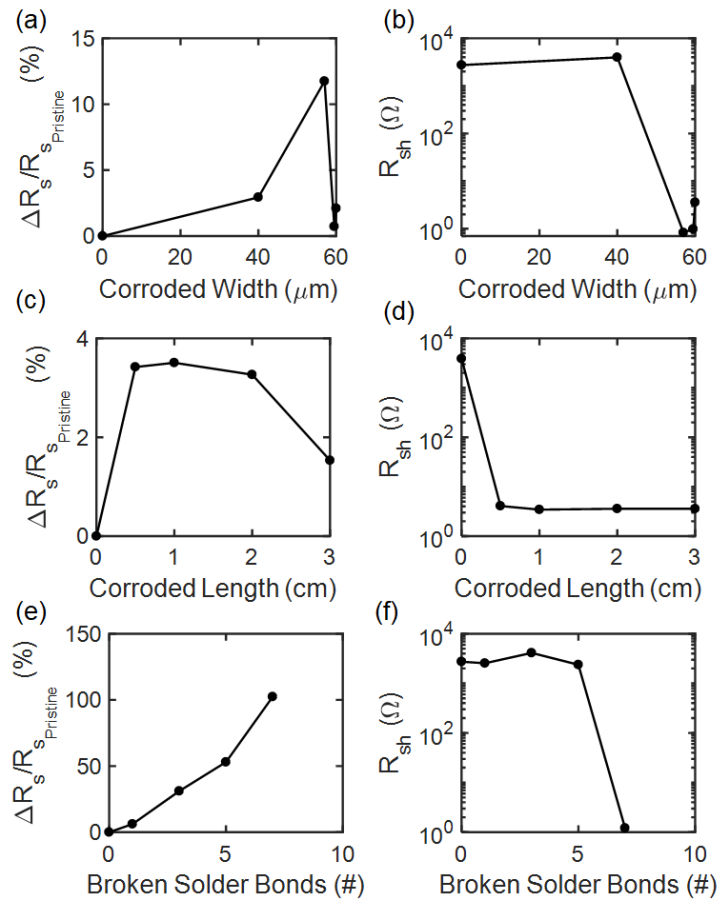


Fig. 5.11. The changes of series resistance and shunt resistance are plotted as a function of (a,b) corroded width, (c,d) corroded length, and (e,f) the number of broken solder bonds. Here, $R_{S_{Pristine}} = 4.2 \times 10^{-3} \Omega$

5.5.1 Reverse Bias Characteristics

Finger corrosion related “diode shunts” saturates at sufficiently high reverse bias, while PID related increase in “real” shunt current increases with reverse bias. Thus, reverse bias characteristics will differentiate between the two degradations. In addition, PID on its own does not change the short-circuit current in p-type c-Si cells [174], but in n-type c-Si cells the short-circuit current is influenced and the slope of I-V curve at low voltage alters negligibly [175, 176]; however, finger corrosion may affect I_{SC} depending on its severity (as shown in Fig. 5.4). A Griddler simulation of the under illumination I-V shown in Fig. 5.12 demonstrates the feasibility of this approach. In practice, the approach may require removal of the protection diodes from a module and carefully ensure that the cells do not go into reverse breakdown.

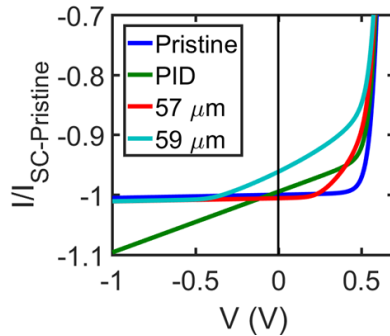


Fig. 5.12. The I-V characteristics compare PID vs. various degrees of finger thinning (e.g. $57\mu m$ and $59\mu m$ out of $60\mu m$ width). We assume that the area affected due to these two degradation mechanisms are equal.

5.5.2 Irradiance Dependent Efficiency

If the reverse bias part of I-V characteristic is not available then we can use irradiance as a probe to distinguish between the fake and the real shunt. Fig. 5.13 shows that compared to pristine characteristics, the efficiency-irradiance plot is affected significantly only if the shunts are real (e.g. PID). Although this method distinguishes

between fake and real shunt, we may not be able to positively identify the mechanism that led to the real shunting formation.

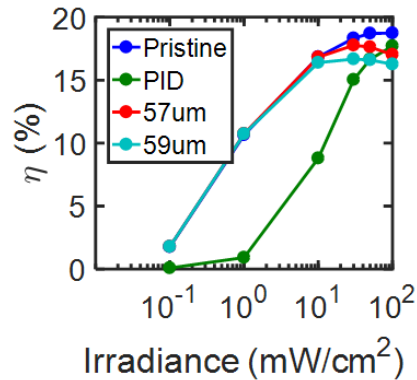


Fig. 5.13. Irradiance dependence of efficiency. At lower irradiance, a real shunt (related to PID, for example) reduce the cell efficiency much more significantly compared to a fake shunt (associated with finger corrosion).

5.5.3 Optical Measurement to Distinguish between Yellowing and Delamination-induced Loss in Photo-current

Grid delamination-induced I_{SC} -loss leads to local dissipation of photo-current and corresponding localized increase in self-heating and cell temperature. Yellowing prevents photons from reaching the cell, and thus the loss of photo-generated current is not related to the local hot-spot formation. Therefore, an IR image should differentiate between these two degradation modes. Another way to distinguish between the two is visual inspection. Yellowing generally affects most of the area of the module/cell; however, grid delamination normally occurs close to the edges of the module/cell. Finally, one may analyze the I-V curves at reverse bias. As shown in Fig. 5.14 yellowing reduces the short circuit current, but does not affect the slope of the curve at reverse bias. Delamination, on the other hand, not also reduces the

short-circuit current, but also features a shunt like signature at reverse bias associated with gradual turn-off of the diodes far from the current collection points.

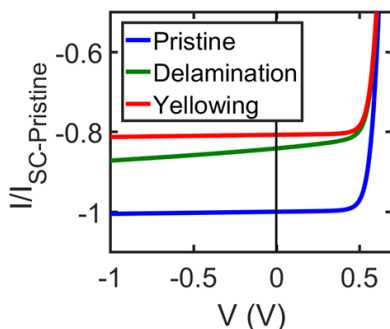


Fig. 5.14. Irradiance dependence of efficiency. At lower irradiance, a real shunt (related to PID, for example) reduce the cell efficiency much more significantly compared to a fake shunt (associated with finger corrosion).

5.5.4 Combination of Degradation Mechanisms

The discussed methods can distinguish the mechanisms when only one is influencing the cell/module. If two or more mechanisms affect the I-V curve simultaneously, (e.g. yellowing and PID) the features of I-V characteristics may be mischaracterized as being due to grid delamination. Therefore, it may not possible to distinguish between the mechanisms only relying on electrical characterization. Other methods such as visual inspection and/or IR imaging will be helpful. Yellowing uniformly affects the module and is easy to spot by visual inspection [172]. IR imaging will spot the shunted areas due to higher recombination in the PID affected parts. Thus, it is possible to differentiate between the mechanisms based on electro-optical multi-probe characterization methods.

5.6 Summary and Conclusion

In this chapter, we have used Griddler, a solar cell and module simulator, to investigate the effects of CDS on the performance of solar cells. We find that: (a) only solder bond failure directly increases the series resistance of the cell (compared to other two degradations studied in this work), as characterized by the derivative close the open-circuit condition; (b) finger thinning does not affect the performance of cell significantly until the finger width reduces to less than $10\mu m$. The electrical signature of finger thinning is a steeper slope in lower voltages, which may be mischaracterized by shunt resistance. Reverse bias I-V characteristics may be used to distinguish between diode shunt due to corrosion, and actual shunt due to PID, for example. Finally, finger delamination reduces the performance by sinking the photo-generated current locally and reduces J_{SC} . An optical image, IR image of hot-spot formation, and a slope of I-V curve at reverse bias help differentiate between yellowing and finger delamination. A deep and nuanced understanding of the complex correlation of a degradation mode and its electrical signatures (reflected in the I-V) characteristics is essential for interpreting the qualification tests and fields results and improve the next generation of solar modules manufactured for a specific weather zone.

So far we have shown that solder bond failure increases the series resistance via simulation and some experimental results found in the literature. In the next chapter we will validate this direct correlation based on measurements such as dark lock-in thermography that can pinpoint the hotspots count. Hence the correlation is easy to identify.

6. DLIT IDENTIFIES SOLDER BOND FAILURE AS THE ROOT CAUSE OF THE SERIES RESISTANCE INCREASE

Note: The material in this chapter has been adapted from Ref. [177]

Correlating the electrical performance of photovoltaics (PV) modules to the spatially-resolved photoluminescence (PL), electroluminescence (EL) and dark lock-in thermography (DLIT) images is an important long-term goal for developing solar cell technology. These images offer highly sophisticated and detailed information about the spatial distribution and (if imaged at successive time intervals) temporal degradation of local series and shunt resistances. There have been extensive studies to correlate these imaging techniques to local characteristics at the cell level, however, it has been difficult to extract and quantify module-level information from the techniques. In this chapter, we interpret module current-voltage (I-V) measurements along with corresponding DLIT images within a module-scale simulation framework, demonstrating that series-resistance degradation of the module I-V characteristics, in this case, can be attributed to solder bond failures. Our simulations highlight how current crowding associated with a failed solder joint (or a section of the solder pad) translates to the characteristic point-like (asymmetric-doublet) heating pattern in neighboring solder joints (or the neighboring regions of the pad). The correlation between series resistance and solder joint/pad degradation would inform an expedited diagnosis of the field degradation of solar modules.

6.1 Introduction

With the accelerated worldwide deployment of solar farms, the rapid evolution of solar cell technologies (e.g. from standard back surface field (BSF) to passivated

emitter and rear contact (PERC) to bifacial heterojunction with intrinsic thin layer (HIT) cells) has created a need for developing diagnostic methods that correlate the module performance to the underlying design parameters of a solar cell. The diagnostic techniques belong to two categories. The first group includes analytical techniques such as electroluminescence (EL), photoluminescence (PL), and dark lock-in thermography (DLIT), which provide highly sophisticated, spatially-resolved information regarding a solar module. The second group involves various electrical characterization techniques, such as current-voltage (I-V), Suns-Vmp method, etc. that provide module-integrated information about the solar cells. A physics-based correlation between the two classes of techniques would allow one to interpret the electrical signatures of the intensity and temperature-dependent I-V characteristics of fielded modules in terms of the physical degradation processes typically obtained by EL, PL, and DLIT measurements.

There are many examples of previous efforts to correlate analytical and electrical techniques. For example, in a pioneering contribution, Sinton and Cuevas [178] presented a method to calculate the carrier lifetime and implicit I-V curve using photoconductance data. Fada et al. [179] have shown how the exposure to the damp heat test correlates to I-V characteristics of c-Si modules. Karimi et al. [180] have used machine learning to correlate EL image features with I-V characteristics. Recently, Sun et al. [181] proposed a method called Suns-Vmp that only uses the maximum power point voltage and current of the c-Si modules at different times of the day to extract the characteristics and diagnose the possible issues of the module. In other words, the Suns-Vmp method relies on a solar farm as a natural testbed of solar modules with variable light intensity and temperature. Similarly, Asadpour et al. [147] demonstrated that by analyzing the I-V curve signatures and intensity-dependent efficiency of c-Si solar modules one can determine the increase in the series resistance due to solder bond failure and distinguish “fake shunt”, due to finger corrosion/delamination, from a real shunt due to Potential Induced Degradation (PID). While correlating the electrical signatures to the underlying mechanisms causing them are physically

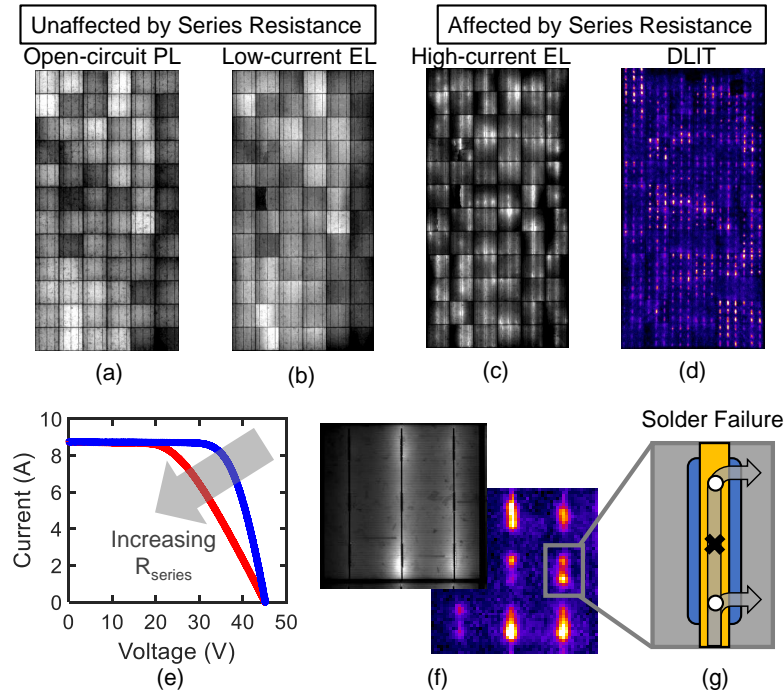


Fig. 6.1. (a-d) EL/PL/DLIT help characterizing local resistance of the cell since they contain spatially-resolved information on the position of increased resistance. In contrast, (e) the I-V measurements give us information about module-level series resistance. (f) The EL image highlights the location of back-side solder pads, and there is higher EL signal near certain solder pads. The DLIT shows non-uniform heating at back side solder pads. (g) The zoomed in schematic shows that solder bond failure can lead to series resistance degradation, which manifests itself as localized hotspots in DLIT/EL images.

justified and they can interpret a variety of experiments self-consistently, they have rarely been supported by spatially-resolved characterization techniques, such as EL, PL, etc.

Over the years, spatially-resolved characterization methods have become increasingly more sophisticated and powerful. For instance, in 2005 Fuyuki [182] for the first time used a cost-effective silicon CCD camera to image EL in a silicon solar cell, which enabled wider-spread use of imaging for silicon solar cell characterization. The most common use of EL imaging has been to link luminescence signatures to

spatial variation in cell voltage, which has been applied in both silicon [183] and in thin-film solar cells [184]. However, at increasing current densities, series resistance begins to affect the EL images, which causes deviation from the low-current, resistance-free voltage maps. Based on this, Hinken et al. [183] demonstrated the use of EL voltage-dependent imaging for series resistance characterization. In the early 2000s, Breitenstein popularized the use of DLIT for mapping PV performance metrics based on power dissipation, and since then combining DLIT with EL and PL imaging has become a robust approach for identifying local I-V metrics, as demonstrated in Refs. [185, 186] which measure local diode saturation current and series resistance. Similarly, Augarten et al. [187] combined PL and DLIT to estimate local shunt resistance, and Kendig et al. combined thermal imaging with EL to identify weak diode defects in thin-film solar cells [188]. Refs. [189, 190] further demonstrate that each characterization technique has a different strength for extracting different local parameters.

Despite the many cell-level studies that quantify device metrics from luminescence and thermal imaging, there has been a persistent gap in translating the microscopic images to macroscopic module-level electrical signatures. Fig. 6.1 shows that imaging techniques focus on the local parameters, however, if combined with I-V measurements, it would be possible to extract a significant amount of additional and complementary information from the techniques. This occurs in part because the complex current flow patterns and highly nonlinear diode/shunt characteristics remaps/transforms the information about local degradation to very different features of the module-level I-V characteristics. In this regard, we explained in a recent paper that the corrosion/delamination leads to “fake shunt” resistance and solder bond failure to series-resistance losses [147].

In this chapter, we find a direct correlation between the number of solder bond failures obtained from DLIT images with the series-resistance degradation derived from module I-V characteristics. A systematic analysis of the DLIT images and its implications for the I-V characteristics confirm the correlation. The rest of the

chapter is arranged as follows. In section II we explain the theory of how broken solder bonds cause current redistribution, and we show the simulation results confirming the theory. In section III we validate the theory by experimental results and show the correlation of hotspots and series resistance due to solder bond failure. Finally, in section IV we conclude the chapter.

6.2 Theory and Simulation: Current Redistribution in Modules with Broken solder bonds

To understand how a solder bond failure can be experimentally observed in a DLIT experiment and to correlate it to the series resistance, we must first understand the hierarchical current flow in a crystalline silicon solar module. During current collection in a crystalline silicon solar cell under illumination, the fingers first collect the distributed photo-generated carriers and funnel them to the busbars. Subsequently, the solder bonds act as bridges for the current to be transferred from the busbars to the ribbons. The physics of this hierarchical current collection within an illuminated module has been discussed in detail in Ref. [147]. A similar hierarchical current collection occurs at the backside of the solar cells through the multiple sections of the solder pads.

For the purposes of this chapter, we will instead focus on the dark I-V characteristics. When the module is in the dark and a forward bias voltage is applied between the external terminals, Fig. 6.2 shows that the solder bonds allow the input current to flow from the ribbon to the busbars. The current in the busbar is then funneled through the fingers and passes through the semiconductor (forward-biased p-n junction) to reach the grounded back-surface. Due to distributed voltage drops, the current through the solder bonds is not equal. For example, the solder bonds closer to the current injection points (A, B at the bottom) carry more current towards the busbars (indicated by the longer arrow also see Fig. 6.3f). This reflects the fact that the diodes closer to the injection points (A, B) are more strongly forward biased,

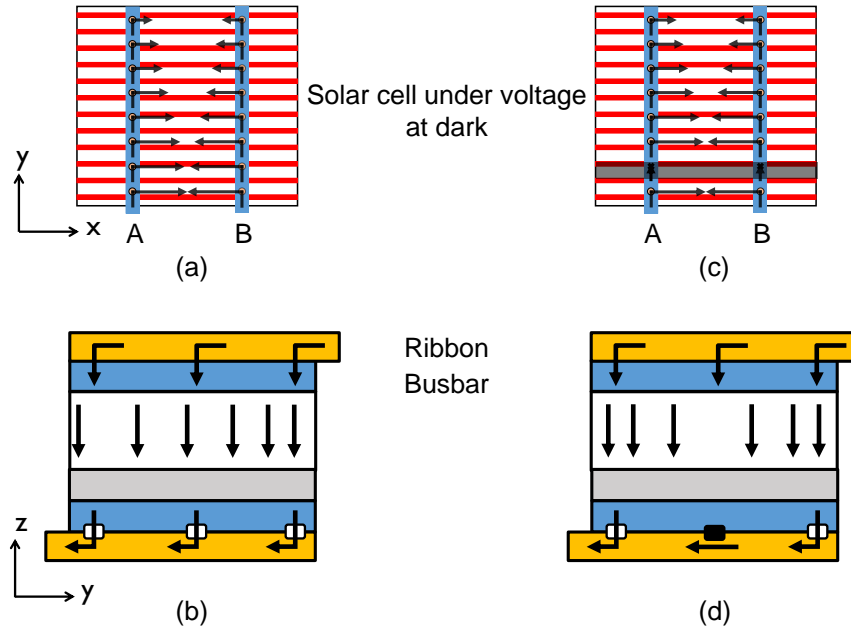


Fig. 6.2. (a) Top view of a typical solar cell with the ribbons connected to the busbar through eight solder bonds. (b) Side view of the pristine module showing current transfer pathways from the ribbon to the busbar, through healthy solder bonds (white boxes). (c) Top view of a solar cell with a broken tabbing point and corresponding redistribution of current. (d) Side view of modified current transfer pathways between the ribbon and the busbar. Current cannot go through the broken bond, hence more current will go through the remaining healthy bonds. Localized failure within the backside solder pads is governed by the same principle and therefore leads to a similar current redistribution.

offering lower resistance to the current flow. The size of the arrows in Fig. 6.2 2a reduces because the voltage drops over the series resistance of the parallel combination of ribbons and busbars that in turn reduces the available forward bias of the diode further away from the injection points. Fig. 6.3 validates this interpretation by cell level numerical simulator called GriddlerTM [162]. As an aside, note that our simulation uses solder bonds as the discrete contact points for current transfer between the busbars and ribbons. Modern cells sometimes use continuous soldering (instead of discrete bonds) on the front and multi-segment solder pads at the backside of the

cell. In that case, this simulation framework can be used for analyzing the first design directly and as a discrete approximation of the second design.

When a solder bond is missing due to manufacturing error or is broken due to stress [191], the current flow pattern changes significantly, see Fig. 6.2. The current flowing through the ribbon cannot transfer to the corresponding point of the busbar due to higher resistance associated with the broken solder bond. Instead, the current continues to flow along the ribbon until it reaches the next healthy solder bond and transfers to the busbar. Therefore, the healthy solder bonds and the adjacent silicon diodes close to these bonds will carry higher current levels. Such current crowding spatially redistributes the local power dissipation.

Once again we used the numerical simulator GriddlerTM [162] to confirm the hypothesis. We simulated a number of cells in which alternate solder bonds are broken. The simulation parameters that were used for a typical c-Si cell with an efficiency of 18.7% are summarized in Table 6.1. The results in Fig. 6.3 demonstrate less power dissipation close to the broken bonds and more dissipation causing hotspots in the vicinity of the adjacent healthy bonds.

6.3 Theory and Simulation: Hot Spot Formation around Broken solder bonds

The discussion above suggests that a completely broken solder bond will be surrounded by a region with redistributed power dissipation, i.e. an asymmetric doublet of hot or cold spots. In practice, the solder bonds degrade over time due to periodic mechanical stress, and the resistance of the pathway increases gradually until failure. In this section, we wish to examine this gradual increase in the solder bond resistance carefully, because the DLIT experiments are likely to involve solder bonds at different stages of degradation.

Unfortunately, GriddlerTM does not allow gradual degradation of solder bonds. Therefore, to examine the position of dissipated power when the solder bonds degrade

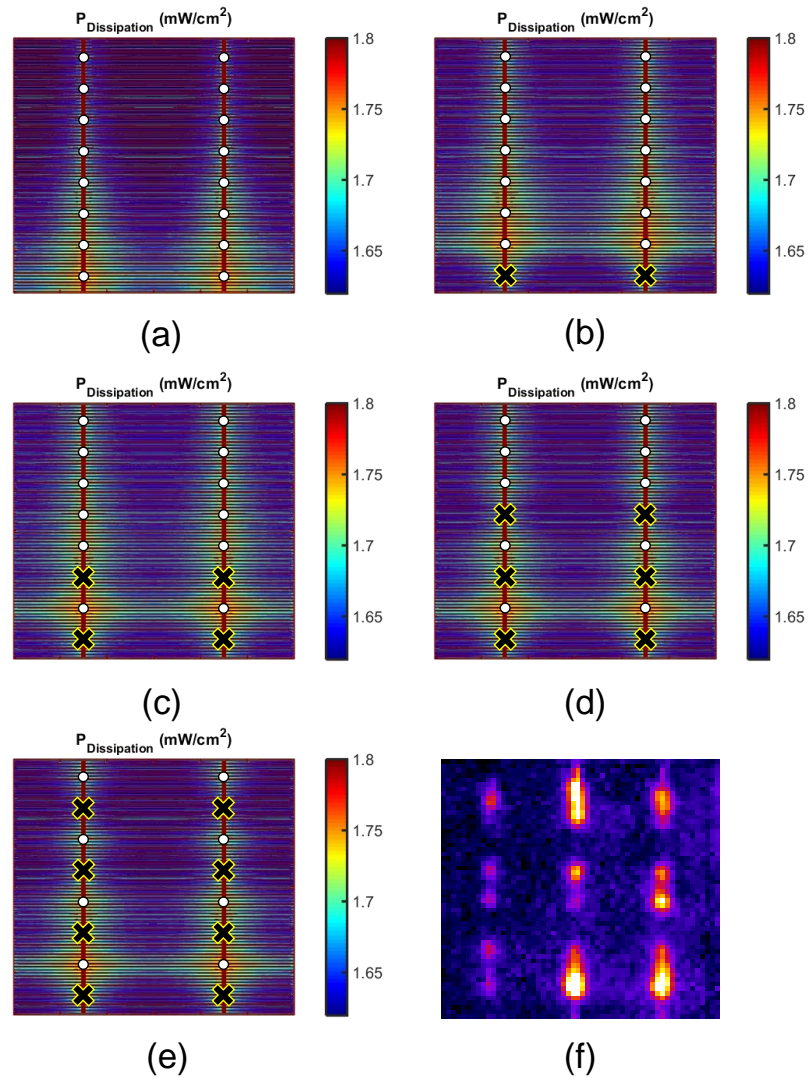


Fig. 6.3. Power dissipation map of solar cells with (a) zero, (b) one, (c) two, (d) three, and (e) four alternating broken solder bond(s) on each ribbon. The black crosses show the broken bonds and the white dots show the healthy ones. It is possible to pinpoint the broken tabs. Because more current goes through the healthy tabs and they become hotter (hotspots). (f) Measured DLIT image indicating the regions closer to current injection points at the bottom solder-pads contain characteristic asymmetric doublet hotspots.

over time, we have simulated the structure using the HSPICE circuit simulator with the terminal I-V characteristics of the pristine cell calibrated to experimental values

Table 6.1.
Baseline Simulation Parameters for Cells in Griddler

Property	Value
Finger sheet resistance	3 $m\Omega/sq$
Busbar sheet resistance	3 $m\Omega/sq$
Finger contact resistance	0 $m\Omega/sq$
Layer sheet resistance	80 Ω/sq
Wafer internal series resistance	0 $m\Omega.cm^2$
Internal shunt conductance	0 $1/(\Omega.cm^2)$
Ribbon width	1 mm
Ribbon sheet resistance	0.1 $m\Omega/sq$
Contact point resistance	0 $m\Omega$
Number of tabbing points on ribbon	8
1-sun J_{ph} , non-shaded area	39.6 mA/cm^2
J_{01} , passivated area	200 fA/cm^2
J_{01} , metal contact	600 fA/cm^2
J_{02} , passivated area	10 nA/cm^2
J_{02} , metal contact	50 nA/cm^2
Finger pitch	1.9 mm
Finger width	60 μm
Number of fingers	82
Busbar width	1.5 mm
Number of busbars	2
Cell area	243.36 cm^2
Front illumination	0 $Suns$

discussed in section VI. Since the solar cell is symmetric, we have simulated half of the cell. The baseline input parameters of the simulation are shown in Table 6.2 and the circuit schematic is shown in Fig. 6.4a. The resistance of each part of the ribbon (busbar) connecting two solder bonds is lumped into one resistance as $R_{rib_i}(R_{bus_i})$.

Table 6.2.
Baseline Simulation Parameters for the Cell simulated in HSPICE

Property	Value
Busbar resistance, R_{bus}	3.8 $m\Omega$
Ribbon resistance, R_{rib}	1.9 $m\Omega$
Solder bond resistance, R_{rib}	0.1 $m\Omega$
Current source	0.4 A
Diode saturation current, I_{01}	19.5 pA
Shunt resistance, R_{sh}	10 $k\Omega$
Series resistance including finger resistance, R_S	0.3 $m\Omega$

The numerical simulation results in Fig. 6.4b-d show the gradual change in the power dissipation for $R_{SB2} = 0.1m\Omega$ (Pristine), $2.5m\Omega$ (Half-broken), 1Ω (Fully broken). We have compared the relative change in the power dissipation of sub-cells, ribbons, and busbars (See Fig. 6.4e) in pristine and fully broken bond conditions. Two adjacent ribbons and busbars to the broken solder bond show a notable change, however, there is no significant relative change in power dissipation of the sub-cells. Since the diodes are already turned on by the current there is not a significant change in the voltage on diodes with a change in the current passing through the diodes. Hence the small change in the sub-cell power is expected.

To understand the origin of hot spots in DLIT images, we need to quantify the spatially-resolved self-heating in the ribbons. The spatially-resolved power dissipation in Fig. 6.4b-d shows that breaking solder bond #2 (R_{SB2}) reduces power dissipation

in the preceding section of the ribbon (#2) and increases the power dissipation in the following section of the ribbon (#3). The rest of the ribbon-segments (#4 to #8) do not have a significant change in their power dissipation. The opposite profile is obtained for the busbar, i.e. power dissipation is increased in the preceding section of the busbar (#2), while power dissipation is reduced in the following section of the busbar (#3).

The redistribution of the ribbon and busbar currents, in turn, may lead to spatially-correlated self-heating and degradation of the neighboring solder bonds. Since solder bond #2 (R_{SB2}) is broken, the current cannot go through it. Instead, the current has to find a new path with lower resistances. Most of the current previously going through R_{SB2} will now flow through R_{SB3} . As a result, the power dissipation is reduced in segment #3 of the busbar. In contrast, current flow through R_{SB1} is now enhanced, leading to an increase in Joule-heating of segment #2 of the busbar (R_{bus2}). Since more current is going through R_{SB3} , the solder bond following the broken one, R_{SB3} heats more and is prone to degradation. Hence solder bonds adjacent to the broken one are represented by a cluster of hot spots within a cell (see Fig. 6.6a). We will see later that this clustering of solder bond failures is indeed observed in experiments.

So far, we have explained through simulation how the magnitude and the position of the power dissipation evolve as a solder bond gradually degrades over time. In the next section, we will experimentally determine the number of hotspots and their correlation with series resistance using DLIT imaging. Although the simulation focused on the failure of solder bonds on the front side, the module analyzed uses continuous soldering on the front side and three solder pads on the backside of the cell. Therefore, the simulation results discussed above should be interpreted as a discrete approximation of the solder bond hot-spot formation. In this perspective, gradual localized degradation of the solder pad in the experimental modules is equivalently represented by a discrete solder bond failure of the simulation results.

6.4 Experimental Validation

A total of 23 modules have been examined from the same manufacturer that have been installed in the field for two years. The modules have 72 multi c-Si solar cells and their initial output power was 310W. As shown in Fig. 6.5(a), the modules have substantial power loss with outputs in the 200-280W range. The fill factor (FF) decreased more significantly compared to other characteristics such as Fig. 6.5b-c which were previously presented in [17] and are reproduced here for the ease of reference), indicating signs of series resistance degradation as discussed in [17]. For example, the FF of one severely degraded module drops from the nominal value of 0.76 to 0.51. Since changing less than 2% compared to their pristine values, it is indeed the FF-loss associated with increase that causes the loss of almost one third of initial output power i.e. $((0.76 - 0.51)/0.76)$. The I-V curves under illumination have been fitted using a five-parameter double-diode model to extract the series resistance. As shown in Fig. 5(d), we find that the series resistance increase is exclusively correlated to the power loss.

Asadpour et al. [147] have recently shown that module-level series resistance degradation is directly correlated to solder bond/solder-pad degradation, assuming that there is no degradation of the internal circuitry. In contrast, the degradation of the metallic fingers through corrosion or delamination appears only as a “fake shunt” in the terminal I-V characteristics but does not increase the series resistance. We analyzed the module using a variety of luminescence imaging techniques such as EL, PL, and DLIT to confirm the physical cause of series resistance degradation [192]. Although EL imaging has been used to detect solder bond failure or measuring series resistance [193–195], DLIT has been used less frequently for such purposes. DLIT allows one to observe the redistribution of power dissipation due to solder bond failure because it maps the related change of the thermal dissipation in the ribbons. We will see later that the DLIT results are indeed well correlated to the series resistance of the module.

To pinpoint the hotspots with DLIT, our collaborators at NREL applied a forward bias current of 8.8 A pulsed in a square wave with a 50 % duty cycle at 1 Hz to the terminals of the modules. The camera is referenced to the same frequency, and this lock-in method allows us to record the heat dissipation that is dependent on the applied current stimulus while effectively subtracting out the steady-state background heat. The camera for DLIT is a FLIR SC5600-M (formerly Cedip Silver 660M) InSb camera with 640×512 pixels. The pulse bias was applied using Kepco BOP 100-100MG power supplies triggered by a Tektronix AFG3102 dual-channel function generator.

We quantified the number and area of hotspots by thresholding the images and processing an image mask. Fig. 6.6 shows a severely degraded module and a mildly degraded module along with the hotspots above the threshold. We note that the hotspots are localized within the region defined by the busbar/ribbons and solder pads on the backside of the cell, confirming that the degradation is associated with these components. The stress causes the solder bonds on the front or back-side pads to degrade over time, thereby increasing the resistance for the current in the ribbons to be transferred to the busbars. As explained in Fig. 6.4, the current-crowding associated within the neighboring healthy bonds leads to the hot spot formation. EL and PL images are shown in Fig. 6 are consistent with the current redistribution mechanism. The EL images collected at forward-bias equivalent to I_{SC} show brighter EL regions coincident with hotspots from DLIT. Although, there are cracks in both modules the cracking does not correlate with the module power loss. This was shown in [192], where UV fluorescence images were used to show that cracking is not the main cause of power loss. Moreover, cracked cells are in a different location compared to those showing solder-related hotspots. Therefore, the cracks are not responsible for the DLIT pattern that correlates with the module power loss.

To verify the source of degradation, the five-parameter model fitting of measured I-V curves was used to extract the series resistance of modules. As shown in Fig. 6.5,

the number of hotspots and series resistance are strongly correlated. Such correlation validates the hypothesis of series resistance increase due to the failed solder bonds.

This validation confirms that it is possible to use the I-V measurements to detect the solder bond failure and get an estimate of the number of broken bonds based on the increase in the series resistance compared to its pristine value. However, if one desires the spatial distribution of the healthy and broken bonds and the evolution of degraded bonds over time, DLIT imaging provides the additional information needed. Interestingly, the modules examined had a significant decrease in the output power (and significant increase of the series resistance) after only two years in the field. This analysis demonstrates the importance of high-quality solder bonds or solder pads for highly reliable solar modules.

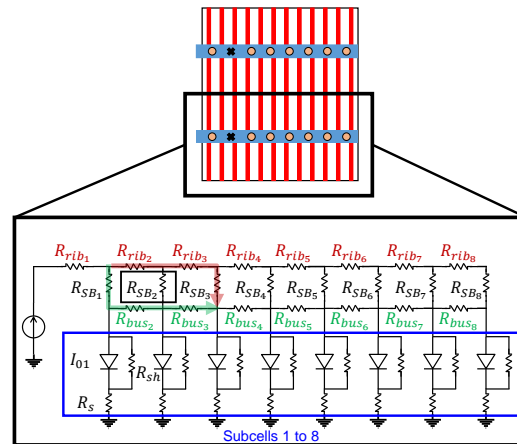
Although DLIT imaging in this case was performed indoors, we note that there is wide interest in adapting such diagnostic methods for outdoor use without dismounting modules. Indeed, steady-state EL imaging and fly-over thermal imaging are used in field installations [196, 197]. However, steady-state thermal imaging does not produce the high resolution that we obtain using a scientific grade lock-in thermal camera. Implementing lock-in detection in the field is not unprecedented, where daylight background can be subtracted from EL or PL images by lock-in modulation of the current injection or extraction in the module [198, 199]. Furthermore, illuminated lock-in thermography (ILIT) could be implemented outdoors without accessing the electrical contacts of the module, where a pulsed light excitation modulates the injection level [200]. Indeed, a portable ILIT setup has been demonstrated that works similarly to outdoor “contactless EL” imaging [200]. There is also great promise for decreasing the cost of outdoor-compatible ILIT or DLIT systems to make them more accessible to module owners: An inexpensive proof-of-concept pricing less than \$1K has been demonstrated for thermal imaging of mechanical defects and dental caries using a cellphone-attachment microbolometer thermal detector with custom lock-in acquisition code [201]. These examples highlight the future possibility of high-resolution

outdoor thermal imaging to identify metallization failures such as current crowding at partial solder bond degradation as occurred in the modules we studied here.

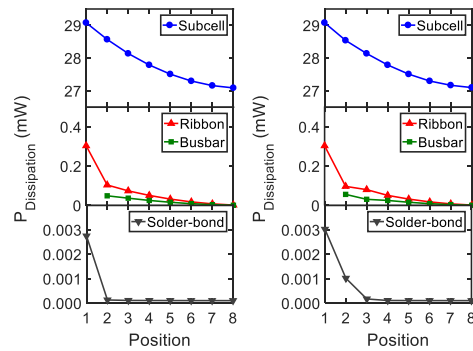
6.5 Summary and Conclusions

In this chapter, DLIT experiments have been used in conjunction with cell-level simulations of power dissipation to evaluate the causes of increased series resistance in PV modules after two years of field operation. The results demonstrate that the solder bond failure is uniquely correlated to increased series resistance and corresponding loss of output power. We reached this conclusion by extracting the series resistance out of I-V measurement and counting the hotspots from DLIT images. This correlation confirms that the solder bond failure can be determined in situ by monitoring the series resistance increase of a fielded module, complemented by periodic validation offered by the lab-scale DLIT tests. Furthermore, the simulations of current redistribution pathways highlight a characteristic hot/cold dyad pattern that arises in DLIT images due to the current-crowding mechanism at partially broken solder joints.

In the future, if one can further correlate the solder bond failure exclusively to an accelerated standard test, we will have made significant progress toward finding the root cause leading to loss of power degradation based on solar farm data. To further explore this possibility, in the next chapter we will propose a physics-based and a probabilistic model that predicts the output power of c-Si solar panels that suffers from solder bond failure.

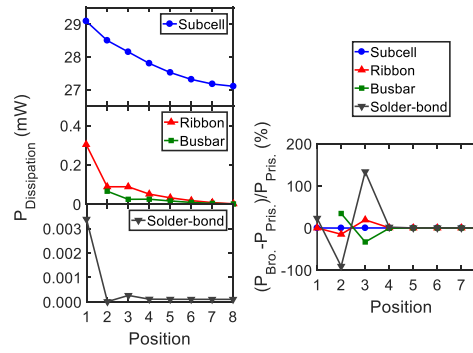


(a)



(b)

(c)



(d)

(e)

Fig. 6.4. (a) Schematic solar cell and zoomed in elements of the half-cell simulated in HSPICE. Sub-cells include the silicon (semiconductor) part and finger resistance. (b) Power dissipation in different parts of the cell in (b) Pristine, (c) Half-broken, and (d) Fully broken condition of second solder bond (R_{SB_2}). (e) Relative change in power dissipation before and after the second solder bond breaks. Only adjacent metallic parts show a significant change.

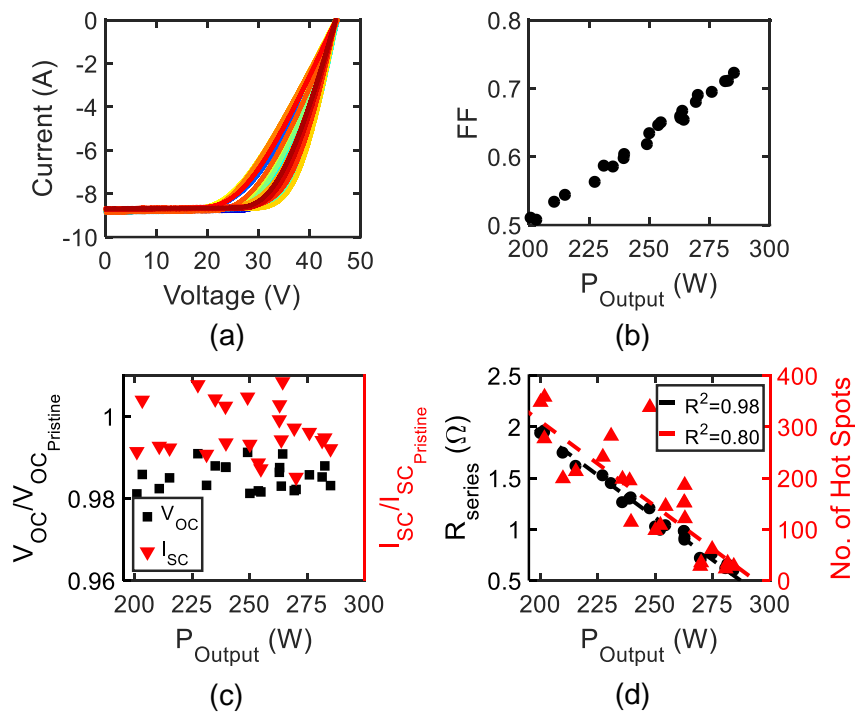


Fig. 6.5. There is a strong correlation between power loss, series resistance, and number of hot spots increase in the experimental set. If the internal circuitry has degraded the root cause can only be series resistance increase due to solder bond failure.

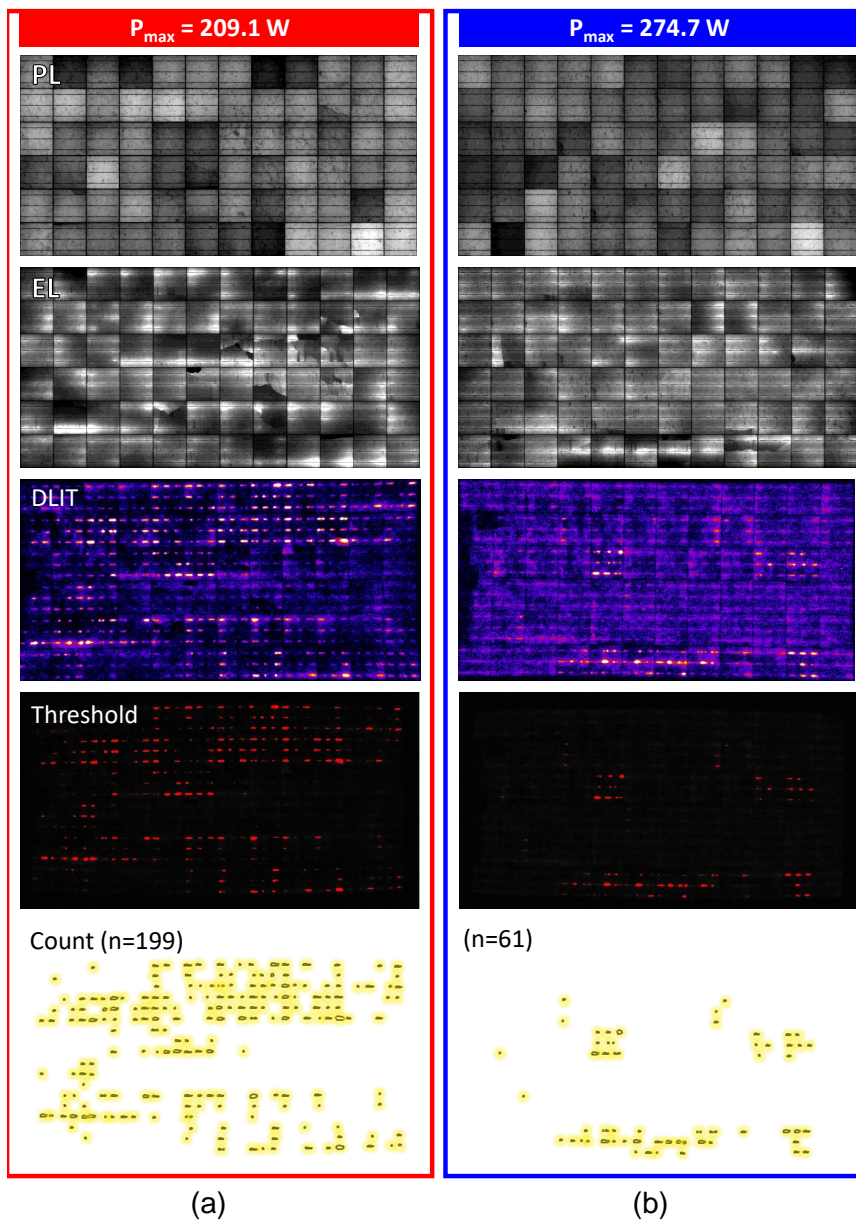


Fig. 6.6. Severely degraded module (a) and mildly degraded module (b). DLIT images show severely degraded modules have more hot spots validating that more broken bonds cause more hotspots and more power loss.

7. A PHYSICS-BASED AND PROBABILISTIC MODEL THAT PREDICTS THE SOLDER BOND FAILURE IN C-SI SOLAR PANELS

Note: The material in this chapter has been adapted from Ref. [202]

Predicting the time-dependent performance degradation of the PV modules installed in a solar farm, based exclusively on the location-specific weather conditions and predetermined degradation parameters obtained from accelerated tests, has been a long-term goal of the research community. Recently, several groups have developed statistical techniques to analyze, train, and then predict the time-dependent efficiency degradation of the solar modules. Although these techniques show promising results, the non-linear time-dependence and coupling among various degradation modes make it unlikely the statistical models can be predictive. Indeed, for accurate prediction, these statistical models must be guided by physics-based degradation models. Sun et al. have demonstrated the promise of these physics-guided forward and inverse models to predict the performance of the solar cells [181]. An important degradation mechanism missing in Ref. [181] is the failure of solder bonds due to the mechanical stress caused by the daily and seasonal fluctuations in the ambient temperature. In this chapter, we will develop a physics-based model that predicts the electro-mechanical performance of a solar module with solder bond failure as the dominant degradation mechanism. This degradation model will serve as a building-block of an integrated reliability model that can predict the performance of a module simultaneously subjected to several degradation mechanisms.

7.1 Introduction

As a part of a standardized qualification protocol, many accelerated tests assess the long-term reliability of various solar module technologies. Each test is expected to isolate and accelerate specific pathways for module degradation. For example damp heat test quantifies the impact of extreme ambient temperature and humidity on the module performance [167, 173, 203–205]. By stressing a module at high voltage, one can quantify its vulnerability to potential induced degradation (PID) [175, 206–216]. Similarly, thermal cycling (TC) assesses the reliability of a module subject to daily and seasonal cyclic change of temperature [217–223]. The cyclic contraction and expansion of different parts of the module (with dissimilar coefficient of thermal expansion, CTE) creates significant shear stress at various interfaces. In particular, metallic-silicon interface and solder bonds are prone to stress-induced degradation due to their rigid and non-conformal topology. In a typical module, these metallic components include front ribbon made of copper, front solder bonds/pads, silver contacts (fingers and busbars), rear aluminum contacts, rear solder, rear ribbon made of copper, and other inter-module connections [222]. The degradation of various interfaces imprints their characteristic signature on the J-V curve of the module. As discussed in chapter 6, solder bond failure manifests itself as an increase in series resistance, characterized by the reduced slope close to V_{OC} of the module. There have been several efforts to model the lifetime of a module that degrades exclusively due to solder bond failure. For example, Jiang et al. have used numerical simulation based on the finite element method (FEM) to define the fatigue-limited lifetime as a power-law of the average ambient temperature [221]. However, the analysis did not account for the cyclic variation of temperature that causes the stress to begin with [223]. Jabarullah et al. also started from a FEM method and found the fatigue damage is correlated to the number of thermal cycles (temperature variation) that the cell is subjected to. They also used the Monte Carlo simulation to find the damage distribution and finally fit

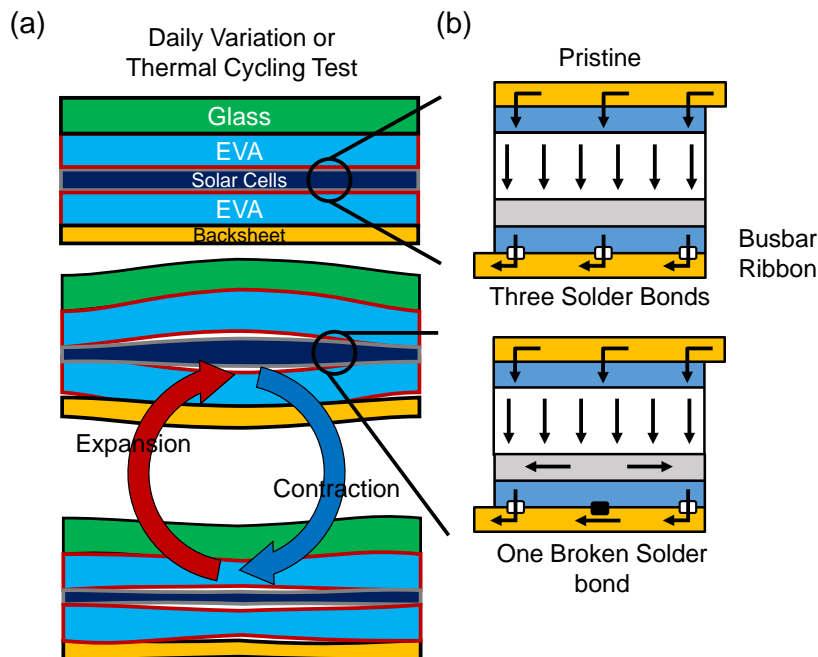


Fig. 7.1. (a) The temperature variation causes the module to expand and contract. (b) Initial and degraded cell with one broken bond.

the data to extract the solder bond lifetime [222]. The methodology, however, does not provide a compact model or analytical formulation suitable for inverse modeling.

In this chapter, we will show that a physics-based model can predict the time-dependent efficiency degradation of a c-Si solar module subject to solder bond failure. We will see that the rate of solder bond failure depends on ambient temperature, incident light, wind speed, etc. In addition, We will use the Markov technique to account for the statistical distribution of the failure time distribution. Given the ambient operating conditions, this powerful physics-based model will predict the cumulative degradation of a module at any location of the world. We start by discussing the work of Bosco et al. [191] that correlates the accumulated stress in a module to the ambient temperature and the material properties of the solder bonds. Second, we presume that the number of broken solder bonds in a cell/module is linearly correlated to the accumulated stress. Finally, We can use the solar-cell simulator GriddlerTM [162] to

find the degraded J-V characteristics associated with the number of broken solder bonds. Since we already know how the temperature variation affects the solder bonds as a function of time, GriddlerTM results can be used to predict the evolution of the performance at the cell level over the course of time. Eventually, the cells must be connected in series to create a module. Due to the probabilistic nature of the solder bond failure in different cells across the module, we will need to use the Markov chain model to predict the efficiency degradation of a fielded module. We will end the chapter by summarizing the key conclusions.

7.2 Theory and Simulation Framework

7.2.1 An Overview of the Theoretical Framework

There are three components of the phenomenological model of the series-resistance increase due to solder bond failure: (a) Stress accumulation due to temperature cycling, (b) breaking of the solder bond once critical stress has been accumulated, and (c) the effect the broken solder bonds have on the I-V characteristics of the solar cell.

We recall that the stress accumulated in the cell/module is due to temperature variation that causes contraction and expansion as shown in Fig. 7.1. Eq. 7.1 [191] shows semi-empirically how the variation of the temperature relates to the accumulated stress-induced damage in the modules.

$$D = C(\Delta T)^n (r(T))^b \exp\left(-\frac{Q}{k_B T_{\max}}\right) \quad (7.1)$$

where ΔT is the average module temperature, T_{\max} the daily maximum module temperature, C is a scaling constant (here: 239.9), Q is the activation energy of the solder material (here: 0.19 eV), and k_B is the Boltzmann constant. Here, $r(T)$ is the number of times that the temperature crosses the reversal temperature $T = 56.4^\circ C$ over the course of time. The parameters including $b = 0.33$ and $n = 1.9$ that are used in our simulation are taken from Ref. [191].

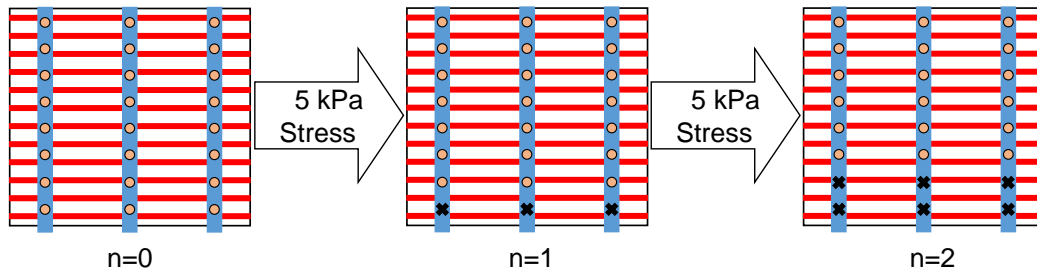


Fig. 7.2. Top view of a cell with three busbars and eight solder bonds on each busbar. Horizontal red lines show fingers while vertical blue lines show busbars. The healthy solder bonds are shown as circles and broken ones are the black crosses. One row of solder bonds breaks when the module/cell is exposed to $5kPa$ of accumulated damage.

Once we have calculated the time-integrated accumulated stress in a module due to temperature-fluctuation, next we must correlate this stress to the number of broken solder bonds within the module. For simplicity, we assume a linear relationship between the accumulated stress and the number of broken bonds. Specifically, we assume that the successive accumulation of 5 kPa stress leads to the failure of a row of solder bonds, see Fig. 7.2. For simplicity, we neglect any stress relaxation due to the failure of the solder bonds. As the third and final part of the model, we correlated the number of broken bonds in a module and the corresponding increase in the series resistance. Taken together, these three components relate the ambient temperature fluctuation to the degradation of the series resistance of a solar module. We will discuss these effects in more detail in the following section.

7.2.2 Step 1: Module Temperature Fluctuation Determines the Accumulated Stress on the Solder Bonds

The first step of finding the accumulated damage is to find the module temperature. We used self-consistent model from [224] as shown in Eq. 7.2

$$T(t) = T_a(t) + c_T I(t) \left(\frac{\tau\alpha}{u_L} \right) \left(1 - \frac{\eta_0(t)}{\tau\alpha} \right) \quad (7.2)$$

where T_a in $^{\circ}C$ is the ambient temperature, $c_T \sim 1$ is a correction for daily averaged temperature, I is the time-dependent irradiance, $\tau \sim 0.95$ is the transmittance of glazing, α the absorbed fraction (here: 0.8), u_L is the heat loss coefficient with the value of 21.5 in $m^2 \cdot ^{\circ}C/W$, and η_0 is the initial efficiency of the module. The efficiency η_0 itself depends on temperature with temperature-coefficient,

$$\eta_0 = \eta_{nom}(1 - \beta_P (T(t) - 25)) \quad (7.3)$$

where η_{nom} is the nominal efficiency of the module and $\beta_P = 0.41\% / ^{\circ}C$ is the temperature coefficient of efficiency. Therefore, we must self-consistently solve Eqs. 7.3 and 7.2 to determine the module temperature, as shown in Fig. 7.3a).

As an aside, the ambient temperature-series is sometimes reported in very short time intervals (e.g. 1 minute). Given the thermal mass, a module cannot follow such a rapid thermal variation. Instead, the temperature is defined by an exponentially weighted moving average (EWMA) as described in Ref. [191], see Eq. 7.4

$$(T_{module})_t = (T_{module})_{t-1} \alpha + (T_{cell})_t (1 - \alpha) \quad (7.4)$$

where $\alpha = 0.8$ is the EWMA gain parameter.

Once the module temperature is calculated, we can determine the number of reversal temperature crossing assuming the threshold is $T = 56.4^{\circ}C$ as shown in Fig. 7.3b. The weather data and the reversal temperature both start mid-April and continue until November. The reversal crossing stops in early October since the module temperature does not reach $56.4^{\circ}C$. Finally, we use the quantities obtained in Eq. 7.1 to calculate the accumulated damage for the given technology and local weather condition.

7.2.3 Step 2: Accumulated Damage and Broken Solder Bonds

Solder bond breakage is a statistical event terminated by a threshold. In other words, as the damage/defects accumulate, some solder bonds will reach the critical

stress necessary for the breakage before others do. As a result, there will be a sequential solder bond dissociation with accumulated damage. We can and will describe this statistical nature of solder bond dissociation by a Markov Chain model later in the Chapter. Here we take an alternate (and simplified) perspective that on-average a row of solder bonds break for every 5 kPa (to be calibrated against experiment) of accumulated stress. This simplified relationship allows us to calculate the number of broken bonds as a function of time as shown in Fig. 7.3c. Recall that the initial time zero corresponds to mid April for Fig. 7.3a,b. Due to the non-linear dependence of stress and temperature reversal, the stress increases very rapidly for the pristine module, with the corresponding rise in the solder bond failures. After the first few weeks, with a few bonds already broken, the subsequent damage-accumulation is reduced and bond-breaking slows. The Markov Chain model will show that the presumed linearity between accumulated defects and the solder bond failure is inaccurate. After all, all the solder bonds are experiencing damage at the same time. Once one solder bond fails because it reaches the critical stress, the other solder bonds are also primed for failure and the subsequent failures in other bonds come in quick succession. In a simplified model, we can describe this effect by a nonlinear dependence of solder bond failure on the accumulated stress, a topic we will return to later.

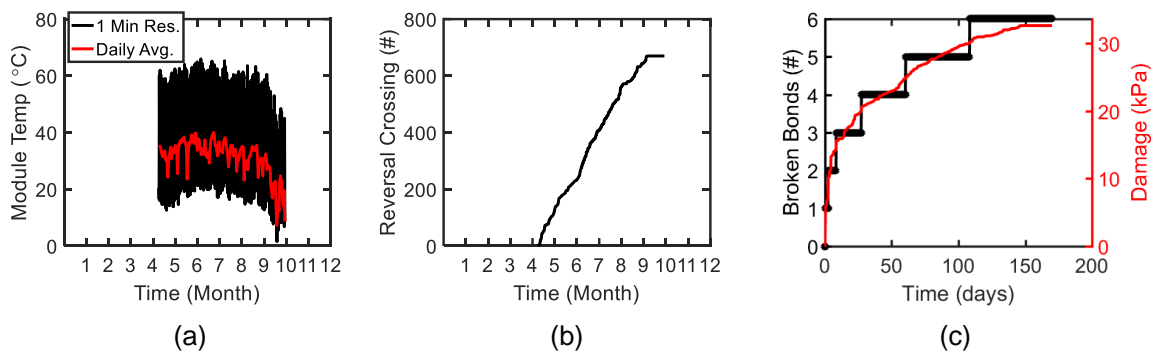


Fig. 7.3. (a) Module temperature and (b) reversal temperature crossing as a function of time from April to November. (c) Accumulated damage (red line) and the number of broken solder bonds (black circles) as a function of time starting at time zero.

7.2.4 Step 3: Broken Solder Bonds and Increasing Series Resistance

Finally, we can use GriddlerTM to calculate the cell level degradation of the J-V characteristics in response to a different number of broken bonds as shown in Fig. 7.4a. The baseline parameters used for the simulated cell are shown in Table 7.1. The non-linear dependence of the efficiency and number of broken bonds is shown in Fig. 7.4b by extracting the characteristics from the J-V curves. Once the solder bond failure exceeds 6 or 7 rows, the local current needs to travel a long distance before being collected by the remaining "healthy" solder bond. Naturally, numerical convergence becomes difficult. However, the module degrades more than 20% of its power long before this extreme scenario, allowing us to explore the essential consequence of solder bond failure regarding the power degradation of a solar module.

Fig. 7.4c shows efficiency as a function of time and it has discrete steps in time reflecting the abrupt breaking of a solder bond. In practice, the accumulated damage would increase the resistance even before the solder bond breaking. However, our previous work has shown that the resistance change in damaged but unbroken bonds is small compared to completely-broken solder bonds. This presumption is verified by the observation that even though a module has more than 1500 solder bonds, the discrete change of efficiency due to solder bond failure is still observed at the module level. In order to use the Eq. 7.1 in a compact model form, we need to find the relationship between the number of broken bonds and series resistance. Since we have the J-V curves we extract the series resistance and put it in a lookup table (see Table 7.2). Then using Eq. 7.5 it is possible to calculate the series resistance that can be used in a five-parameter compact model as shown in 5.1. We assume that the number of broken bonds cannot include fractions, However, we can interpolate between the series resistance values to account for gradual solder bond failure. Fig. 7.5 shows how the series resistance degrades as the number of broken bonds increases as well as the series resistance as a function of time.

Table 7.1.
Baseline Simulation Parameters for Cells in Griddler

Property	Value
Finger sheet resistance	3 $m\Omega/sq$
Busbar sheet resistance	3 $m\Omega/sq$
Finger contact resistance	0 $m\Omega/sq$
Layer sheet resistance	80 Ω/sq
Wafer internal series resistance	0 $m\Omega.cm^2$
Internal shunt conductance	0 $1/(\Omega.cm^2)$
Ribbon width	1 mm
Ribbon sheet resistance	0.1 $m\Omega/sq$
Contact point resistance	0 $m\Omega$
Number of tabbing points on ribbon	8
1-sun J_{ph} , non-shaded area	39.6 mA/cm^2
J_{01} , passivated area	200 fA/cm^2
J_{01} , metal contact	600 fA/cm^2
J_{02} , passivated area	10 nA/cm^2
J_{02} , metal contact	50 nA/cm^2
Finger pitch	1.9 mm
Finger width	60 μm
Number of fingers	82
Busbar width	1.5 mm
Number of busbars	3
Cell area	243.36 cm^2
Front illumination	1 $Suns$

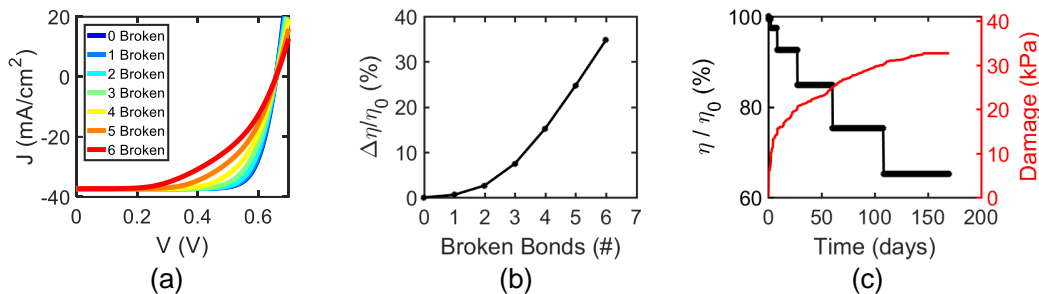


Fig. 7.4. (a) J-V curve of a cell with a different number of broken bonds, (b) non-linear dependence of normalized efficiency as a function of the number of broken bonds, and (c) normalized efficiency (black circles) and accumulated damage (red line) as a function of time.

$$R_S = R_{S_0} + \Delta R_S(n) \quad (7.5)$$

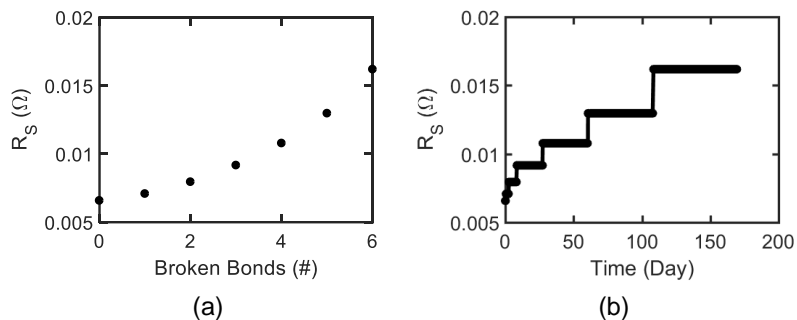


Fig. 7.5. (a) series resistance as a function of the number of broken bonds. (b) Increasing series resistance as a function of time.

For future work, we will calibrate the relation of stress and the number of broken bonds using literature data. We will use the data from Ref. [220] that measured the I-V curves at a different number of cycles. Then fit the pristine I-V data using GriddlerTM simulator at cell level then, put the cells in series to match the module level extracted I-V. The next step is to break solder bonds in a consecutive manner in the cell simulator to match the series resistance of the measured module I-V. Then

Table 7.2.
Number of Broken Bonds vs. Change in Series Resistance Lookup Table

Number of broken bonds (n)	$\Delta R_S(n)$ ($m\Omega$)
0	0.00
1	0.50
2	1.40
3	2.60
4	4.20
5	6.40
6	9.60

we can find the minimum number of broken bonds needed for the measured series resistance. We then correlate the number of broken bonds to the accumulated stress calculated by Eq. 7.1.

7.3 Statistical Distribution of Solder Bond Failure at Module Level

The presumption that bonds break linearly with accumulated stress is reasonable, but potentially inaccurate. After all, the breakage of the solder bonds is a statistical phenomenon. Although the stress is accumulated inside the module the location of exact breakage i.e. which cell is going to suffer the failure is not known and successive failures occur at an accelerated rate.

7.3.1 A Markov Chain Model for Solder Bond Failure

A rigorous analysis of solder bond failure distribution can be derived from the Markov chain approach and is summarized in Eq. 7.6. This equation was originally developed to describe an analogous problem of soft-breakdown in gate dielectrics [225].

$$P_n(\chi, \xi) = \left[\prod_{m=0}^{n-1} (1 + m\xi) \right] \left(\frac{1 - e^{-(\xi\chi)}}{\xi\chi} \right)^n \frac{\chi^n e^{-\chi}}{n!} \quad (7.6)$$

where P_n is the probability of a cell with n broken solder bonds, as shown in Fig. 7.2. In other words, $P_n = N_n/N$ where N is total number of cells in the module and N_n is the number of cells with n rows of broken bonds, and $\chi = (t/\eta)^\beta$ is the normalized time-variable to η that is the mean-time to the first breakage of the solder bonds. Here, β is location-specific time-exponent for the accumulated damage shown by the red-line in Fig. 7.3(c), and ξ is the correlation factor that accounts for stress-concentration and subsequent acceleration of defect generation in the remaining solder bonds. For simplicity, we assume that the solder bonds on the same row break together. Therefore, it can be treated as a worst-case scenario.

Overall, the Markov chain model allows us to calculate the number of broken solder bonds within each cell of a module as a function of stress time. Since we already simulated the I-V curves of the cells having a different number of broken bonds, we put these cells in series and reconstruct/predict the I-V curve related to any state of solder bond failure within the module.

The simulation does not account for the gradual process of solder bond failure. This level of detail can be added once the initial model has been verified by adding more simulations that include the semi-broken bonds. We have used $\xi = 0.1$ (weak correlation), $\eta = 5000$ hour, and total time = 40000 hour ~ 4.5 year. As shown in Fig. 7.6 number of healthy cells (with none of the bonds broken) decreases in time. First, there is a rise of cells with a single row of broken bonds, however, as cells begin to develop the second and third broken solder bonds, the number of cells with only one row of broken bonds decline. The process continues until the output power drops below 80% of initial power.

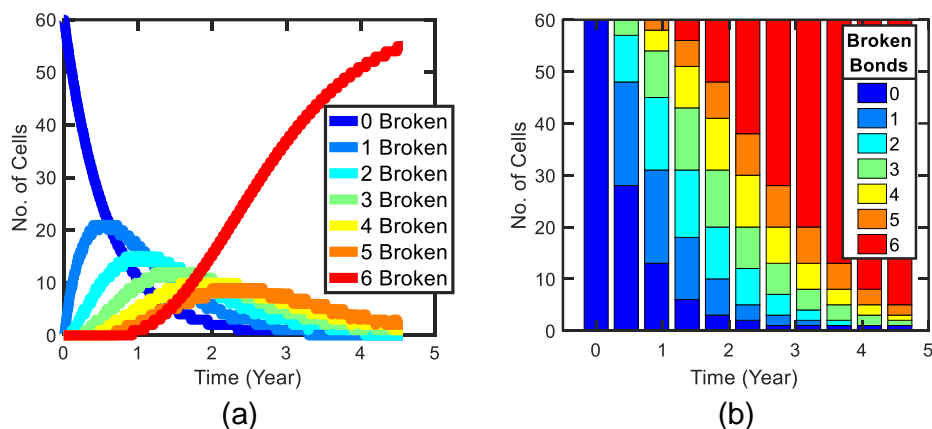


Fig. 7.6. (a) Distribution of the number of cells with n rows of broken bonds N_n . (b) Distribution of the number of cells with n rows of broken bonds N_n at ten different points in time in bar plot for easier visualization.

7.3.2 Results and Discussion

Having the distribution of the number of broken bonds, the next step is to put these cells in series to reconstruct the J-V curve at module level (see Fig. 7.7). The efficiency of the module plateaus to $\sim 12.7\%$ as shown in Fig. 7.7b. If we zoom in

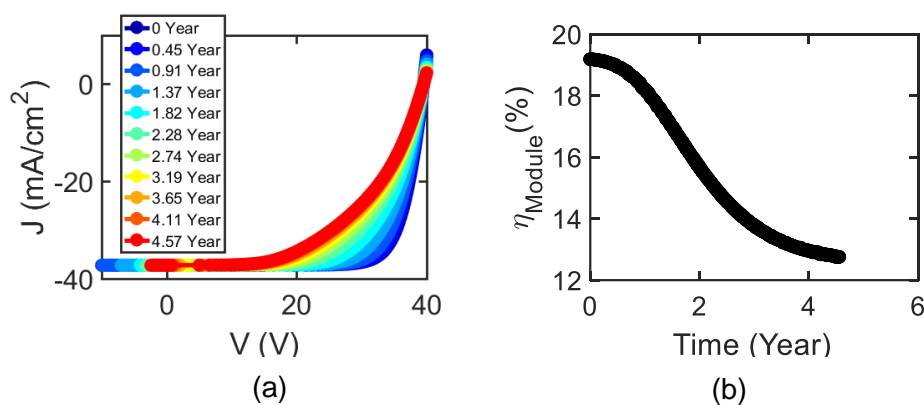


Fig. 7.7. (a) J-V curve of a module undergoing solder bond failure at different times. (b) The efficiency of the module as a function of time saturates close to the end.

the results, we will see that the efficiency drops in steps with successive failure of solder bonds fail (see Fig. 7.8a). Such a drop is expected as shown in measured data provided by Sandia National Lab of a string of 13 modules that have 60 multi c-Si cells (see Fig. 7.8b). The efficiency data was extracted by the Suns-Vmp method developed by Sun et al. [181]. The duration of the measured data is ~ 150 days.

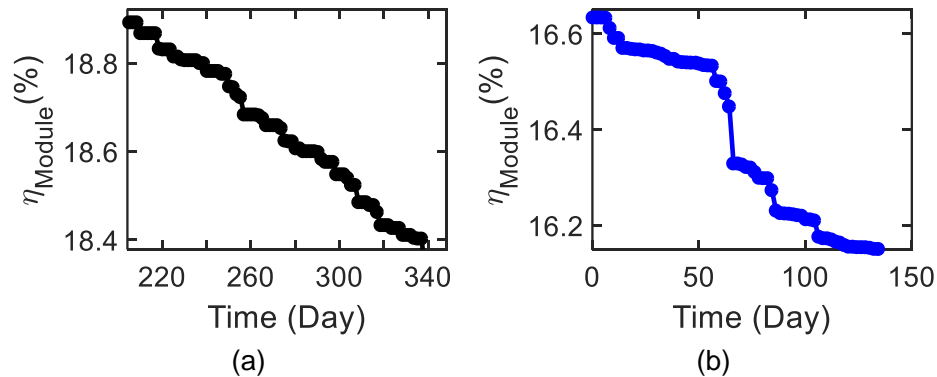


Fig. 7.8. (a) Discrete and sudden drops in efficiency due to solder bond failure results of (a) simulation and (b) extracted from measurement.

To get a compact model, the final step after validation of the model against experimental data is to extract the series resistance at the cell or module level as a function of time. Since the resistance saturates to a final value, we can fit it using a modified Sigmoidal function as described in [226]. This formula can be used in the five-parameter model of a solar cell compact model to predict the impact of solder bond failure on the overall efficiency of a solar module.

7.4 Conclusion and Summary

Starting from the ambient temperature cycles and technology-specific parameters, we used a physics-based phenomenological model to calculate the efficiency degradation of a cell undergoing solder bond failure. Due to the statistical nature of bond failure at the module level, we used a probability distribution function to find the number of cells that have a certain number of broken bonds. We assumed that the

bonds break in a consecutive manner in cells, therefore we used a macroscopic Markov chain method to calculate the probability distribution function of solder bond failure. This method enables us to find the series resistance as a function of time at the module level. Such a parameter can be used in a five-parameter compact model to predict the performance of a module that suffers from solder bond failure.

The model proposed in this chapter is one of the building blocks of a more comprehensive model that predicts the lifetime and energy output of solar panels installed in the field. The comprehensive model includes different degradation mechanisms such as yellowing, corrosion, PID, delamination, soiling, etc. This task will be explained more in the future work section of chapter 8.

8. CONCLUSIONS

In chapter 1, we introduced the concept of the levelized cost of electricity (LCOE) and the need to reduce it for solar energy so that it can compete with other sources of energy. LCOE is the cost of a unit of solar energy from the fabrication of the device to decommissioning over the energy that it produces over its lifetime. The thesis focused on three important ways we could reduce the LCOE, namely, by adopting a high-through solution-processed perovskite-based solar cell technology, by developing an innovative bifacial perovskite-silicon tandem solar cell technology, and by developing physics-based forward and inverse reliability models, suitable for 30-50 year lifetime projection.

8.1 Summary of Chapter 2: A 3D high-efficiency Perovskite Technology

We explored the ways that LCOE can be reduced by replacing c-Si with a new type of direct bandgap solar absorber called 3D perovskite. The solution-processed perovskites based on the hot-casting method is less expensive than the traditional c-Si technology. The higher absorption coefficient of perovskite dramatically reduces the amount of material needed to fabricate a solar cell. Also, the band alignment of the absorber and the electron transport material (ETM) and hole transport material (HTM) along with high carrier mobility and low defect density make the perovskite cells highly efficient. Therefore, perovskite solar cells have been suggested as a promising candidate for replacing the c-Si cells. After all, the highest verified perovskite cell efficiency is at 25.2% (based on NREL efficiency chart) is already approaching the maximum efficiency achieved by c-Si cell at 26.1%. Such rapid progress from 2.1% in 2005 to 25.2% in 2020 shows the eminent effort and demand for an inexpensive substitution for the c-Si cells. Since only a few hundred nanometers of perovskite is

needed for strong light absorption, roll-to-roll fabrication is possible that gives rise to higher throughput for perovskite cells compared to c-Si cells. This makes them an even more commercially viable option. In this chapter, we have discussed the physics and performance potential of perovskite solar cells and explained strategies for efficiency improvement.

8.2 Summary of Chapter 3: Efficiency Enhancement by Tandem Solar Cells

The next step is to improve the energy output of the fabricated cell/panel. The most important factor in energy output is efficiency. The higher the efficiency the higher the energy output. To improve efficiency one can use different materials, different cell structures, different fabrication processes to reduce the impurities or defect density. Also one can use more than one absorber layer to collect most of the solar spectrum and convert the photons to electron-hole pair. This is called a tandem structure.

In this chapter, we integrated a highly efficient perovskite cell of $\sim 20\%$ as the top cell with a standard a-Si/c-Si heterojunction (HIT) cell of $\sim 24\%$ as the bottom cell resulting in a 25% tandem structure. In the analysis, we focused on a relatively simple two-terminal series-connected tandem structure. Due to the series connection of the two sub-cells, the current of the sub-cells must be matched. Our opto-electrical simulations demonstrated that efficiency is maximized if the perovskite layer is designed for an optimal thickness of 135 nm. At the optimum point, the matched J_{SC} is $18\text{mA}/\text{cm}^2$ and it is smaller than both the sub-cells, e.g. perovskite ($\sim 24.5\text{mA}/\text{cm}^2$) and HIT ($\sim 40.5\text{mA}/\text{cm}^2$). Moreover, even a slight variation of 20 nm in the perovskite layer thickness causes the tandem cell efficiency to drop by about 1%. The high sensitivity makes the structure impractical. Furthermore, a marginal 1% increase in efficiency is not enough to include another layer of complication to the fabrication

process of HIT cells. Therefore, we proposed that a more promising solution based on bifacial tandem structure.

The bifacial tandem structure needs to replace the aluminum contact layer at the backside of the HIT cell with an ITO layer similar to a bifacial HIT cell. This structure resolves the thickness sensitivity issue by relaxing the current constraints and introducing more light from the backside. Now the bottom HIT cell has enough input illumination (depending on the available albedo light) to compensate for the variability of the light absorption for the top perovskite cell. The bifacial tandem outperforms bifacial HIT within the practical albedo light up-to 40% having a 33% normalized to one sun efficiency. This higher energy output makes the bifacial tandem suitable for many applications.

8.3 Summary of Chapter 4: Reliability of Perovskite Solar Cells

Although 3D perovskite improves efficiency and energy output, this class of materials suffers from a short lifetime when in contact with moisture or oxygen. Indeed, 3D perovskite is not stable and degrades when exposed to air. The material is hygroscopic and easily degraded and excessive/undesirable ion-mobility leads to instability and hysteresis of the solar cell characteristics. To overcome the stability/reliability and lifetime issues of 3D perovskite we worked on a type of 2D perovskite material called Ruddlesden-Popper. The 2D structure depending on its formulation has higher formation energy that makes them intrinsically more stable. Also, the existing organic spacers between the inorganic slabs of this material protects the inorganic layers from the moisture ingress. This makes the material as a whole less prone to degradation while exposed to higher humidity compared to 3D perovskite. Even after 1000 hours (about 42 days) of exposure to 85% relative humidity at 85°C the 2D perovskite cells remain above 80% of their initial output power. The problem, however, is the lower efficiency of the 2D material in comparison to 3D perovskite.

Our collaborators measured the I-V characteristics of the 2D perovskite cells at different conditions to better understand the charged carrier transport in the 2D material. The measurements were done at different absorber thicknesses, illumination intensities, and ambient temperatures. The behavior under different illumination was as expected, namely, we observed the logarithmic dependence of the J_{SC} on the intensity of sunlight due to diode (p-n junction) structure. Interestingly an increase of the absorber thickness beyond a critical value reduced J_{SC} as well as efficiency. Another anomalous feature involved V_{OC} turnover and reduced J_{SC} at a lower temperature.

We proposed a novel, vertically stacked quantum well (Q-well) energy landscape to explain these phenomena. since the carriers travel within the orientation of the inorganic slabs and not through the organic spacers we use the Q-wells as a proxy of how the organic spacers impact the transport of the charged carriers. This energy landscape thus identifies two types of carriers: quasi-bound carriers localized in low energy levels in inorganic regions and free delocalized carriers outside the potential barriers. The electrons and holes are repeatedly trapped into and de-trapped from the quasi-bound states as they are moving towards their respective contacts.

The reason for the J_{SC} being maximized at an optimum thickness is as follows. On one hand the thicker the absorber layer, the more light is being absorbed. Eventually, the absorption plateaus beyond a critical thickness. On the other hand, increasing absorber thickness increases the number of Q-wells. These wells increase the trapping/de-trapping of the carriers while they are being transferred inside the 2D perovskite. This mechanism causes more recombination inside the Q-wells and hence the short circuit current decreases. The two factors of competition define the optimum thickness. This occurs at any applied voltage, including the short circuit condition.

Regarding the temperature dependence, at a lower temperature, the carriers have less thermal energy and cannot escape the potential well they are trapped in. Therefore the recombination rate increases and both J_{SC} and FF drop at a lower temperature. In order to explain the V_{OC} turnover, we incorporated the Gaussian disorder

mobility model associated with amorphous organic regions. This model takes into account the variation of the depth of the Q-wells within the structure. A second contribution to the temperature dependence arises from the reduction of the bandgap at a lower temperature which is counter-intuitive but has been seen in both 2D and 3D perovskites. Using these models we were able to reproduce the turnover trend of the V_{OC} . Although the 2D perovskite has higher stability and is more reliable, it has lower efficiency compared to its 3D class. Based on the simulated results, decreasing the barrier by changing the organic spacer or doping, it may be possible to increase the efficiency of the Dion Jacobson class of 2D perovskite solar cells.

8.4 Summary of Chapter 5: Reliability of c-Si Solar Cells

After we have explained the possible ways of increasing the lifetime of the top cell of a tandem structure we need to investigate the reliability issues of the bottom cell which is the c-Si.

Based on a report by NREL, the internal circuitry discoloration (related to metal corrosion) is the second most frequent degradation mechanism reported for the c-Si panels. We studied the ways this mechanism affects the J-V curve of the cells and how it affects module performance. We used Griddler as a cell simulator and realized that finger thinning due to corrosion does not decrease the performance of the panels significantly unless the initial thickness of 60 to 100 μm is reduced to 20 μm . Once the finger has been thinned, the slope close to the J_{SC} (which is a proxy of shunt resistance of the cell) starts to increase. Hence, the J-V curve looks as if the cell suffers from a "fake" shunting issue. This fake shunt can be differentiated from the real shunt by looking at efficiency at low intensity. The real shunt causes the efficiency to drop at all intensities, however, the fake shunt only occurs at high illumination intensity. At any current density (close to J_{SC} for example) the generated carriers need to find the lowest resistive path towards the contact. Since the fingers are corroded, the carriers have to travel through a more resistive path of the semiconductor. This

causes a higher voltage drop on their path which turns on the distributed diodes in the vicinity of the corroded/thinned fingers. These turned-on diodes sink significantly more current through themselves due to exponential dependence of the higher applied voltage on them resulting in a lower collected current. The higher the generated photo-current, the stronger the effect and therefore, we see a slope close to J_{SC} . The next way of distinguishing the real shunt from the fake shunt is to observe the J-V curve at both reverse and forward bias. Due to the symmetric nature of the real shunt resistance, the J-V will be symmetric in that case, but the "fake" shunt current will saturate at J_{SC} either in the forward or reverse bias region of the J-V curve.

The delamination of the contacts from the silicon substrate can occur when the moisture reaches the contacts and through hydrolysis produces H_2 gas. The accumulated gas then increases the pressure under the contact and initiates the delamination. This degradation can be assumed as an extreme case of finger thinning since if the finger is fully corroded there is no metallic contact for the carriers to go through and be collected. Thus, we saw a similar J-V characteristics when compared to finger thinning simulation results.

The next mechanism that we investigated was solder bond failure. The temperature difference during night and day and also seasonal change in temperature causes the solders between the busbars and ribbons to fail due to accumulated stress over time. We show through our simulations that the sole reason for the increase of series resistance in the solar panels is solder bond failure if only the internal circuitry of the panel is subject to degradation. When the solder bonds fail, the current needs to go through a more resistive path of the busbars to find the next healthy bond. Then it can be transferred to the next cell via ribbons. However, the busbars are not resistive compared to the silicon substrate and the voltage drop due to this change of path of the current is small and the current can be collected and transferred. Therefore, we can see the shift in the voltage in the J-V curve close to the V_{OC} which is an indicator of series resistance.

We then put the degraded cells at the edges of a panel in our simulator since the moisture ingress and corrosion impacts the peripheral cells first. We found that the J-V features seen at the cell level transfer to the panel level in a similar fashion.

8.5 Summary of Chapter 6: Electrical Signature of Solder Bond Failure

We validated module simulation regarding solder bond failure by comparing the predictions with photo-luminescence, electro-luminescence, and dark lock-in thermography (DLIT) characterization results of 23 fielded modules. These spatially-resolved maps identify various locally degraded regions of the cell/panel. In contrast, J-V curves tell us the global features of the panel including the series resistance. The measured modules had mild to severe loss of initial power showing up in the reduction of their FF. That was an indicator of possible high series resistance. To show the correlation of solder bond failure and series resistance we had a hypothesis. When a bond breaks the current has to go through other healthy bonds making them more heated up due to current crowding. DLIT specifically pinpoints these hotspots telling us there is a doublet pattern of hotter and colder solder bonds within a cell. This pattern was seen on the parts that solder bonds/pads were located on the cells. Then we used image processing to count the number of hotspots in each panel. We showed a direct correlation between the number of hotspots and the loss of power with a regression coefficient of 0.8.

8.6 Summary of Chapter 7: A Physics-based Model of Solder Bond Failure

Next, we proposed a physics-based and statistical model of solder bond failure (SBF) correlating the accumulated damage in the solder bonds to the output power and lifetime of the cell/panels. We used an established semi-empirical formula that calculates the accumulated stress in the bonds based on the change in the ambient temperature as a function of time. Then we assumed a linear relationship between

the number of broken bonds and the amount of accumulated stress. Once calibrated against the result of the thermal cycling test, the approach would provide a comprehensive phenomenological description of one of the most important electro-mechanical degradation modes of a solar module.

In addition to the average degradation, we can account for the probabilistic nature of the number of broken bonds in each cell at the module level. A Markov chain method allowed us to calculate the average number of broken bonds in various cells and the fact that the total number of healthy and broken ones is independent of time. Once calibrated to the mean time to failure of the first bond, this method predicts the degradation trend of a fielded module arising from the solder bond failure and the corresponding increase in its series resistance.

To summarize, we explored several ways to reduce LCOE, namely,

1. Reducing the cost of fabrication using a new solution-processed perovskite absorber.
2. Increasing the energy output by combining c-Si and perovskite in a bifacial tandem structure.
3. Investigating the reliability issues of 3D perovskite and proposing ways to improve it using Ruddlesden-Popper 2D perovskite.
4. Analyzing the reliability issues of c-Si modules and correlated series resistance of the panels directly to their solder bond failure.
5. Proposing a phenomenological model to predict the efficiency and lifetime of a module that suffers from solder bond failure.

8.7 Future Work: Physics-based Reliability Modeling

8.7.1 Forward Modeling: Location-specific Predictive Reliability Model of a Solar Cell

As the future work, the proposed physics-based model for solder bond failure can be used as a building block of a more comprehensive model that predicts the performance of a solar panel installed in the field anywhere world-wide. Other building blocks of this comprehensive model have already been developed. Specifically, they consist of different degradation mechanisms such as potential induced degradation (PID), yellowing of the laminating polymer, PID assisted corrosion, cracking of the cells, delamination of the polymer or contacts, etc. This predictive reliability model is also known as "Forward Modeling" because one starts from the structural information of the panel and its initial I-V performance. Then, one predicts the future lifetime and energy output based on the environmental condition, such as the irradiance, ambient temperature, and wind velocity, etc. This modeling is possible since we know how each of the mechanisms impacts on the electrical signature of the module. For example, PID assisted corrosion occurs when moisture penetrates a module and reaches its contacts while the module is under illumination (See Fig. 8.1).

The reactions following the process can be simulated using Butler-Volmer equation that connects the corrosion potential and current at anode and cathode electrodes as shown in Fig. 8.2.

8.7.2 Inverse Modeling: Reading the "Heartbeat" of a Solar Farm

Forward modeling is irrelevant for farms already in existence because degradation parameters based on qualification tests are either incomplete or unavailable. For these fielded modules, we can use the historical performance data to back-calculate the parameters needed in our physics-based building blocks to predict the future performance and the lifetime of the panel. The inverse modeling is more complicated

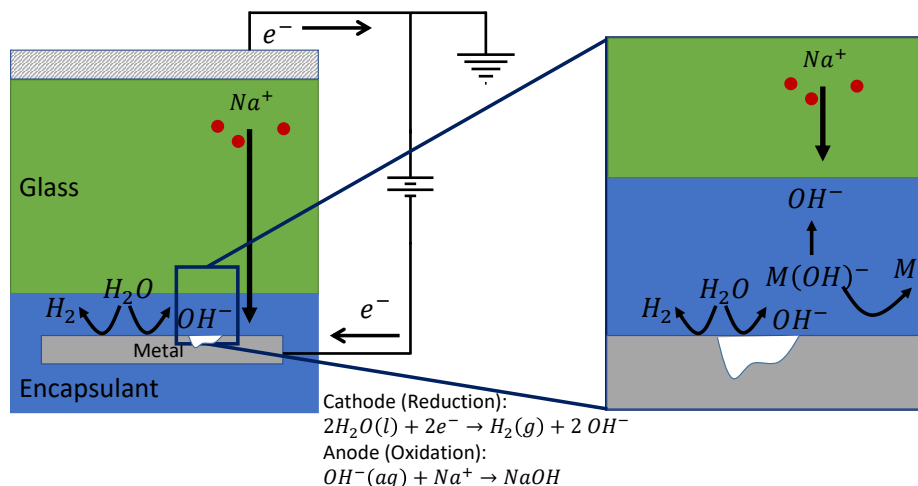


Fig. 8.1. PID assisted corrosion process needs the circuit to be completed by drifted sodium ions

when the modules are going through multiple degradation mechanisms simultaneously. However, we realized that each mechanism triggers a certain phenomenon that results in a different electrical signature. Hence when we matched the J-V curves of the modules using the five-parameter model as shown in Fig. 8.3 we could tune each parameter to manifest the impact of a degradation mechanism. Also, it can be seen how the change in one parameter can be traced back to the mechanism causing the issue. For example, we have discussed in chapter 5 how a J-V curve in reverse bias can distinguish between fake shunt due to finger thinning and real shunt due to PID. We have made significant progress regarding inverse modeling. The solder bond failure model developed in this thesis provides an important component necessary for a holistic inverse model.

The forward and inverse models will help financial intuitions better estimate of return of investment and alert the solar cell manufacturer regarding potential vulnerabilities of their designs and suggests opportunities for prolonging the lifetime of solar modules. Also, these approaches can be used to refine standard and accelerated tests to better reflect the region-specific degradation modes of solar modules.

$$I_{corr} = I_{Red,C} - I_{Ox,C} = I_{o,C} \left[\exp\left(\frac{E_{corr,C} + E_{eq,C} - I_{corr}R_{Metal}}{\beta_{Red,C}}\right) - \exp\left(\frac{I_{corr}R_{Metal} - E_{corr,C} - E_{eq,C}}{\beta_{Ox,C}}\right) \right]$$

$$I_{corr} = I_{Ox,A} - I_{Red,A} = I_{o,A} \left[\exp\left(-\frac{E_{corr,C} + I_{corr}R_{Sol} + E_{eq,A}}{\beta_{Ox,A}}\right) - \exp\left(\frac{E_{corr,C} + I_{corr}R_{Sol} + E_{eq,A}}{\beta_{Red,A}}\right) \right]$$

$$E_{eq,C} = E_{o,C} + \frac{RT}{n_C F} \ln(a_{Red,C}), E_{eq,A} = E_{o,A} + \frac{RT}{n_A F} \ln(a_{Ox,A})$$

Fig. 8.2. Electrical equivalent of Butler-Volmer equation of a freely corroding system. A stands for anode, C for cathode, Ox for oxidation, and Red for reduction. β is the Tafel slope and positive values are used in the equation, and E values are SHE reduction potential.

In closing, despite the plateauing of the cost of traditional solar cells, the analysis of various innovative techniques and technologies presented in this thesis suggests many opportunities for sustained cost reduction for many years to come. It is our hope that the adoption of strategies discussed in this thesis, along with the advances in economy-of-scale of manufacturing supported by a comprehensive program of recycling, will ultimately transform solar cell technology as the dominant source of abundant, clean, renewable, and always-available energy source for the global population.

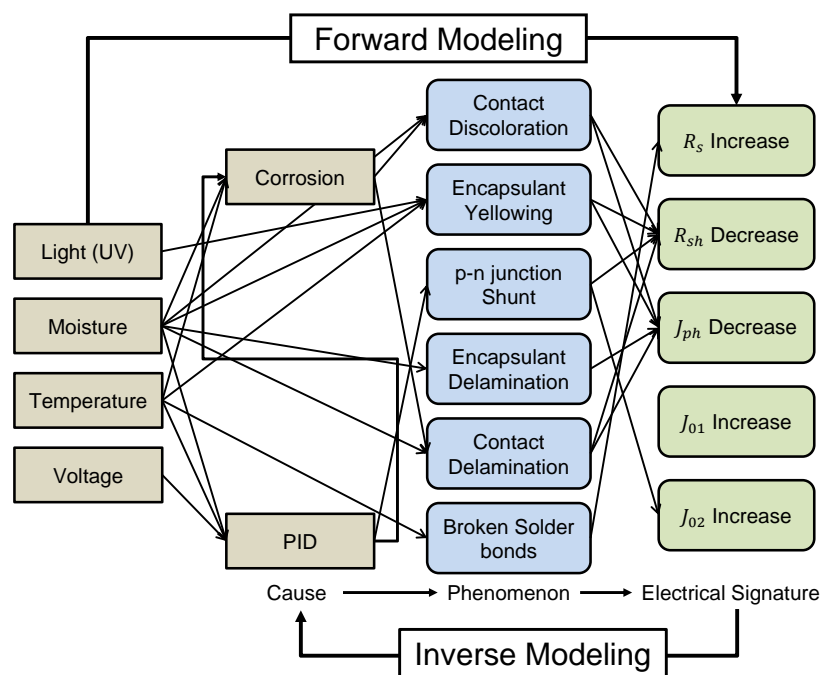


Fig. 8.3. The causes, phenomena, and electrical signatures due to causes influencing the parameters in the five-parameter model. The list is not comprehensive.

REFERENCES

REFERENCES

- [1] H. Ritchie and M. Roser, “Energy,” *Our World in Data*, 2020, <https://ourworldindata.org/energy>.
- [2] “Lazard.com — Levelized Cost of Energy and Levelized Cost of Storage 2019.” [Online]. Available: <https://www.lazard.com/perspective/lcoe2019>
- [3] O. of Energy Efficiency and R. Energy, “The History of Solar.” [Online]. Available: https://www1.eere.energy.gov/solar/pdfs/solar_{-}timeline.pdf
- [4] W. Shockley and H. J. Queisser, “Detailed balance limit of efficiency of p-n junction solar cells,” *Journal of Applied Physics*, vol. 32, no. 3, pp. 510–519, mar 1961. [Online]. Available: <http://aip.scitation.org/doi/10.1063/1.1736034>
- [5] M. A. Green, E. D. Dunlop, J. Hohl-Ebinger, M. Yoshita, N. Kopidakis, and X. Hao, “Solar cell efficiency tables (version 56),” *Progress in Photovoltaics: Research and Applications*, vol. 28, no. 7, pp. 629–638, jul 2020. [Online]. Available: <https://onlinelibrary.wiley.com/doi/abs/10.1002/pip.3303>
- [6] A. Luque and S. Hegedus, Eds., *Handbook of Photovoltaic Science and Engineering*. Chichester, UK: John Wiley & Sons, Ltd, apr 2003. [Online]. Available: <http://doi.wiley.com/10.1002/0470014008>
- [7] M. Woodhouse, B. Smith, A. Ramdas, and Robert Margolis, “Crystalline Silicon Photovoltaic Module Manufacturing Costs and Sustainable Pricing: 1H 2018 Benchmark and Cost Reduction Roadmap,” National Renewable Energy Laboratory, Golden, CO, Tech. Rep. February, 2019. [Online]. Available: <https://www.nrel.gov/docs/fy19osti/72134.pdf>.{0}ANREL
- [8] N. R. E. L. (U.S.), “Solar Manufacturing Cost Analysis — Energy Analysis — NREL.” [Online]. Available: <https://www.nrel.gov/analysis/solar-manufacturing-cost.html>
- [9] W. Nie, H. Tsai, R. Asadpour, J.-C. Blancon, A. J. Neukirch, G. Gupta, J. J. Crochet, M. Chhowalla, S. Tretiak, M. A. Alam, H.-L. Wang, and A. D. Mohite, “High-efficiency solution-processed perovskite solar cells with millimeter-scale grains,” *Science*, vol. 347, no. 6221, pp. 522–525, Jan. 2015. [Online]. Available: <http://science.sciencemag.org/content/347/6221/522>
- [10] W. Nie, J. C. Blancon, A. J. Neukirch, K. Appavoo, H. Tsai, M. Chhowalla, M. A. Alam, M. Y. Sfeir, C. Katan, J. Even, S. Tretiak, J. J. Crochet, G. Gupta, and A. D. Mohite, “Light-activated photocurrent degradation and self-healing in perovskite solar cells,” *Nature Communications*, vol. 7, may 2016.

- [11] O. Schultz, S. W. Glunz, and G. P. Willeke, "Multicrystalline silicon solar cells exceeding 20% efficiency," *Progress in Photovoltaics: Research and Applications*, vol. 12, no. 7, pp. 553–558, nov 2004. [Online]. Available: <https://onlinelibrary.wiley.com/doi/full/10.1002/pip.583><https://onlinelibrary.wiley.com/doi/abs/10.1002/pip.583><https://onlinelibrary.wiley.com/doi/10.1002/pip.583>
- [12] C. Battaglia, A. Cuevas, and S. De Wolf, "High-efficiency crystalline silicon solar cells: Status and perspectives," pp. 1552–1576, may 2016. [Online]. Available: www.rsc.org/ees
- [13] J. Kim, S. Kim, C. Zuo, M. Gao, D. Vak, and D. Kim, "Humidity-Tolerant Roll-to-Roll Fabrication of Perovskite Solar Cells via Polymer-Additive-Assisted Hot Slot Die Deposition," *Advanced Functional Materials*, vol. 29, no. 26, p. 1809194, jun 2019. [Online]. Available: <https://onlinelibrary.wiley.com/doi/abs/10.1002/adfm.201809194>
- [14] B. Dou, J. B. Whitaker, K. Bruening, D. T. Moore, L. M. Wheeler, J. Ryter, N. J. Breslin, J. J. Berry, S. M. Garner, F. S. Barnes, S. E. Shaheen, C. J. Tassone, K. Zhu, and M. F. Van Hest, "Roll-to-Roll Printing of Perovskite Solar Cells," *ACS Energy Letters*, vol. 3, no. 10, pp. 2558–2565, oct 2018. [Online]. Available: <https://pubs.acs.org/sharingguidelines>
- [15] N. L. Chang, A. W. Y. Ho-Baillie, D. Vak, M. Gao, M. A. Green, and R. J. Egan, "Manufacturing cost and market potential analysis of demonstrated roll-to-roll perovskite photovoltaic cell processes," *Solar Energy Materials and Solar Cells*, vol. 174, pp. 314–324, jan 2018.
- [16] "IEC Standard - Home." [Online]. Available: <https://www.iecee.org/dyn/www/f?p=106:49:0:::FSP{ }STD{ }ID:24313>
- [17] R. Asadpour, R. V. K. Chavali, and M. A. Alam, "Physics-Based computational modeling of moisture ingress in solar modules: Location-specific corrosion and delamination," in *Conference Record of the IEEE Photovoltaic Specialists Conference*, vol. 2016-November. Institute of Electrical and Electronics Engineers Inc., nov 2016, pp. 840–843.
- [18] P. Denholm, M. O'Connell, G. Brinkman, and J. Jorgenson, "Overgeneration from Solar Energy in California: A Field Guide to the Duck Chart (NREL/TP-6A20-65023)," National Renewable Energy Laboratory, Tech. Rep. November, 2015. [Online]. Available: <http://www.nrel.gov/docs/fy16osti/65453.pdf>
- [19] N. R. E. L. (U.S.), "Ten Years of Analyzing the Duck Chart: How an NREL Discovery in 2008 Is Helping Enable More Solar on the Grid Today — News — NREL." [Online]. Available: <https://www.nrel.gov/news/program/2018/10-years-duck-curve.html>
- [20] W. Nie, H. Tsai, R. Asadpour, J.-C. Blancon, A. J. Neukirch, G. Gupta, J. J. Crochet, M. Chhowalla, S. Tretiak, M. A. Alam, H.-L. Wang, and A. D. Mohite, "High-efficiency solution-processed perovskite solar cells with millimeter-scale grains," *Science*, vol. 347, no. 6221, pp. 522–525, jan 2015. [Online]. Available: <http://www.sciencemag.org/content/347/6221/522>

- [21] A. Kojima, K. Teshima, Y. Shirai, and T. Miyasaka, “Novel Photoelectrochemical Cell with Mesoscopic Electrodes Sensitized by Lead-halide Compounds (5),” *Meeting Abstracts*, vol. MA2007-02, no. 8, pp. 352–352, Sep. 2007. [Online]. Available: <http://ma.ecsdl.org/content/MA2007-02/8/352>
- [22] H. J. Snaith, “Perovskites: The Emergence of a New Era for Low-Cost, High-Efficiency Solar Cells,” *The Journal of Physical Chemistry Letters*, vol. 4, no. 21, pp. 3623–3630, Nov. 2013. [Online]. Available: <https://doi.org/10.1021/jz4020162>
- [23] K. Leo, “Perovskite photovoltaics: Signs of stability,” *Nature Nanotechnology*, vol. 10, no. 7, pp. 574–575, Jul. 2015. [Online]. Available: <https://www.nature.com/articles/nnano.2015.139>
- [24] “Best Research-Cell Efficiency Chart — Photovoltaic Research — NREL.” [Online]. Available: <https://www.nrel.gov/pv/cell-efficiency.html>
- [25] J. Burschka, N. Pellet, S. J. Moon, R. Humphry-Baker, P. Gao, M. K. Nazeeruddin, and M. Grätzel, “Sequential deposition as a route to high-performance perovskite-sensitized solar cells,” *Nature*, vol. 499, no. 7458, pp. 316–319, 2013.
- [26] M. M. Lee, J. Teuscher, T. Miyasaka, T. N. Murakami, and H. J. Snaith, “Efficient hybrid solar cells based on meso-superstructured organometal halide perovskites,” *Science*, vol. 338, no. 6107, pp. 643–647, nov 2012.
- [27] A. Mei, X. Li, L. Liu, Z. Ku, T. Liu, Y. Rong, M. Xu, M. Hu, J. Chen, Y. Yang, M. Grätzel, and H. Han, “A hole-conductor-free, fully printable mesoscopic perovskite solar cell with high stability,” *Science*, vol. 345, no. 6194, pp. 295–298, 2014.
- [28] H. Zhou, Q. Chen, G. Li, S. Luo, T. B. Song, H. S. Duan, Z. Hong, J. You, Y. Liu, and Y. Yang, “Interface engineering of highly efficient perovskite solar cells,” *Science*, vol. 345, no. 6196, pp. 542–546, aug 2014.
- [29] H. S. Kim, C. R. Lee, J. H. Im, K. B. Lee, T. Moehl, A. Marchioro, S. J. Moon, R. Humphry-Baker, J. H. Yum, J. E. Moser, M. Grätzel, and N. G. Park, “Lead iodide perovskite sensitized all-solid-state submicron thin film mesoscopic solar cell with efficiency exceeding 9%,” *Scientific Reports*, vol. 2, pp. 591–591, 2012.
- [30] M. Liu, M. B. Johnston, and H. J. Snaith, “Efficient planar heterojunction perovskite solar cells by vapour deposition,” *Nature*, vol. 501, no. 7467, pp. 395–398, Sep. 2013. [Online]. Available: <https://www.nature.com/articles/nature12509>
- [31] N. J. Jeon, J. H. Noh, Y. C. Kim, W. S. Yang, S. Ryu, and S. I. Seok, “Solvent engineering for high-performance inorganic-organic hybrid perovskite solar cells,” *Nature Materials*, vol. 13, no. 9, pp. 897–903, 2014.
- [32] P. Docampo, J. M. Ball, M. Darwich, G. E. Eperon, and H. J. Snaith, “Efficient organometal trihalide perovskite planar-heterojunction solar cells on flexible polymer substrates,” *Nat Commun*, vol. 4, Nov. 2013. [Online]. Available: <http://www.nature.com/ncomms/2013/131112/ncomms3761/full/ncomms3761-.html>

- [33] O. Malinkiewicz, A. Yella, Y. H. Lee, G. M. Espallargas, M. Graetzel, M. K. Nazeeruddin, and H. J. Bolink, "Perovskite solar cells employing organic charge-transport layers," *Nature Photonics*, vol. 8, no. 2, pp. 128–132, feb 2014.
- [34] J. Seo, S. Park, Y. Chan Kim, N. J. Jeon, J. H. Noh, S. C. Yoon, and S. I. Seok, "Benefits of very thin PCBM and LiF layers for solution-processed p-i-n perovskite solar cells," *Energy Environ. Sci.*, vol. 7, no. 8, pp. 2642–2646, 2014. [Online]. Available: <http://dx.doi.org/10.1039/C4EE01216J>
- [35] S. D. Stranks, G. E. Eperon, G. Grancini, C. Menelaou, M. J. P. Alcocer, T. Leijtens, L. M. Herz, A. Petrozza, and H. J. Snaith, "Electron-Hole Diffusion Lengths Exceeding 1 Micrometer in an Organometal Trihalide Perovskite Absorber," *Science*, vol. 342, no. 6156, pp. 341–344, Oct. 2013. [Online]. Available: <http://science.sciencemag.org/content/342/6156/341>
- [36] G. Xing, N. Mathews, S. Sun, S. S. Lim, Y. M. Lam, M. Gratzel, S. Mhaisalkar, and T. C. Sum, "Long-range balanced electron-and hole-transport lengths in organic-inorganic CH₃NH₃PbI₃," *Science*, vol. 342, no. 6156, pp. 344–347, 2013.
- [37] J. S. Manser and P. V. Kamat, "Band filling with free charge carriers in organometal halide perovskites," *Nature Photonics*, vol. 8, no. 9, pp. 737–743, 2014.
- [38] M. Grätzel, "The light and shade of perovskite solar cells," pp. 838–842, may 2014.
- [39] M. D. McGehee, "Perovskite solar cells: Continuing to soar," pp. 845–846, may 2014.
- [40] R. S. Sanchez, V. Gonzalez-Pedro, J. W. Lee, N. G. Park, Y. S. Kang, I. Mora-Sero, and J. Bisquert, "Slow dynamic processes in lead halide perovskite solar cells. Characteristic times and hysteresis," *Journal of Physical Chemistry Letters*, vol. 5, no. 13, pp. 2357–2363, jul 2014.
- [41] H. J. Snaith, A. Abate, J. M. Ball, G. E. Eperon, T. Leijtens, N. K. Noel, S. D. Stranks, J. T. W. Wang, K. Wojciechowski, and W. Zhang, "Anomalous hysteresis in perovskite solar cells," *Journal of Physical Chemistry Letters*, vol. 5, no. 9, pp. 1511–1515, may 2014.
- [42] G. E. Eperon, V. M. Burlakov, P. Docampo, A. Goriely, and H. J. Snaith, "Morphological control for high performance, solution-processed planar heterojunction perovskite solar cells," *Advanced Functional Materials*, vol. 24, no. 1, pp. 151–157, jan 2014.
- [43] M. Xiao, F. Huang, W. Huang, Y. Dkhissi, Y. Zhu, J. Etheridge, A. Gray-Weale, U. Bach, Y. B. Cheng, and L. Spiccia, "A fast deposition-crystallization procedure for highly efficient lead iodide perovskite thin-film solar cells," *Angewandte Chemie - International Edition*, vol. 53, no. 37, pp. 9898–9903, sep 2014.
- [44] B. Conings, L. Baeten, C. De Dobbelaere, J. D'Haen, J. Manca, and H. G. Boyen, "Perovskite-based hybrid solar cells exceeding 10% efficiency with high reproducibility using a thin film sandwich approach," *Advanced Materials*, vol. 26, no. 13, pp. 2041–2046, apr 2014.

- [45] A. Dualeh, N. Tétreault, T. Moehl, P. Gao, M. K. Nazeeruddin, and M. Grätzel, “Effect of annealing temperature on film morphology of organic-inorganic hybrid perovskite solid-state solar cells,” *Advanced Functional Materials*, vol. 24, no. 21, pp. 3250–3258, jun 2014.
- [46] Q. Wang, Y. Shao, Q. Dong, Z. Xiao, Y. Yuan, and J. Huang, “Large fill-factor bilayer iodine perovskite solar cells fabricated by a low-temperature solution-process,” *Energy and Environmental Science*, vol. 7, no. 7, pp. 2359–2365, 2014.
- [47] H. B. Kim, H. Choi, J. Jeong, S. Kim, B. Walker, S. Song, and J. Y. Kim, “Mixed solvents for the optimization of morphology in solution-processed, inverted-type perovskite/fullerene hybrid solar cells,” *Nanoscale*, vol. 6, no. 12, pp. 6679–6683, jun 2014.
- [48] “Solar cell woes,” p. 665, sep 2014. [Online]. Available: http://www.nrel.gov/ncpv/images/efficiency_{_}chart.jpg
- [49] Q. Chen, H. Zhou, Z. Hong, S. Luo, H. S. Duan, H. H. Wang, Y. Liu, G. Li, and Y. Yang, “Planar heterojunction perovskite solar cells via vapor-assisted solution process,” *Journal of the American Chemical Society*, vol. 136, no. 2, pp. 622–625, jan 2014.
- [50] G. Grancini, S. Marras, M. Prato, C. Giannini, C. Quarti, F. De Angelis, M. De Bastiani, G. E. Eperon, H. J. Snaith, L. Manna, and A. Petrozza, “The impact of the crystallization processes on the structural and optical properties of hybrid perovskite films for photovoltaics,” *Journal of Physical Chemistry Letters*, vol. 5, no. 21, pp. 3836–3842, nov 2014.
- [51] V. S. Gevaerts, L. J. A. Koster, M. M. Wienk, and R. A. J. Janssen, “Discriminating between Bilayer and Bulk Heterojunction Polymer:Fullerene Solar Cells Using the External Quantum Efficiency,” *ACS Applied Materials & Interfaces*, vol. 3, no. 9, pp. 3252–3255, Sep. 2011. [Online]. Available: <http://dx.doi.org/10.1021/am200755m>
- [52] H. Hoppe, N. S. Sariciftci, and D. Meissner, “Optical constants of conjugated polymer/fullerene based bulk-heterojunction organic solar cells,” *Molecular Crystals and Liquid Crystals*, vol. 385, no. 1, pp. 113–119, Jan. 2002. [Online]. Available: <http://dx.doi.org/10.1080/713738799>
- [53] S. Sun, T. Salim, N. Mathews, M. Duchamp, C. Boothroyd, G. Xing, T. C. Sum, and Y. M. Lam, “The origin of high efficiency in low-temperature solution-processable bilayer organometal halide hybrid solar cells,” *Energy and Environmental Science*, vol. 7, no. 1, pp. 399–407, 2014.
- [54] L. A. A. Pettersson, L. S. Roman, and O. Inganäs, “Modeling photocurrent action spectra of photovoltaic devices based on organic thin films,” *Journal of Applied Physics*, vol. 86, no. 1, pp. 487–496, Jul. 1999. [Online]. Available: <http://scitation.aip.org/content/aip/journal/jap/86/1/10.1063/1.370757>
- [55] R. F. Pierret, *Advanced Semiconductor Fundamentals*, 2nd ed. Upper Saddle River, N.J: Prentice Hall, Aug. 2002.
- [56] “Taurus Medici - Technology Computer Aided Design (TCAD) — Synopsys.” [Online]. Available: <https://www.synopsys.com/silicon/tcad/device-simulation/taurus-medici.html>

- [57] V. A. Trukhanov, V. V. Bruevich, and D. Y. Paraschuk, "Effect of doping on performance of organic solar cells," *Physical Review B*, vol. 84, no. 20, p. 205318, nov 2011. [Online]. Available: <http://link.aps.org/doi/10.1103/PhysRevB.84.205318>
- [58] S. A. Rutledge and A. S. Helmy, "Carrier mobility enhancement in poly(3,4-ethylenedioxythiophene)-poly(styrenesulfonate) having undergone rapid thermal annealing," *Journal of Applied Physics*, vol. 114, no. 13, p. 133708, oct 2013. [Online]. Available: <http://scitation.aip.org/content/aip/journal/jap/114/13/10.1063/1.4824104>
- [59] A. Lenz, H. Kariis, A. Pohl, P. Persson, and L. Ojamäe, "The electronic structure and reflectivity of PEDOT:PSS from density functional theory," *Chemical Physics*, vol. 384, no. 1–3, pp. 44–51, jun 2011. [Online]. Available: <http://www.sciencedirect.com/science/article/pii/S0301010411001571>
- [60] E. Mosconi, A. Amat, M. K. Nazeeruddin, M. Grätzel, and F. De Angelis, "First-Principles Modeling of Mixed Halide Organometal Perovskites for Photovoltaic Applications," *The Journal of Physical Chemistry C*, vol. 117, no. 27, pp. 13902–13913, jul 2013. [Online]. Available: <http://pubs.acs.org/doi/full/10.1021/jp4048659>
- [61] Z.-L. Guan, J. B. Kim, H. Wang, C. Jaye, D. A. Fischer, Y.-L. Loo, and A. Kahn, "Direct determination of the electronic structure of the poly(3-hexylthiophene):phenyl-[6,6]-C61 butyric acid methyl ester blend," *Organic Electronics*, vol. 11, no. 11, pp. 1779–1785, nov 2010. [Online]. Available: <http://www.sciencedirect.com/science/article/pii/S1566119910002533>
- [62] P. Schulz, E. Edri, S. Kirmayer, G. Hodes, D. Cahen, and A. Kahn, "Interface energetics in organo-metal halide perovskite-based photovoltaic cells," *Energy & Environmental Science*, vol. 7, no. 4, pp. 1377–1381, mar 2014. [Online]. Available: <http://pubs.rsc.org/en/content/articlelanding/2014/ee/c4ee00168k>
<http://pubs.rsc.org/en/Content/ArticleLanding/2014/EE/c4ee00168k>
- [63] B. W. Larson, J. B. Whitaker, X.-B. Wang, A. A. Popov, G. Rumbles, N. Kopidakis, S. H. Strauss, and O. V. Boltalina, "Electron Affinity of Phenyl-C61-Butyric Acid Methyl Ester (PCBM)," *The Journal of Physical Chemistry C*, vol. 117, no. 29, pp. 14958–14964, jul 2013. [Online]. Available: <http://dx.doi.org/10.1021/jp403312g>
<http://pubs.acs.org/doi/full/10.1021/jp403312g>
- [64] S. R. Cowan, A. Roy, and A. J. Heeger, "Recombination in polymer-fullerene bulk heterojunction solar cells," *Physical Review B - Condensed Matter and Materials Physics*, vol. 82, no. 24, p. 245207, 2010.
- [65] C. M. Proctor, M. Kuik, and T. Q. Nguyen, "Charge carrier recombination in organic solar cells," pp. 1941–1960, dec 2013.
- [66] C. M. Proctor, C. Kim, D. Neher, and T. Q. Nguyen, "Nongeminate recombination and charge transport limitations in diketopyrrolopyrrole-based solution-processed small molecule solar cells," *Advanced Functional Materials*, vol. 23, no. 28, pp. 3584–3594, jul 2013.

- [67] R. Asadpour, R. V. Chavali, M. Ryyan Khan, and M. A. Alam, “Bifacial Si heterojunction-perovskite organic-inorganic tandem to produce highly efficient ($\eta_T^* \approx 33\%$) solar cell,” *Applied Physics Letters*, vol. 106, no. 24, p. 243902, jun 2015. [Online]. Available: <http://aip.scitation.org/doi/10.1063/1.4922375>
- [68] K. Maki, D. Fujishima, H. Inoue, Y. Tsunomura, T. Asaumi, S. Taira, T. Kinoshita, M. Taguchi, H. Sakata, H. Kanno, and E. Maruyama, “High-efficiency HIT solar cells with a very thin structure enabling a high Voc,” in *2011 37th IEEE Photovoltaic Specialists Conference*. IEEE, Jun. 2011, pp. 000 057–000 061. [Online]. Available: <http://ieeexplore.ieee.org/lpdocs/epic03/wrapper.htm?arnumber=6185845>
- [69] M. Taguchi, A. Yano, S. Tohoda, K. Matsuyama, Y. Nakamura, T. Nishiwaki, K. Fujita, and E. Maruyama, “24.7% Record efficiency HIT solar cell on thin silicon wafer,” *IEEE Journal of Photovoltaics*, vol. 4, no. 1, pp. 96–99, jan 2014.
- [70] J. You, Z. Hong, Y. M. Yang, Q. Chen, M. Cai, T.-B. Song, C.-C. Chen, S. Lu, Y. Liu, H. Zhou, and Y. Yang, “Low-Temperature Solution-Processed Perovskite Solar Cells with High Efficiency and Flexibility,” *ACS Nano*, vol. 8, no. 2, pp. 1674–1680, Feb. 2014. [Online]. Available: <http://dx.doi.org/10.1021/nm406020d>
- [71] P. P. Boix, K. Nonomura, N. Mathews, and S. G. Mhaisalkar, “Current progress and future perspectives for organic/inorganic perovskite solar cells,” *Materials Today*, vol. 17, no. 1, pp. 16–23, Jan. 2014. [Online]. Available: <http://www.sciencedirect.com/science/article/pii/S1369702113004562>
- [72] A. S. Gudovskikh, J. P. Kleider, J. Damon-Lacoste, P. Roca i Cabarrocas, Y. Veschetti, J. C. Muller, P. J. Ribeyron, and E. Rolland, “Interface properties of a-Si:H/c-Si heterojunction solar cells from admittance spectroscopy,” *Thin Solid Films*, vol. 511–512, pp. 385–389, Jul. 2006. [Online]. Available: <http://www.sciencedirect.com/science/article/pii/S0040609005024648>
- [73] R. S. Crandall, E. Iwaniczko, J. V. Li, and M. R. Page, “A comprehensive study of hole collection in heterojunction solar cells,” *Journal of Applied Physics*, vol. 112, no. 9, p. 093713, nov 2012. [Online]. Available: <http://aip.scitation.org/doi/10.1063/1.4764031>
- [74] R. V. K. Chavali, J. R. Wilcox, B. Ray, J. L. Gray, and M. A. Alam, “Correlated Nonideal Effects of Dark and Light I–V Characteristics in a-Si/c-Si Heterojunction Solar Cells,” *IEEE Journal of Photovoltaics*, vol. 4, no. 3, pp. 763 – 771, 2014. [Online]. Available: <http://ieeexplore.ieee.org/lpdocs/epic03/wrapper.htm?arnumber=6777567>
- [75] R. Varache, J. P. Kleider, W. Favre, and L. Korte, “Band bending and determination of band offsets in amorphous/crystalline silicon heterostructures from planar conductance measurements,” *Journal of Applied Physics*, vol. 112, no. 12, p. 123717, dec 2012. [Online]. Available: <http://aip.scitation.org/doi/10.1063/1.4769736>
- [76] S. De Wolf and M. Kondo, “Abruptness of a-Si:Hc-Si interface revealed by carrier lifetime measurements,” *Applied Physics Letters*, vol. 90, no. 4, p. 042111, jan 2007. [Online]. Available: <http://aip.scitation.org/doi/10.1063/1.2432297>

- [77] R. Chavali, S. Khatavkar, C. Kannan, V. Kumar, P. Nair, J. Gray, and M. Alam, "Multiprobe Characterization of Inversion Charge for Self-Consistent Parameterization of HIT Cells," *IEEE Journal of Photovoltaics*, vol. 5, no. 3, pp. 725–735, May 2015.
- [78] L. Korte, E. Conrad, H. Angermann, R. Stangl, and M. Schmidt, "Advances in a-Si:H/c-Si heterojunction solar cell fabrication and characterization," *Solar Energy Materials and Solar Cells*, vol. 93, no. 6-7, pp. 905–910, Jun 2009.
- [79] H. Angermann, L. Korte, J. Rappich, E. Conrad, I. Sieber, M. Schmidt, K. Hübener, and J. Hauschild, "Optimisation of electronic interface properties of a-Si:H/c-Si hetero-junction solar cells by wet-chemical surface pre-treatment," *Thin Solid Films*, vol. 516, no. 20, pp. 6775–6781, Aug 2008.
- [80] A. Descoeurdes, L. Barraud, S. De Wolf, B. Strahm, D. Lachenal, C. Guérin, Z. C. Holman, F. Zicarelli, B. Demareux, J. Seif, J. Holovsky, and C. Ballif, "Improved amorphous/crystalline silicon interface passivation by hydrogen plasma treatment," *Applied Physics Letters*, vol. 99, no. 12, p. 123506, Sep 2011. [Online]. Available: <http://aip.scitation.org/doi/10.1063/1.3641899>
- [81] Z. C. Holman, A. Descoeurdes, L. Barraud, F. Z. Fernandez, J. P. Seif, S. De Wolf, and C. Ballif, "Current Losses at the Front of Silicon Heterojunction Solar Cells," *IEEE Journal of Photovoltaics*, vol. 2, no. 1, pp. 7–15, Jan. 2012. [Online]. Available: <http://ieeexplore.ieee.org/lpdocs/epic03/wrapper.htm?arnumber=6129468>
- [82] C. Ballif, S. De Wolf, A. Descoeurdes, and Z. C. Holman, "Amorphous Silicon/Crystalline Silicon Heterojunction Solar Cells," in *Semiconductors and Semimetals*. Academic Press Inc., 2014, vol. 90, pp. 73–120.
- [83] H. Zhou, Q. Chen, G. Li, S. Luo, T.-b. Song, H.-S. Duan, Z. Hong, J. You, Y. Liu, and Y. Yang, "Interface engineering of highly efficient perovskite solar cells," *Science*, vol. 345, no. 6196, pp. 542–546, Aug. 2014. [Online]. Available: <http://www.sciencemag.org/content/345/6196/542>
- [84] M. A. Green, K. Emery, Y. Hishikawa, W. Warta, and E. D. Dunlop, "Solar cell efficiency tables (Version 45)," *Progress in Photovoltaics: Research and Applications*, vol. 23, no. 1, pp. 1–9, Jan. 2015. [Online]. Available: <http://onlinelibrary.wiley.com/doi/10.1002/pip.2573/abstract>
- [85] W. Nie, H. Tsai, R. Asadpour, J.-C. Blancon, A. J. Neukirch, G. Gupta, J. Crochet, M. Chhowalla, S. Tretiak, M. A. Alam, H.-L. Wang, and A. D. Mohite, "High Efficiency Solution-Processed Perovskite Solar Cells with Millimeter-Scale Grains," *Science*, 2014.
- [86] C. D. Bailie, M. G. Christoforo, J. P. Mailoa, A. R. Bowring, E. L. Unger, W. H. Nguyen, J. Burschka, N. Pellet, J. Z. Lee, M. Grätzel, R. Noufi, T. Buonassisi, A. Salleo, and M. D. McGehee, "Semi-transparent perovskite solar cells for tandems with silicon and CIGS," *Energy & Environmental Science*, vol. 8, no. 3, pp. 956–963, Mar. 2015. [Online]. Available: <http://pubs.rsc.org/en/content/articlelanding/2015/ee/c4ee03322a>

- [87] P. Löper, S.-J. Moon, S. M. d. Nicolas, B. Niesen, M. Ledinsky, S. Nicolay, J. Bailat, J.-H. Yum, S. D. Wolf, and C. Ballif, “Organic–inorganic halide perovskite/crystalline silicon four-terminal tandem solar cells,” *Physical Chemistry Chemical Physics*, Dec. 2014. [Online]. Available: <http://pubs.rsc.org/en/content/articlelanding/2015/cp/c4cp03788j>
- [88] J. P. Mailoa, C. D. Bailie, E. C. Johlin, E. T. Hoke, A. J. Akey, W. H. Nguyen, M. D. McGehee, and T. Buonassisi, “A 2-terminal perovskite/silicon multijunction solar cell enabled by a silicon tunnel junction,” *Applied Physics Letters*, vol. 106, no. 12, p. 121105, Mar. 2015. [Online]. Available: <http://scitation.aip.org/content/aip/journal/apl/106/12/10.1063/1.4914179>
- [89] B. W. Schneider, N. N. Lal, S. Baker-Finch, and T. P. White, “Pyramidal surface textures for light trapping and antireflection in perovskite-on-silicon tandem solar cells,” *Optics Express*, vol. 22, no. S6, p. A1422, Aug. 2014.
- [90] M. Filipič, P. Löper, B. Niesen, S. De Wolf, J. Krč, C. Ballif, and M. Topič, “CH₃NH₃PbI₃ perovskite / silicon tandem solar cells: characterization based optical simulations,” *Optics Express*, vol. 23, no. 7, pp. A263–A278, Apr. 2015. [Online]. Available: <http://www.opticsexpress.org/abstract.cfm?URI=oe-23-7-A263>
- [91] G. Xing, N. Mathews, S. S. Lim, N. Yantara, X. Liu, D. Sabba, M. Grätzel, S. Mhaisalkar, and T. C. Sum, “Low-temperature solution-processed wavelength-tunable perovskites for lasing,” *Nature Materials*, vol. 13, no. 5, pp. 476–480, May 2014. [Online]. Available: <http://www.nature.com/nmat/journal/v13/n5/full/nmat3911.html>
- [92] “Taurus Medici,” United States, 2010.
- [93] S. P. Bremner, M. Y. Levy, and C. B. Honsberg, “Analysis of tandem solar cell efficiencies under AM1.5G spectrum using a rapid flux calculation method,” *Progress in Photovoltaics: Research and Applications*, vol. 16, no. 3, pp. 225–233, May 2008. [Online]. Available: <http://onlinelibrary.wiley.com/doi/10.1002/pip.799/abstract>
- [94] A. Banerjee and S. Guha, “Study of back reflectors for amorphous silicon alloy solar cell application,” *Journal of Applied Physics*, vol. 69, no. 2, pp. 1030–1035, Jan. 1991. [Online]. Available: <http://scitation.aip.org/content/aip/journal/jap/69/2/10.1063/1.347418>
- [95] R. Chen, S. R. Das, C. Jeong, M. R. Khan, D. B. Janes, and M. A. Alam, “Co-Percolating Graphene-Wrapped Silver Nanowire Network for High Performance, Highly Stable, Transparent Conducting Electrodes,” *Advanced Functional Materials*, vol. 23, no. 41, pp. 5150–5158, nov 2013. [Online]. Available: <http://doi.wiley.com/10.1002/adfm.201300124>
- [96] R. Zhu, C. H. Chung, K. C. Cha, W. Yang, Y. B. Zheng, H. Zhou, T. B. Song, C. C. Chen, P. S. Weiss, G. Li, and Y. Yang, “Fused silver nanowires with metal oxide nanoparticles and organic polymers for highly transparent conductors,” *ACS Nano*, vol. 5, no. 12, pp. 9877–9882, dec 2011. [Online]. Available: <http://www.ncbi.nlm.nih.gov/pubmed/22035334>

- [97] W. Gaynor, G. F. Burkhard, M. D. McGehee, and P. Peumans, "Smooth nanowire/polymer composite transparent electrodes," *Advanced Materials*, vol. 23, no. 26, pp. 2905–2910, jul 2011. [Online]. Available: <http://www.ncbi.nlm.nih.gov/pubmed/21538594>
- [98] U. Feister and R. Grewe, "SPECTRAL ALBEDO MEASUREMENTS IN THE UV and VISIBLE REGION OVER DIFFERENT TYPES OF SURFACES," *Photochemistry and Photobiology*, vol. 62, no. 4, pp. 736–744, Oct. 1995. [Online]. Available: <http://onlinelibrary.wiley.com/doi/10.1111/j.1751-1097.1995.tb08723.x/abstract>
- [99] H. Tsai, W. Nie, J. C. Blancon, C. C. Stoumpos, R. Asadpour, B. Harutyunyan, A. J. Neukirch, R. Verduzco, J. J. Crochet, S. Tretiak, L. Pedesseau, J. Even, M. A. Alam, G. Gupta, J. Lou, P. M. Ajayan, M. J. Bedzyk, M. G. Kanatzidis, and A. D. Mohite, "High-efficiency two-dimensional ruddlesden-popper perovskite solar cells," *Nature*, vol. 536, no. 7616, pp. 312–317, jul 2016.
- [100] H. Tsai, R. Asadpour, J. C. Blancon, C. C. Stoumpos, J. Even, P. M. Ajayan, M. G. Kanatzidis, M. A. Alam, A. D. Mohite, and W. Nie, "Design principles for electronic charge transport in solution-processed vertically stacked 2D perovskite quantum wells," *Nature Communications*, vol. 9, no. 1, pp. 1–9, dec 2018.
- [101] P. Calado, A. M. Telford, D. Bryant, X. Li, J. Nelson, B. C. O'Regan, and P. R. F. Barnes, "Evidence for ion migration in hybrid perovskite solar cells with minimal hysteresis," *Nature Communications*, vol. 7, p. 13831, Dec. 2016. [Online]. Available: <https://www.nature.com/articles/ncomms13831>
- [102] Z. Li, C. Xiao, Y. Yang, S. P. Harvey, D. H. Kim, J. A. Christians, M. Yang, P. Schulz, S. U. Nanayakkara, C.-S. Jiang, J. M. Luther, J. J. Berry, M. C. Beard, M. M. Al-Jassim, and K. Zhu, "Extrinsic ion migration in perovskite solar cells," *Energy & Environmental Science*, vol. 10, no. 5, pp. 1234–1242, May 2017. [Online]. Available: <http://pubs.rsc.org/en/content/articlelanding/2017/ee/c7ee00358g>
- [103] V. Nandal and P. R. Nair, "Predictive Modeling of Ion Migration Induced Degradation in Perovskite Solar Cells," *ACS Nano*, vol. 11, no. 11, pp. 11 505–11 512, Nov. 2017. [Online]. Available: <https://doi.org/10.1021/acsnano.7b06294>
- [104] Z. Song, A. Abate, S. C. Watthage, G. K. Liyanage, A. B. Phillips, U. Steiner, M. Graetzel, and M. J. Heben, "In-situ observation of moisture-induced degradation of perovskite solar cells using laser-beam induced current," in *2016 IEEE 43rd Photovoltaic Specialists Conference (PVSC)*, Jun. 2016, pp. 1202–1206.
- [105] J. Yang, B. D. Siempelkamp, D. Liu, and T. L. Kelly, "Investigation of CH₃NH₃PbI₃ Degradation Rates and Mechanisms in Controlled Humidity Environments Using in Situ Techniques," *ACS Nano*, vol. 9, no. 2, pp. 1955–1963, Feb. 2015. [Online]. Available: <https://doi.org/10.1021/nn506864k>

- [106] N.-K. Kim, Y. H. Min, S. Noh, E. Cho, G. Jeong, M. Joo, S.-W. Ahn, J. S. Lee, S. Kim, K. Ihm, H. Ahn, Y. Kang, H.-S. Lee, and D. Kim, "Investigation of Thermally Induced Degradation in CH₃NH₃PbI₃ Perovskite Solar Cells using In-situ Synchrotron Radiation Analysis," *Scientific Reports*, vol. 7, no. 1, p. 4645, Jul. 2017. [Online]. Available: <https://www.nature.com/articles/s41598-017-04690-w>
- [107] Li Xiong, Tschumi Manuel, Han Hongwei, Babkair Saeed Salem, Alzubaydi Raysah Ali, Ansari Azhar Ahmad, Habib Sami S., Nazeeruddin Mohammad Khaja, Zakeeruddin Shaik M., and Grätzel Michael, "Outdoor Performance and Stability under Elevated Temperatures and Long-Term Light Soaking of Triple-Layer Mesoporous Perovskite Photovoltaics," *Energy Technology*, vol. 3, no. 6, pp. 551–555, May 2015. [Online]. Available: <https://onlinelibrary.wiley.com/doi/abs/10.1002/ente.201500045>
- [108] Y. Han, S. Meyer, Y. Dkhissi, K. Weber, J. M. Pringle, U. Bach, L. Spiccia, and Y.-B. Cheng, "Degradation observations of encapsulated planar CH₃NH₃PbI₃ perovskite solar cells at high temperatures and humidity," *Journal of Materials Chemistry A*, vol. 3, no. 15, pp. 8139–8147, Mar. 2015. [Online]. Available: <http://pubs.rsc.org/en/content/articlelanding/2015/ta/c5ta00358j>
- [109] S. Guarnera, A. Abate, W. Zhang, J. M. Foster, G. Richardson, A. Petrozza, and H. J. Snaith, "Improving the Long-Term Stability of Perovskite Solar Cells with a Porous Al₂O₃ Buffer Layer," *The Journal of Physical Chemistry Letters*, vol. 6, no. 3, pp. 432–437, Feb. 2015. [Online]. Available: <https://doi.org/10.1021/jz502703p>
- [110] Z. Zhu, D. Zhao, C.-C. Chueh, X. Shi, Z. Li, and A. K. Y. Jen, "Highly Efficient and Stable Perovskite Solar Cells Enabled by All-Crosslinked Charge-Transporting Layers," *Joule*, vol. 2, no. 1, pp. 168–183, Jan. 2018. [Online]. Available: <http://www.sciencedirect.com/science/article/pii/S2542435117301770>
- [111] A. Fakharuddin, F. Di Giacomo, I. Ahmed, Q. Wali, T. M. Brown, and R. Jose, "Role of morphology and crystallinity of nanorod and planar electron transport layers on the performance and long term durability of perovskite solar cells," *Journal of Power Sources*, vol. 283, pp. 61–67, Jun. 2015. [Online]. Available: <http://www.sciencedirect.com/science/article/pii/S0378775315003183>
- [112] Smith Ian C., Hoke Eric T., Solis-Ibarra Diego, McGehee Michael D., and Karunadasa Hemamala I., "A Layered Hybrid Perovskite Solar-Cell Absorber with Enhanced Moisture Stability," *Angewandte Chemie*, vol. 126, no. 42, pp. 11414–11417, Oct. 2014. [Online]. Available: <https://onlinelibrary.wiley.com/doi/abs/10.1002/ange.201406466>
- [113] D. H. Cao, C. C. Stoumpos, O. K. Farha, J. T. Hupp, and M. G. Kanatzidis, "2D Homologous Perovskites as Light-Absorbing Materials for Solar Cell Applications," *Journal of the American Chemical Society*, vol. 137, no. 24, pp. 7843–7850, Jun. 2015. [Online]. Available: <https://doi.org/10.1021/jacs.5b03796>

- [114] C. C. Stoumpos, D. H. Cao, D. J. Clark, J. Young, J. M. Rondinelli, J. I. Jang, J. T. Hupp, and M. G. Kanatzidis, "Ruddlesden–Popper Hybrid Lead Iodide Perovskite 2D Homologous Semiconductors," *Chemistry of Materials*, vol. 28, no. 8, pp. 2852–2867, Apr. 2016. [Online]. Available: <https://doi.org/10.1021/acs.chemmater.6b00847>
- [115] D. Saponi, M. Kepenekian, L. Pedesseau, C. Katan, and J. Even, "Quantum confinement and dielectric profiles of colloidal nanoplatelets of halide inorganic and hybrid organic-inorganic perovskites," *Nanoscale*, vol. 8, no. 12, pp. 6369–6378, mar 2016.
- [116] L. Pedesseau, D. Saponi, B. Traore, R. Robles, H. H. Fang, M. A. Loi, H. Tsai, W. Nie, J. C. Blancon, A. Neukirch, S. Tretiak, A. D. Mohite, C. Katan, J. Even, and M. Kepenekian, "Advances and Promises of Layered Halide Hybrid Perovskite Semiconductors," 2016.
- [117] J. Even, L. Pedesseau, and C. Katan, "Understanding quantum confinement of charge carriers in layered 2D hybrid perovskites," *ChemPhysChem*, 2014.
- [118] T. Ishihara, "Optical properties of PbI-based perovskite structures," *Journal of Luminescence*, vol. 60-61, no. C, pp. 269–274, 1994.
- [119] X. Hong, T. Ishihara, and A. V. Nurmikko, "Dielectric confinement effect on excitons in PbI₄-based layered semiconductors," *Physical Review B*, vol. 45, no. 12, pp. 6961–6964, 1992.
- [120] E. A. Muljarov, S. G. Tikhodeev, N. A. Gippius, and T. Ishihara, "Excitons in self-organized semiconductor/insulator superlattices: PbI-based perovskite compounds," *Physical Review B*, vol. 51, no. 20, pp. 14 370–14 378, 1995.
- [121] K. Tanaka and T. Kondo, "Bandgap and exciton binding energies in lead-iodide-based natural quantum-well crystals," *Science and Technology of Advanced Materials*, vol. 4, no. 6, pp. 599–604, 2003.
- [122] I. B. Koutselas, L. Ducasse, and G. C. Papavassiliou, "Electronic properties of three- and low-dimensional semiconducting materials with Pb halide and Sn halide units," *Journal of Physics: Condensed Matter*, vol. 8, no. 9, pp. 1217–1227, feb 1996. [Online]. Available: <http://stacks.iop.org/0953-8984/8/i=9/a=012?key=crossref.67a360944a23a70b88147433a5da0d8e>
- [123] O. Yaffe, A. Chernikov, Z. M. Norman, Y. Zhong, A. Velauthapillai, A. Van Der Zande, J. S. Owen, and T. F. Heinz, "Excitons in ultrathin organic-inorganic perovskite crystals," *Physical Review B - Condensed Matter and Materials Physics*, vol. 92, no. 4, p. 045414, jul 2015.
- [124] C. C. Stoumpos, C. M. M. Soe, H. Tsai, W. Nie, J. C. Blancon, D. H. Cao, F. Liu, B. Traoré, C. Katan, J. Even, A. D. Mohite, and M. G. Kanatzidis, "High Members of the 2D Ruddlesden-Popper Halide Perovskites: Synthesis, Optical Properties, and Solar Cells of (CH₃(CH₂)₃NH₃)₂(CH₃NH₃)₄Pb₅I₁₆," *Chem*, vol. 2, no. 3, pp. 427–440, mar 2017.

- [125] C. M. M. Soe, C. C. Stoumpos, M. Kepenekian, B. Traoré, H. Tsai, W. Nie, B. Wang, C. Katan, R. Seshadri, A. D. Mohite, J. Even, T. J. Marks, and M. G. Kanatzidis, “New Type of 2D Perovskites with Alternating Cations in the Interlayer Space, $(\text{C}(\text{NH}_2)_3)(\text{CH}_3\text{NH}_3)_n\text{PbI}_{3n+1}$: Structure, Properties, and Photovoltaic Performance,” *Journal of the American Chemical Society*, vol. 139, no. 45, pp. 16 297–16 309, nov 2017.
- [126] C. M. M. Soe, W. Nie, C. C. Stoumpos, H. Tsai, J. C. Blancon, F. Liu, J. Even, T. J. Marks, A. D. Mohite, and M. G. Kanatzidis, “Understanding Film Formation Morphology and Orientation in High Member 2D Ruddlesden–Popper Perovskites for High-Efficiency Solar Cells,” *Advanced Energy Materials*, vol. 8, no. 1, p. 1700979, jan 2018.
- [127] X. Zhang, X. Ren, B. Liu, R. Munir, X. Zhu, D. Yang, J. Li, Y. Liu, D. M. Smilgies, R. Li, Z. Yang, T. Niu, X. Wang, A. Amassian, K. Zhao, and S. Liu, “Stable high efficiency two-dimensional perovskite solar cells via cesium doping,” *Energy and Environmental Science*, vol. 10, no. 10, pp. 2095–2102, oct 2017.
- [128] H. Tsai, W. Nie, J.-C. Blancon, C. C. Stoumpos, R. Asadpour, B. Harutyunyan, A. J. Neukirch, R. Verduzco, J. J. Crochet, S. Tretiak, L. Pedesseau, J. Even, M. A. Alam, G. Gupta, J. Lou, P. M. Ajayan, M. J. Bedzyk, M. G. Kanatzidis, and A. D. Mohite, “High-efficiency two-dimensional Ruddlesden–Popper perovskite solar cells,” *Nature*, vol. 536, no. 7616, pp. 312–316, Aug. 2016. [Online]. Available: <http://www.nature.com/nature/journal/v536/n7616/abs/nature18306.html>
- [129] L. N. Quan, M. Yuan, R. Comin, O. Voznyy, E. M. Bearegard, S. Hoogland, A. Buin, A. R. Kirmani, K. Zhao, A. Amassian, D. H. Kim, and E. H. Sargent, “Ligand-Stabilized Reduced-Dimensionality Perovskites,” *Journal of the American Chemical Society*, vol. 138, no. 8, pp. 2649–2655, Mar. 2016. [Online]. Available: <https://doi.org/10.1021/jacs.5b11740>
- [130] J.-C. Blancon, H. Tsai, W. Nie, C. C. Stoumpos, L. Pedesseau, C. Katan, M. Kepenekian, C. M. M. Soe, K. Appavoo, M. Y. Sfeir, S. Tretiak, P. M. Ajayan, M. G. Kanatzidis, J. Even, J. J. Crochet, and A. D. Mohite, “Extremely efficient internal exciton dissociation through edge states in layered 2D perovskites,” *Science*, p. eaal4211, Mar. 2017. [Online]. Available: <http://science.sciencemag.org/content/early/2017/03/08/science.aal4211>
- [131] M. A. Alam, M. S. Hybertsen, R. Kent Smith, and G. A. Baraff, “Simulation of semiconductor quantum well lasers,” *IEEE Transactions on Electron Devices*, vol. 47, no. 10, pp. 1917–1925, oct 2000.
- [132] H. Tsai, W. Nie, J. C. Blancon, C. C. Stoumpos, C. M. M. Soe, J. Yoo, J. Crochet, S. Tretiak, J. Even, A. Sadhanala, G. Azzellino, R. Brenes, P. M. Ajayan, V. Bulović, S. D. Stranks, R. H. Friend, M. G. Kanatzidis, and A. D. Mohite, “Stable Light-Emitting Diodes Using Phase-Pure Ruddlesden–Popper Layered Perovskites,” *Advanced Materials*, vol. 30, no. 6, p. 1704217, feb 2018.
- [133] J. C. Blancon, W. Nie, A. J. Neukirch, G. Gupta, S. Tretiak, L. Cognet, A. D. Mohite, and J. J. Crochet, “The Effects of Electronic Impurities and Electron–Hole Recombination Dynamics on Large-Grain Organic–Inorganic Perovskite Photovoltaic Efficiencies,” *Advanced Functional Materials*, vol. 26, no. 24, pp. 4283–4292, jun 2016.

- [134] A. Miyata, A. Mitioglu, P. Plochocka, O. Portugall, J. T. W. Wang, S. D. Stranks, H. J. Snaith, and R. J. Nicholas, "Direct measurement of the exciton binding energy and effective masses for charge carriers in organic-inorganic trihalide perovskites," *Nature Physics*, vol. 11, no. 7, pp. 582–587, jul 2015.
- [135] R. Mauer, I. A. Howard, and F. Laquai, "Effect of nongeminate recombination on fill factor in polythiophene/ methanofullerene organic solar cells," *Journal of Physical Chemistry Letters*, vol. 1, no. 24, pp. 3500–3505, dec 2010.
- [136] J. Nelson, "Diffusion-limited recombination in polymer-fullerene blends and its influence on photocurrent collection," *Physical Review B - Condensed Matter and Materials Physics*, vol. 67, no. 15, p. 155209, apr 2003.
- [137] C. G. Shuttle, B. O'Regan, A. M. Ballantyne, J. Nelson, D. D. Bradley, and J. R. Durrant, "Bimolecular recombination losses in polythiophene: Fullerene solar cells," *Physical Review B - Condensed Matter and Materials Physics*, vol. 78, no. 11, p. 113201, sep 2008.
- [138] A. K. K. Kyaw, D. H. Wang, V. Gupta, W. L. Leong, L. Ke, G. C. Bazan, and A. J. Heeger, "Intensity dependence of current-voltage characteristics and recombination in high-efficiency solution-processed small-molecule solar cells," *ACS Nano*, vol. 7, no. 5, pp. 4569–4577, may 2013.
- [139] A. Maurano, R. Hamilton, C. G. Shuttle, A. M. Ballantyne, J. Nelson, B. O'Regan, W. Zhang, I. McCulloch, H. Azimi, M. Morana, C. J. Brabec, and J. R. Durrant, "Recombination dynamics as a key determinant of open circuit voltage in organic bulk heterojunction solar cells: A comparison of four different donor polymers," *Advanced Materials*, vol. 22, no. 44, pp. 4987–4992, nov 2010.
- [140] L. J. Koster, V. D. Mihailetschi, R. Ramaker, and P. W. Blom, "Light intensity dependence of open-circuit voltage of polymer:fullerene solar cells," *Applied Physics Letters*, vol. 86, no. 12, pp. 1–3, mar 2005.
- [141] V. Gupta, A. K. K. Kyaw, D. H. Wang, S. Chand, G. C. Bazan, and A. J. Heeger, "Barium: An efficient cathode layer for bulk-heterojunction solar cells," *Scientific Reports*, vol. 3, jun 2013.
- [142] B. Ray, A. G. Baradwaj, M. R. Khan, B. W. Boudouris, and M. A. Alam, "Collection-limited theory interprets the extraordinary response of single semiconductor organic solar cells," *Proceedings of the National Academy of Sciences of the United States of America*, vol. 112, no. 36, pp. 11 193–11 198, sep 2015.
- [143] J. C. Scott and G. G. Malliaras, "Charge injection and recombination at the metal-organic interface," *Chemical Physics Letters*, vol. 299, no. 2, pp. 115–119, jan 1999.
- [144] R. V. K. Chavali, J. V. Li, C. Battaglia, S. D. Wolf, J. L. Gray, and M. A. Alam, "A Generalized Theory Explains the Anomalous Suns-Voc Response of Si Heterojunction Solar Cells," *IEEE Journal of Photovoltaics*, vol. 7, no. 1, pp. 169–176, Jan. 2017.

- [145] W. Yang, Y. Luo, P. Guo, H. Sun, and Y. Yao, "Leakage Current Induced by Energetic Disorder in Organic Bulk Heterojunction Solar Cells: Comprehending the Ultrahigh Loss of Open-Circuit Voltage at Low Temperatures," *Physical Review Applied*, vol. 7, no. 4, p. 044017, Apr. 2017. [Online]. Available: <https://link.aps.org/doi/10.1103/PhysRevApplied.7.044017>
- [146] Bässler H., "Charge Transport in Disordered Organic Photoconductors a Monte Carlo Simulation Study," *physica status solidi (b)*, vol. 175, no. 1, pp. 15–56, Feb. 2006. [Online]. Available: <https://onlinelibrary.wiley.com/doi/abs/10.1002/pssb.2221750102>
- [147] R. Asadpour, X. Sun, and M. A. Alam, "Electrical Signatures of Corrosion and Solder Bond Failure in c-Si Solar Cells and Modules," *IEEE Journal of Photovoltaics*, vol. 9, no. 3, pp. 759–767, May 2019.
- [148] D. C. Jordan, T. J. Silverman, J. H. Wohlgemuth, S. R. Kurtz, and K. T. VanSant, "Photovoltaic failure and degradation modes," *Progress in Photovoltaics: Research and Applications*, vol. 25, no. 4, pp. 318–326, Apr. 2017. [Online]. Available: <http://onlinelibrary.wiley.com/doi/10.1002/pip.2866/abstract>
- [149] J. H. Wohlgemuth, D. W. Cunningham, P. Monus, J. Miller, and A. Nguyen, "Long Term Reliability of Photovoltaic Modules," in *2006 IEEE 4th World Conference on Photovoltaic Energy Conference*, vol. 2, May 2006, pp. 2050–2053.
- [150] D. C. Jordan and S. R. Kurtz, "Photovoltaic Degradation Rates—an Analytical Review," *Progress in Photovoltaics: Research and Applications*, vol. 21, no. 1, pp. 12–29, Jan. 2013. [Online]. Available: <http://onlinelibrary.wiley.com/doi/10.1002/pip.1182/abstract>
- [151] E. E. van Dyk, J. B. Chamel, and A. R. Gxasheka, "Investigation of delamination in an edge-defined film-fed growth photovoltaic module," *Solar Energy Materials and Solar Cells*, vol. 88, no. 4, pp. 403–411, Sep. 2005. [Online]. Available: <http://www.sciencedirect.com/science/article/pii/S0927024804004866>
- [152] W. Oh, S. Kim, S. Bae, N. Park, Y. Kang, H.-S. Lee, and D. Kim, "The degradation of multi-crystalline silicon solar cells after damp heat tests," *Microelectronics Reliability*, vol. 54, no. 9, pp. 2176–2179, Sep. 2014. [Online]. Available: <http://www.sciencedirect.com/science/article/pii/S0026271414002674>
- [153] X. Han, Y. Wang, L. Zhu, H. Xiang, and H. Zhang, "Mechanism study of the electrical performance change of silicon concentrator solar cells immersed in de-ionized water," *Energy Conversion and Management*, vol. 53, no. 1, pp. 1–10, Jan. 2012. [Online]. Available: <http://www.sciencedirect.com/science/article/pii/S0196890411002238>
- [154] P. Hacke, K. Terwilliger, S. Glick, D. Trudell, N. Bosco, S. Johnston, and S. Kurtz, "Test-to-Failure of crystalline silicon modules," in *2010 35th IEEE Photovoltaic Specialists Conference*, Jun. 2010, pp. 000 244–000 250.

- [155] M. Kloos, I. Bennett, S. Kurtz, S. Johnston, N. Call, S. Glick, K. Terwilliger, M. Kempe, and P. Hacke, "Characterization of Multicrystalline Silicon Modules with System Bias Voltage Applied in Damp Heat," in *25th European Photovoltaic Solar Energy Conference and Exhibition / 5th World Conference on Photovoltaic Energy Conversion, 6-10 September 2010, Valencia, Spain*, Oct. 2010, pp. 3760–3765. [Online]. Available: <http://www.eupvsec-proceedings.com/proceedings?paper=8802>
- [156] P. Hacke, R. Smith, K. Terwilliger, S. Glick, D. Jordan, S. Johnston, M. Kempe, and S. Kurtz, "Testing and Analysis for Lifetime Prediction of Crystalline Silicon PV Modules Undergoing Degradation by System Voltage Stress," *IEEE Journal of Photovoltaics*, vol. 3, no. 1, pp. 246–253, Jan. 2013.
- [157] P. Hacke, K. Terwilliger, S. Glick, R. Smith, G. Perrin, S. Kurtz, N. Bosco, and J. Wohlgemuth, "Application of the terrestrial photovoltaic module accelerated test-to-failure protocol," in *2014 IEEE 40th Photovoltaic Specialist Conference (PVSC)*, Jun. 2014, pp. 0930–0936.
- [158] C. Peike, S. Hoffmann, P. Hülsmann, B. Thaidigsmann, K. A. Weiß, M. Koehl, and P. Bentz, "Origin of damp-heat induced cell degradation," *Solar Energy Materials and Solar Cells*, vol. 116, pp. 49–54, Sep. 2013. [Online]. Available: <http://www.sciencedirect.com/science/article/pii/S0927024813001359>
- [159] M. D. Kempe, "Modeling of rates of moisture ingress into photovoltaic modules," *Solar Energy Materials and Solar Cells*, vol. 90, no. 16, pp. 2720–2738, Oct. 2006. [Online]. Available: <http://www.sciencedirect.com/science/article/pii/S0927024806001632>
- [160] M. Jankovec, F. Galliano, E. Annigoni, H. Y. Li, F. Sculati-Meillaud, L. E. Perret-Aebi, C. Ballif, and M. Topič, "In-Situ Monitoring of Moisture Ingress in PV Modules Using Digital Humidity Sensors," *IEEE Journal of Photovoltaics*, vol. 6, no. 5, pp. 1152–1159, Sep. 2016.
- [161] J. D. Fields, M. I. Ahmad, V. L. Pool, J. Yu, D. G. V. Campen, P. A. Parilla, M. F. Toney, and M. F. A. M. v. Hest, "The formation mechanism for printed silver-contacts for silicon solar cells," *Nature Communications*, vol. 7, p. 11143, Apr. 2016. [Online]. Available: <https://www.nature.com/articles/ncomms11143>
- [162] J. Wong, "Griddler: Intelligent computer aided design of complex solar cell metallization patterns," in *2013 IEEE 39th Photovoltaic Specialists Conference (PVSC)*, Jun. 2013, pp. 0933–0938.
- [163] M. D. Kempe, G. J. Jorgensen, K. M. Terwilliger, T. J. McMahon, C. E. Kennedy, and T. T. Borek, "Acetic acid production and glass transition concerns with ethylene-vinyl acetate used in photovoltaic devices," *Solar Energy Materials and Solar Cells*, vol. 91, no. 4, pp. 315–329, Feb. 2007. [Online]. Available: <http://www.sciencedirect.com/science/article/pii/S0927024806004107>
- [164] A. Kraft, L. Labusch, T. Ensslen, I. Dürr, J. Bartsch, M. Glatthaar, S. Glunz, and H. Reinecke, "Investigation of Acetic Acid Corrosion Impact on Printed Solar Cell Contacts," *IEEE Journal of Photovoltaics*, vol. 5, no. 3, pp. 736–743, May 2015.

- [165] Yu-Chen Shen, "Electrochemical Mechanisms of Leakage-Current-Induced Delamination and Corrosion in Si Photovoltaic Modules," Lakewood, Colorado, USA, Feb. 2017.
- [166] A. Kraft, Y. Pernia, A. Kalio, A. Gautrein, L. Ni, J. Bartsch, S. Glunz, and H. Reinecke, "Origin of corrosion effects in solar cell contacts during electrochemical nickel deposition," *Journal of Applied Electrochemistry*, vol. 45, no. 1, pp. 95–104, Jan. 2015. [Online]. Available: <https://link.springer.com/article/10.1007/s10800-014-0770-3>
- [167] H. Xiong, C. Gan, X. Yang, Z. Hu, H. Niu, J. Li, J. Si, P. Xing, and X. Luo, "Corrosion behavior of crystalline silicon solar cells," *Microelectronics Reliability*, vol. 70, no. Supplement C, pp. 49–58, Mar. 2017. [Online]. Available: <http://www.sciencedirect.com/science/article/pii/S0026271417300069>
- [168] M. Gagliardi, P. Lenarda, and M. Paggi, "A reaction-diffusion formulation to simulate EVA polymer degradation in environmental and accelerated ageing conditions," *Solar Energy Materials and Solar Cells*, vol. 164, pp. 93–106, May 2017. [Online]. Available: <http://www.sciencedirect.com/science/article/pii/S0927024817300673>
- [169] S. Bowden and A. Rohatgi, "Rapid and accurate determination of series resistance and fill factor losses in industrial silicon solar cells," in *Proc. 17. EU PVSEC*, Munich, Germany, Oct. 2001, p. 1802.
- [170] D. Chianese, A. Realini, N. Cereghetti, A. Rezzonico, E. Bura, G. Friesen, and A. Bernasconi, "Analysis of weathered c-Si PV modules," in *Proceedings of 3rd World Conference on Photovoltaic Energy Conversion, 2003*, vol. 3, May 2003, pp. 2922–2926 Vol.3.
- [171] C. Radue and E. E. van Dyk, "A comparison of degradation in three amorphous silicon PV module technologies," *Solar Energy Materials and Solar Cells*, vol. 94, no. 3, pp. 617–622, Mar. 2010. [Online]. Available: <http://www.sciencedirect.com/science/article/pii/S0927024809004395>
- [172] E. Kaplani, "Detection of Degradation Effects in Field-Aged c-Si Solar Cells through IR Thermography and Digital Image Processing," *International Journal of Photoenergy*, vol. 2012, pp. 1–11, 2012. [Online]. Available: <http://www.hindawi.com/journals/ijp/2012/396792/>
- [173] J. Zhu, M. Koehl, S. Hoffmann, K. A. Berger, S. Zamini, I. Bennett, E. Gerritsen, P. Malbranche, P. Pugliatti, A. Di Stefano, F. Aleo, D. Bertani, F. Paletta, F. Roca, G. Graditi, M. Pellegrino, O. Zubillaga, F. J. C. Iranzo, A. Pozza, T. Sample, and R. Gottschalg, "Changes of solar cell parameters during damp-heat exposure," *Progress in Photovoltaics: Research and Applications*, vol. 24, no. 10, pp. 1346–1358, Oct. 2016. [Online]. Available: <http://onlinelibrary.wiley.com/doi/10.1002/pip.2793/abstract>
- [174] W. Luo, P. Hacke, J. P. Singh, J. Chai, Y. Wang, S. Ramakrishna, A. G. Aberle, and Y. S. Khoo, "In-Situ Characterization of Potential-Induced Degradation in Crystalline Silicon Photovoltaic Modules Through Dark I–V Measurements," *IEEE Journal of Photovoltaics*, vol. 7, no. 1, pp. 104–109, Jan. 2017.

- [175] Y. Komatsu, S. Yamaguchi, A. Masuda, and K. Ohdaira, "Multistage performance deterioration in n-type crystalline silicon photovoltaic modules undergoing potential-induced degradation," *Microelectronics Reliability*, vol. 84, pp. 127–133, May 2018. [Online]. Available: <http://www.sciencedirect.com/science/article/pii/S0026271418301318>
- [176] W. Luo, Y. S. Khoo, J. P. Singh, J. K. C. Wong, Y. Wang, A. G. Aberle, and S. Ramakrishna, "Investigation of Potential-Induced Degradation in n-PERT Bifacial Silicon Photovoltaic Modules with a Glass/Glass Structure," *IEEE Journal of Photovoltaics*, vol. 8, no. 1, pp. 16–22, Jan. 2018.
- [177] R. Asadpour, D. B. Sulas-Kern, S. Johnston, J. Meydbray, and M. A. Alam, "Dark Lock-in Thermography Identifies Solder Bond Failure as the Root Cause of Series Resistance Increase in Fielded Solar Modules," *IEEE Journal of Photovoltaics*, pp. 1–8, jul 2020.
- [178] R. A. Sinton and A. Cuevas, "Contactless determination of current–voltage characteristics and minority-carrier lifetimes in semiconductors from quasi-steady-state photoconductance data," *Applied Physics Letters*, vol. 69, no. 17, pp. 2510–2512, Oct. 1996, publisher: American Institute of Physics. [Online]. Available: <https://aip.scitation.org/doi/10.1063/1.117723>
- [179] J. S. Fada, A. J. Loach, A. J. Curran, J. L. Braid, S. Yang, T. J. Peshek, and R. H. French, "Correlation of I-V Curve Parameters with Module-Level Electroluminescent Image Data Over 3000 Hours Damp-Heat Exposure," in *2017 IEEE 44th Photovoltaic Specialist Conference (PVSC)*, Jun. 2017, pp. 2697–2701.
- [180] A. M. Karimi, J. S. Fada, N. A. Parrilla, B. G. Pierce, M. Koyutürk, R. H. French, and J. L. Braid, "Generalized and Mechanistic PV Module Performance Prediction From Computer Vision and Machine Learning on Electroluminescence Images," *IEEE Journal of Photovoltaics*, vol. 10, no. 3, pp. 878–887, May 2020, conference Name: IEEE Journal of Photovoltaics.
- [181] X. Sun, R. V. K. Chavali, and M. A. Alam, "Real-time monitoring and diagnosis of photovoltaic system degradation only using maximum power point—the Suns-Vmp method," *Progress in Photovoltaics: Research and Applications*, vol. 27, no. 1, pp. 55–66, 2019. [Online]. Available: <https://onlinelibrary.wiley.com/doi/abs/10.1002/pip.3043>
- [182] T. Fuyuki, H. Kondo, T. Yamazaki, Y. Takahashi, and Y. Uraoka, "Photographic surveying of minority carrier diffusion length in polycrystalline silicon solar cells by electroluminescence," *Applied Physics Letters*, vol. 86, no. 26, p. 262108, Jun. 2005. [Online]. Available: <https://aip.scitation.org/doi/10.1063/1.1978979>
- [183] D. Hinken, K. Ramspeck, K. Bothe, B. Fischer, and R. Brendel, "Series resistance imaging of solar cells by voltage dependent electroluminescence," *Applied Physics Letters*, vol. 91, no. 18, p. 182104, Oct. 2007. [Online]. Available: <https://aip.scitation.org/doi/10.1063/1.2804562>
- [184] K. N. Zaunbrecher, S. W. Johnston, and J. R. Sites, "Identification and analysis of distinct features in imaging thin-film solar cells," in *2012 38th IEEE Photovoltaic Specialists Conference*, Jun. 2012, pp. 001 716–001 720, iSSN: 0160-8371, 0160-8371.

- [185] K. Ramspeck, K. Bothe, D. Hinken, B. Fischer, J. Schmidt, and R. Brendel, "Recombination current and series resistance imaging of solar cells by combined luminescence and lock-in thermography," *Applied Physics Letters*, vol. 90, no. 15, p. 153502, Apr. 2007. [Online]. Available: <https://aip.scitation.org/doi/10.1063/1.2721138>
- [186] O. Breitenstein, J. Bauer, K. Bothe, D. Hinken, J. Müller, W. Kwapil, M. C. Schubert, and W. Warta, "Can Luminescence Imaging Replace Lock-in Thermography on Solar Cells?" *IEEE Journal of Photovoltaics*, vol. 1, no. 2, pp. 159–167, Oct. 2011.
- [187] R. A. Bardos, J. Weber, O. Breitenstein, J. Bauer, M. Lenio, T. Trupke, and Y. Augarten, "Luminescence Shunt Imaging: Qualitative and Quantitative Shunt Images Using Photoluminescence Imaging," in *24th European Photovoltaic Solar Energy Conference*, Hamburg, Germany, Sep. 2009, pp. 27–31. [Online]. Available: <http://www.eupvsec-proceedings.com/proceedings?paper=4460>
- [188] D. Kendig, J. Christofferson, G. B. Alers, and A. Shakouri, "Application of thermoreflectance imaging to identify defects in photovoltaic solar cells," in *2010 26th Annual IEEE Semiconductor Thermal Measurement and Management Symposium (SEMI-THERM)*, Feb. 2010, pp. 245–248, iSSN: 1065-2221, 1065-2221.
- [189] O. Breitenstein, J. Bauer, D. Hinken, and K. Bothe, "The reliability of thermography- and luminescence-based series resistance and saturation current density imaging," *Solar Energy Materials and Solar Cells*, vol. 137, pp. 50–60, Jun. 2015. [Online]. Available: <http://www.sciencedirect.com/science/article/pii/S0927024815000276>
- [190] O. Breitenstein, C. Shen, H. Kampwerth, and M. A. Green, "Comparison of DLIT- and PL-based Local Solar Cell Efficiency Analysis," *Energy Procedia*, vol. 38, pp. 2–12, Jan. 2013. [Online]. Available: <http://www.sciencedirect.com/science/article/pii/S1876610213013295>
- [191] N. Bosco, T. J. Silverman, and S. Kurtz, "Climate specific thermomechanical fatigue of flat plate photovoltaic module solder joints," *Microelectronics Reliability*, vol. 62, pp. 124–129, Jul. 2016. [Online]. Available: <http://www.sciencedirect.com/science/article/pii/S0026271416300609>
- [192] Dana B. Sulas-Kern, Steve Johnston, and Jenya Meydbray, "Fill Factor Loss in Fielded Photovoltaic Modules Due to Metallization Failures, Characterized by Luminescence and Thermal Imaging," in *46th IEEE Photovoltaic Specialists Conference (PVSC 46)*, Chicago, IL, USA, Jun. 2019.
- [193] J. Walter, D. Eberlein, J. Haunschild, M. Tranitz, and U. Eitner, "A Method to Detect Defective Solder Joints by RS-Electroluminescence Imaging," *Energy Procedia*, vol. 27, pp. 652–657, Jan. 2012. [Online]. Available: <http://www.sciencedirect.com/science/article/pii/S1876610212013379>
- [194] M. Heimann, R. Bakowskie, M. Köhler, J. Hirsch, M. Junghänel, A. Hussack, and S. Sachert, "Investigations of Different Soldering Failure Modes and their Impact on Module Reliability," *Energy Procedia*, vol. 55, pp. 456–463, 2014. [Online]. Available: <https://linkinghub.elsevier.com/retrieve/pii/S1876610214012338>

- [195] A. S. Rajput, C. D. Rodríguez-Gallegos, J. W. Ho, S. Nalluri, S. Raj, A. G. Aberle, and J. P. Singh, “Fast extraction of front ribbon resistance of silicon photovoltaic modules using electroluminescence imaging,” *Solar Energy*, vol. 194, pp. 688–695, Dec. 2019. [Online]. Available: <http://www.sciencedirect.com/science/article/pii/S0038092X19311119>
- [196] Iea Pvps and Marco Paggi, “Task 13: Review on IR and EL Imaging for PV Field Applications – IEA-PVPS,” library Catalog: iea-pvps.org. [Online]. Available: <https://iea-pvps.org/key-topics/review-on-ir-and-el-imaging-for-pv-field-applications/>
- [197] S. Gallardo-Saavedra, L. Hernández-Callejo, and O. Duque-Perez, “Technological review of the instrumentation used in aerial thermographic inspection of photovoltaic plants,” *Renewable and Sustainable Energy Reviews*, vol. 93, pp. 566–579, Oct. 2018. [Online]. Available: <http://www.sciencedirect.com/science/article/pii/S1364032118303708>
- [198] R. Bhoopathy, O. Kunz, M. Juhl, T. Trupke, and Z. Hameiri, “Outdoor photoluminescence imaging of photovoltaic modules with sunlight excitation,” *Progress in Photovoltaics: Research and Applications*, vol. 26, no. 1, pp. 69–73, 2018, eprint: <https://onlinelibrary.wiley.com/doi/pdf/10.1002/pip.2946>. [Online]. Available: <https://onlinelibrary.wiley.com/doi/abs/10.1002/pip.2946>
- [199] J. H. Werner, M. Reuter, and L. Stoicescu, “DaySy: Luminescence Imaging of PV Modules in Daylight,” *29th European Photovoltaic Solar Energy Conference and Exhibition*, pp. 2553–2554, Nov. 2014, iISBN: 9783936338348 Publisher: WIP. [Online]. Available: <http://www.eupvsec-proceedings.com/proceedings?paper=31101>
- [200] S. Johnston, “Contactless electroluminescence imaging for cell and module characterization,” in *2015 IEEE 42nd Photovoltaic Specialist Conference (PVSC)*, Jun. 2015, pp. 1–6.
- [201] M. Razani, A. Parkhimchyk, and N. Tabatabaei, “Lock-in thermography using a cellphone attachment infrared camera,” *AIP Advances*, vol. 8, no. 3, p. 035305, Mar. 2018, publisher: American Institute of Physics. [Online]. Available: <https://aip.scitation.org/doi/10.1063/1.5021601>
- [202] R. Asadpour and M. A. Alam, “Prediction of Efficiency Loss of c-Si Solar Modules due to Soler-bond Failure using Physics-Based Modeling,” (*Under Preparation*).
- [203] S. Suzuki, T. Tanahashi, T. Doi, and A. Masuda, “Acceleration of degradation by highly accelerated stress test and air-included highly accelerated stress test in crystalline silicon photovoltaic modules,” *Japanese Journal of Applied Physics*, vol. 55, no. 2, p. 022302, Jan. 2016. [Online]. Available: <http://iopscience.iop.org/article/10.7567/JJAP.55.022302/meta>
- [204] T. H. Kim, N. C. Park, and D. H. Kim, “The effect of moisture on the degradation mechanism of multi-crystalline silicon photovoltaic module,” *Microelectronics Reliability*, vol. 53, no. 9, pp. 1823–1827, Sep. 2013. [Online]. Available: <http://www.sciencedirect.com/science/article/pii/S0026271413002229>

- [205] M. Koehl, S. Hoffmann, and S. Wiesmeier, "Evaluation of damp-heat testing of photovoltaic modules," *Progress in Photovoltaics: Research and Applications*, vol. 25, no. 2, pp. 175–183, Feb. 2017. [Online]. Available: <https://onlinelibrary.wiley.com/doi/full/10.1002/pip.2842>
- [206] P. Hacke, S. Spataru, K. Terwilliger, G. Perrin, S. Glick, S. Kurtz, and J. Wohlgemuth, "Accelerated Testing and Modeling of Potential-Induced Degradation as a Function of Temperature and Relative Humidity," *IEEE Journal of Photovoltaics*, vol. 5, no. 6, pp. 1549–1553, Nov. 2015.
- [207] S. Yamaguchi and K. Ohdaira, "Degradation behavior of crystalline silicon solar cells in a cell-level potential-induced degradation test," *Solar Energy*, vol. 155, pp. 739–744, Oct. 2017. [Online]. Available: <http://www.sciencedirect.com/science/article/pii/S0038092X17305844>
- [208] J. Oh, S. Bowden, and G. TamizhMani, "Potential-Induced Degradation (PID): Incomplete Recovery of Shunt Resistance and Quantum Efficiency Losses," *IEEE Journal of Photovoltaics*, vol. 5, no. 6, pp. 1540–1548, Nov. 2015.
- [209] W. Oh, S. Bae, S.-I. Chan, H.-S. Lee, D. Kim, and N. Park, "Field degradation prediction of potential induced degradation of the crystalline silicon photovoltaic modules based on accelerated test and climatic data," *Microelectronics Reliability*, vol. 76-77, pp. 596–600, Sep. 2017. [Online]. Available: <http://www.sciencedirect.com/science/article/pii/S0026271417303645>
- [210] Y. Chen, P. Hacke, Y. S. Khoo, K. VanSant, Z. Wang, W. Luo, J. Chai, C. Deline, Y. Wang, A. G. Aberle, P. P. Altermatt, Z. Feng, S. Kurtz, and P. J. Verlinden, "Field Investigations of Potential-Induced Degradation (PID) for Crystalline Silicon PV Panels in Different Climates," in *2017 IEEE 44th Photovoltaic Specialist Conference (PVSC)*, Jun. 2017, pp. 1922–1926.
- [211] F. Ohashi, Y. Mizuno, H. Yoshida, H. Kosuga, T. Furuya, R. Fuseya, R. J. Freitas, Y. Hara, A. Masuda, and S. Nonomura, "Sodium distribution at the surface of silicon nitride film after potential-induced degradation test and recovery test of photovoltaic modules," *Japanese Journal of Applied Physics*, vol. 57, no. 8S3, p. 08RG05, Jul. 2018. [Online]. Available: <http://iopscience.iop.org/article/10.7567/JJAP.57.08RG05/meta>
- [212] S. Yamaguchi, C. Yamamoto, K. Ohdaira, and A. Masuda, "Reduction in the short-circuit current density of silicon heterojunction photovoltaic modules subjected to potential-induced degradation tests," *Solar Energy Materials and Solar Cells*, vol. 161, pp. 439–443, Mar. 2017. [Online]. Available: <http://www.sciencedirect.com/science/article/pii/S0927024816305499>
- [213] K. Hara, K. Ogawa, Y. Okabayashi, H. Matsuzaki, and A. Masuda, "Influence of surface structure of n-type single-crystalline Si solar cells on potential-induced degradation," *Solar Energy Materials and Solar Cells*, vol. 166, pp. 132–139, Jul. 2017. [Online]. Available: <http://www.sciencedirect.com/science/article/pii/S0927024817301320>

- [214] C. Dechthummarong, B. Wiengmoon, D. Chenvidhya, C. Jivacate, and K. Kirtikara, "Physical deterioration of encapsulation and electrical insulation properties of PV modules after long-term operation in Thailand," *Solar Energy Materials and Solar Cells*, vol. 94, no. 9, pp. 1437–1440, Sep. 2010. [Online]. Available: <http://www.sciencedirect.com/science/article/pii/S0927024810002011>
- [215] M. Winkler, B. Richardson, S. Pingel, H. Hoehne, O. Frank, and J. Berghold, "Potential Induced Degradation of Solar Cells and Panels," *25th European Photovoltaic Solar Energy Conference and Exhibition / 5th World Conference on Photovoltaic Energy Conversion, 6-10 September 2010, Valencia, Spain*, pp. 3753–3759, Oct. 2010. [Online]. Available: <http://www.eupvsec-proceedings.com/proceedings?paper=8622>
- [216] C. Ballif, A. Virtuani, F. Sculati-Meillaud, M. Topic, L.-E. Perret-Aebi, H. Y. Li, F. Galliano, M. Jankovec, and E. Annigoni, "Modeling Potential-Induced Degradation (PID) in Crystalline Silicon Solar Cells: From Accelerated-Aging Laboratory Testing to Outdoor Prediction," *32nd European Photovoltaic Solar Energy Conference and Exhibition*, pp. 1558–1563, Jul. 2016. [Online]. Available: <http://www.eupvsec-proceedings.com/proceedings?paper=38295>
- [217] Y.-J. Jeon, D.-S. Kim, and Y.-E. Shin, "Study of characteristics of solar cells through thermal shock and high-temperature and high-humidity testing," *International Journal of Precision Engineering and Manufacturing*, vol. 15, no. 2, pp. 355–360, Feb. 2014. [Online]. Available: <https://doi.org/10.1007/s12541-014-0345-6>
- [218] Y.-J. Jeon, M.-S. Kang, and Y.-E. Shin, "Growth of an Ag₃Sn Intermetallic Compound Layer Within Photovoltaic Module Ribbon Solder Joints," *International Journal of Precision Engineering and Manufacturing-Green Technology*, Apr. 2019. [Online]. Available: <https://doi.org/10.1007/s40684-019-00028-1>
- [219] M.-S. Kang, Y.-J. Jeon, D.-S. Kim, and Y.-E. Shin, "Comparison of the 60Sn40Pb and 62Sn2Ag36Pb Solders for a PV Ribbon Joint in Photovoltaic Modules Using the Thermal Shock Test," *Energies*, vol. 10, no. 4, p. 529, Apr. 2017. [Online]. Available: <https://www.mdpi.com/1996-1073/10/4/529>
- [220] S. Kawai, T. Tanahashi, Y. Fukumoto, F. Tamai, A. Masuda, and M. Kondo, "Causes of Degradation Identified by the Extended Thermal Cycling Test on Commercially Available Crystalline Silicon Photovoltaic Modules," *IEEE Journal of Photovoltaics*, vol. 7, no. 6, pp. 1511–1518, nov 2017.
- [221] N. Jiang, A. G. Ebadi, K. H. Kishore, Q. A. Yousif, and M. Salmani, "Thermomechanical Reliability Assessment of Solder Joints in a Photovoltaic Module Operated in a Hot Climate," *IEEE Transactions on Components, Packaging and Manufacturing Technology*, vol. 10, no. 1, pp. 160–167, Jan. 2020, conference Name: IEEE Transactions on Components, Packaging and Manufacturing Technology.

- [222] N. H. Jabarullah, A. Surendar, M. Arun, A. F. Siddiqi, and T. O. Krasnopevtseva, "Microstructural Characterization and Unified Reliability Assessment of Aged Solder Joints in a PV Module," *IEEE Transactions on Components, Packaging and Manufacturing Technology*, vol. 10, no. 6, pp. 1028–1034, Jun. 2020, conference Name: IEEE Transactions on Components, Packaging and Manufacturing Technology.
- [223] E. H. Amalu, D. J. Hughes, F. Nabhani, and J. Winter, "Thermo-mechanical deformation degradation of crystalline silicon photovoltaic (c-Si PV) module in operation," *Engineering Failure Analysis*, vol. 84, pp. 229–246, feb 2018.
- [224] I. M. Peters and T. Buonassisi, "Energy Yield Limits for Single-Junction Solar Cells," *Joule*, vol. 2, no. 6, pp. 1160–1170, jun 2018.
- [225] M. A. Alam and R. K. Smith, "A phenomenological theory of correlated multiple soft-breakdown events in ultra-thin gate dielectrics," *IEEE International Reliability Physics Symposium Proceedings*, vol. 2003-January, pp. 406–411, 2003.
- [226] R. Asadpour and M. A. Alam, "Is Damp Heat Degradation of c-Si Modules Essentially Universal?" in *Conference Record of the IEEE Photovoltaic Specialists Conference*. Institute of Electrical and Electronics Engineers Inc., jun 2019, pp. 1939–1941.

APPENDICES

A. IMPORTANCE OF THICKNESS VARIATION FOR INDIVIDUAL CELLS

Fig. A.1 shows thickness dependence of typical perovskite solar cell characteristics. In general, the efficiency follows J_{SC} trend. The slight increase in the current density for the thickness less than $0.12 \mu m$ is attributed to enhanced light absorption arising from the interference of the back mirror (contact).

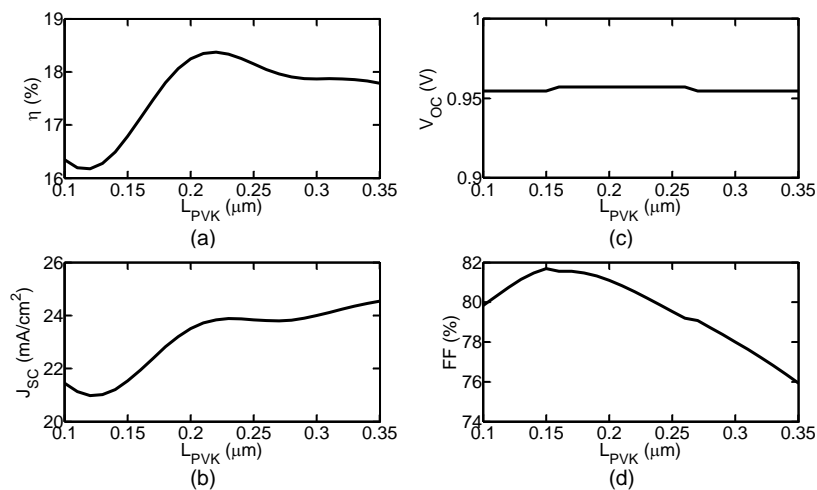


Fig. A.1. Thickness dependence of perovskite cell characteristics.

The performance of the HIT cell is relatively insensitive to the thickness of the absorber (between 100 to 200 μm), see Fig. A.2. Therefore in the optimization of tandem cell, we only considered the variation of the perovskite layer thickness.

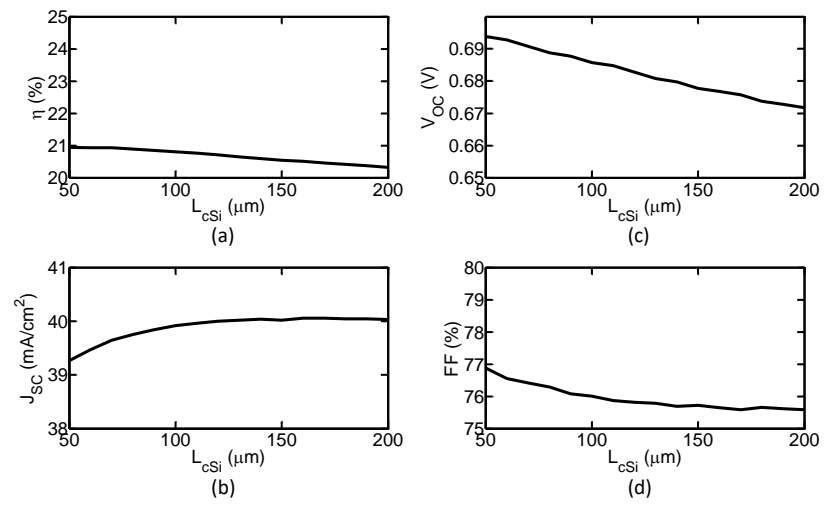


Fig. A.2. Thickness dependence of HIT cell characteristics.

B. ENERGY BAND DIAGRAM OF INDIVIDUAL SUB-CELLS OF PEROVSKITE-HIT TANDEM STRUCTURE

The energy band diagram of the perovskite sub-cell in short circuit condition is shown in Fig. B.1. The perovskite layer is fully depleted (from $0.040 \mu m$ to $0.175 \mu m$). Due to the electrical field in the depletion region, the generated charged carriers will be directed to corresponding contacts. PEDOT:PSS layer (from $0 \mu m$ to $0.040 \mu m$) acts as Hole Transport Material (HTM). PCBM layer (from $0.175 \mu m$ to $0.195 \mu m$) is acting as an Electron Transport Material (ETM) and blocking the holes to be collected in the wrong contact.

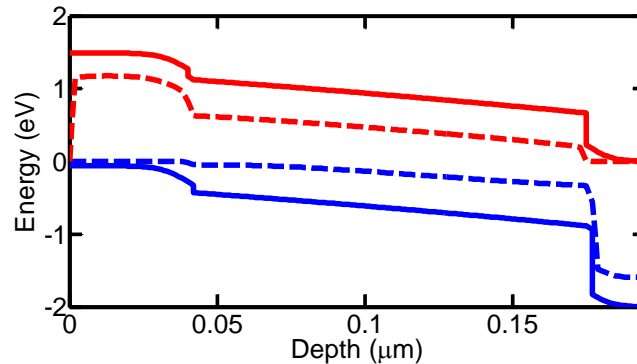


Fig. B.1. The energy band diagram of the perovskite (PVK) sub-cell under short circuit condition.

The photo-generated carriers (holes) in the c-Si absorber region reach the junction through diffusion and get collected at the front contact. The a-Si layers at the back of the device act as effective back surface field and avoids recombination at the wrong contact. The properties of the a-Si/c-Si heterojunction (see Fig. B.2) such as (band offset, emitter doping, etc.) at the junction dictate the performance of the device.

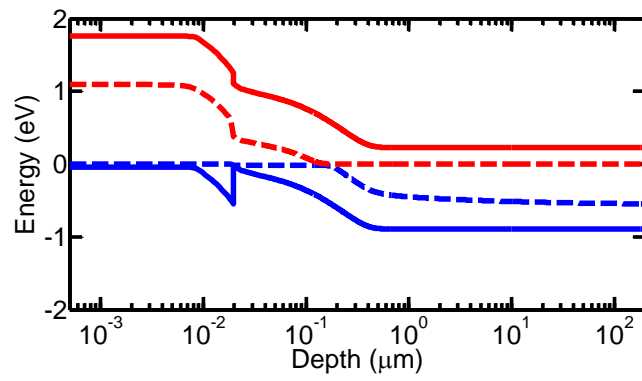


Fig. B.2. The energy band diagram of the HIT sub-cell under short circuit condition.

VITA

VITA

Reza Asadpour received his B. Sc. and M. Sc. degrees in electrical engineering from University of Tehran, Tehran, Iran, in 2010 and 2013, respectively. For his undergraduate thesis he worked on optical lithography and its correction methods. Then he worked on asymmetrical transistor structure to improve reliability and performance of the 6T SRAM design for his Master's thesis. Since 2013, he has been with Prof. Alam's CEED group at Purdue University working on modeling and interpreting perovskite solar cells and c-Si reliability issues towards his Ph.D. degree. His research interest include semiconductor device physics and reliability issues and compact and predictive modeling of electronic devices.